POLITECNICO DI MILANO

Facoltá di Ingegneria dei Processi Industriali

Corso di Laurea Specialistica in Ingegneria Nucleare

Dipartimento di Energia

Single and parallel channel stability analysis by means of multiphysics modeling

Relatore: Prof. Antonio CAMMI

Correlatore: Ing. Davide PAPINI

Tesi di Laurea di:

Gianluca GIORGI Matr. 734352

Anno accademico 2009-2010

Contents

List of Figures

List of Tables

Abstract

Aim of this work has been the development of a predictive model of the behavior of boiling water systems. In particular, the stability analysis of single and parallel channels has been approached by means of a multi-physics modeling: the stability of such systems are an important concern for the operation and safety of many industrial applications and, in particular, in energetic and nuclear fields.

A review the most important results available from literature on the two-phase flow dynamic instabilities in boiling systems has been firstly presented. Main object of the work is the development of a one-dimensional model for mixtures of steam and water flowing through heated channels; such a model has been then validated on experimental data collected at SIET thermal hydraulics laboratories in Piacenza (Italy).

Different aspects of the single channel behavior has been studied. At first an extensive steady state analysis has been performed: more precisely, several steady simulations allowed the calculation of the characteristic curves of such system and, moreover, these ones permitted the deduction of informations on its static stability. Afterwards, a linear stability analysis has been carried out so as to obtain the stability maps of the system and compared the results obtained with some ones available from literature. Finally, some transient calculations have been executed and analyzed.

Instead, for the parallel channel system only a preliminary study on their behavior in a single phase condition has been done in view of a more detailed future analyses.

The overall work has been realized by using *COMSOL Multiphysics* code.

Estratto in lingua italiana

Il problema dell'instabilità termoidraulica di canali bollenti è piuttosto rilevante in moltissime applicazioni industriali. In particolare, nell'ambito della produzione di potenza elettrica da fonte nucleare (e non solo), i risvolti che tale problematica ha sugli aspetti legati alla progettazione ottimale e alla sicurezza degli impianti hanno portato ad un interesse sempre maggiore verso lo studio e la comprensione dei fenomeni fisici alla base di tali instabilità. Oltretutto, la produzione di potenza elettrica da fonte nucleare avviene per lo più mediante l'utilizzo dei cosiddetti reattori ad acqua leggera (LWR), dei quali, buona parte, sono del tipo ad acqua bollente (BWR). In quest'ultimo caso l'accoppiamento tra i meccanismi di instabilità termoidraulica e le retroazioni legate alla neutronica del sistema rendono la problematica ancora più complessa e alimentano la necessità di una sua migliore comprensione. Non meno importante poi è il caso dei generatori di vapore la cui stabilità o instabilità influenza in maniera significativa l'impianto nel suo insieme.

É proprio in questa ottica che va collocato il presente lavoro. L'obiettivo con il quale è stata concepita questa tesi è stato quello di effettuare un'analisi di stabilità di sistemi termoidraulici ad acqua (H_2O) costituiti da uno o più canali cilindrici disposti in parallelo ed uniti alla base e alla sommità da due collettori: i cosiddetti *lower plenum* e *upper plenum*.

Per poter effettuare tale studio è stato necessario innanzitutto sviluppare un opportuno modello. Nel caso in esame si è scelto di schematizzare i canali come sistemi monodimensionali assumendo che le grandezze fisiche caratteristiche del fluido su ciascuna sezione fossero costanti e pari al valor medio sulla stessa. L'intera modellizzazione è stata effettuata con un approccio *"multi-fisico"*, utilizzando cioè un codice in grado di risolvere problemi numerici basati su sistemi di equazioni dif-

ferenziali alle derivate parziali (PDE) accoppiate, che ha il vantaggio di consentire una grande flessibilità nella costruzione di modelli di sistemi più o meno complessi in cui molteplici fenomeni fisici hanno luogo simultaneamente. Il codice utilizzato a tale scopo è *COMSOL Multiphysics*.

Tale tipo di approccio ha permesso la costruzione, in un primo momento, di un modello di sola termofluidodinamica bifase basato sul cosiddetto *Thermal Equilibrium Drift Flux Model* il quale prevede l'ipotesi di equilibrio termodinamico tra le fasi componenti la miscela bifase su ciascuna sezione ma tiene in considerazione lo scorrimento tra le due fasi.

L'adozione di tale modello si è rivelata piuttosto efficace: la procedura di validazione effettuata mediante i dati sperimentali raccolti presso i laboratori di termoidraulica SIET di Piacenza ha mostrato un buon accordo tra dati misurati e dati simulati.

Il modello è stato perciò utilizzato per effettuare l'analisi di un singolo canale e, per fare ciò, è stato aggiunto ad esso un modello di perdita di carico localizzata sia all'ingresso che all'uscita e un semplice modello termico di parete del condotto. Le perdite localizzate sono state introdotte per generalizzare il modello di canale introducendo in esso degli organi regolatori di flusso o dei tratti non riscaldati puntiformi (ad esempio un *riser*).

L'analisi di questo sistema si compone principalmente di tre diversi studi: uno stazionario, un'analisi di stabilità lineare, uno transitorio.

Sia lo studio stazionario che l'analisi di stabilità lineare hanno mostrato un buon accordo con le previsioni teoriche e con i risultati trovati in letteratura. In particolare, durante lo studio stazionario, sono stati analizzati i risultati ottenuti con il modello omogeneo (HEM) e con il *drift flux model* sia in termini di distribuzione assiale delle varie grandezze sia in termini di curve caratteristiche pressione-portata del sistema. Queste ultime poi sono utili per considerazioni statiche sulla stabilità che si è osservato essere influenzata dai parametri operativi come da letteratura.

Per quanto riguarda l'analisi di stabilità lineare, essa è stata effettuata linearizzando il sistema attorno ai punti di equilibrio (stati stazionari) calcolati mediante le simulazioni stazionarie e determinando gli autovalori della matrice della dinamica.

Tale operazione è stata fatta utilizzando il solutore agli autovalori di *COMSOL Multiphysics* il cui segno ha permesso di determinare la stabilità lineare del sistema e di tracciare la mappa di stabilità del sistema. In essa il confine tra zona stabile e zona instabile è stato calcolato utilizzando sia il *drift flux model* che il modello omogeneo e al variare del grado di orifiziatura all'ingresso e all'uscita: i risultati ottenuti sono in accordo con quelli reperiti in letteratura.

A partire dalle mappe di stabilità ottenute, sono state effettuate delle simulazioni in regime transitorio per verificare la risposta non lineare del sistema in condizioni stabili e instabili. In condizioni stabili è stata studiata la risposta ad un gradino di potenza termica ed è stato possibile, a partire dai risultati ottenuti, l'effetto attenuante della parete che ci si aspettava. In condizioni instabili sono state invece osservate oscillazioni divergenti autosostenute in assenza di parete, oscillazioni non divergenti in presenza di quest'ultima.

Infine, è stato svolto uno studio preliminare di un sistema costituito da due canali disposti in parallelo. La costruzione del modello del sistema è stata effettuata a partire dal modello di canale singolo aggiungendo le opportune condizioni al contorno e i parametri sono stati scelti in modo tale da realizzare la condizione di flusso monofase. La procedure di analisi utilizzata per il singolo canale è stata applicata a titolo di esempio a questo sistema rivelandosi efficace per un'analisi sistematica in condizioni di flusso bifase da svolgere in un futuro sviluppo del presente lavoro.

Introduction

In the present thesis, the study of the behavior of thermal hydraulic systems made by single and parallel channels has been approached by means of a multi-physics modeling. Special attention has been focused to the study of their stability: indeed, the transit of the fluid through a heated channel can induce, if a phase change occurs, different kinds of instabilities which can harmfully limit its potential application.

Such an issue is of great importance in many industrial applications. In particular in energetic and nuclear field it plays a fundamental role both for all the aspect concerning the normal exercise and for all those ones concerning the safety: conventional and nuclear steam generators and cores of LWRs are systems in which water, flowing through several heated channels, can undergo, normally or accidentally, a phase change and be so subject to the mentioned instability problems.

The present thesis work is made by four chapters.

Chapter 1 has been conceived with the aim of provide a basically knowledge background. In a first part, a review of the known phenomena that lead to boiling system instabilities is, indeed, reported. A more detailed description is reserved to the static instabilities, namely the Ledinegg instabilities, and to the oscillation mechanism known as pressure drop and density wave oscillations; small mention is dedicated to minor instability types. The second part of the chapter illustrates the most commonly adopted techniques to analyze such instabilities.

In chapter 2, the creation of a one-dimensional model for the fluid dynamics of both water and of mixtures of steam and water is illustrated. At first, the thermal hydraulics of a generic heated channel has been modeled by using the *Thermal Equilibrium Drift Flux Model*; in a second place, the model has been implemented and validated on an available experimental data set relative to an helically coiled steam

generator prototype located at SIET thermal hydraulics laboratories placed in Piacenza (Italy).

In chapter 3, the development of the central part of the entire work is reported. It consisted in the stability analysis of a single boiling channel system: in order to perform it, the developed model for the single/two-phase flow dynamics has been completed by adding two local pressure loss terms and a simple heating model. the analysis can be divided into three different sub-analyses: an exhaustive stationary study, a linear stability analysis, some transient calculations. In particular the stability analysis results have been compared to some ones found in literature.

In chapter 4, the model for the analysis of parallel channel systems has been mainly set up by means of the opportune specification of the boundary conditions. Actually, such a system is made by two channels only and the performed analyses have been done in single-phase flow conditions. Indeed, the aim of this chapter is a preliminary study of this system: a similar procedure used to investigate the single channel system stability is here applied to some test cases in order to show the applicability of the technique.

All the analyses and the calculations done has been realized by means of *COMSOL Multiphysics* code: this software is capable of solving numerical problems based on partial differential equations (PDE) by using the finite element method.

Chapter 1

Review of two-phase flow dynamic instabilities in boiling systems

Abstract

The objective of this chapter is to resume the main features of the thermohydraulic instabilities of boiling systems.

Beside the description of the physical mechanisms which lead to their manifestation, a summary of the approach used for their study is reported. A great mention is dedicated to the most common types of instability, that is the Ledinegg static instability mechanism, the pressure drop oscillations and the density wave oscillations.

A special attention has been dedicated to the description of the stability maps. These are, indeed, an important concern for this work.

1.1 Introduction

In this chapter, various well-known types of two-phase flow instabilities are reviewed.

After an introductory section in which a universally accepted classification of instabilities is reported, two main sections follow.

The first one illustrates the known mechanisms that cause the boiling systems instabilities. The ones related to the most important type of instabilities are discussed

rather extensively. The other ones are, instead, just briefly mentioned.

The second main section treats the main approaches to the study and the analysis of these instabilities. Particular attention is dedicated to the stability maps and to the parametric effects on the instability threshold.

1.2 Types of two-phase flow instabilities

A flow is stable if, when disturbed, its new operating conditions tend asymptotically towards the original ones. Mathematically, it is to say that the original operating point is a solution of a system with the property that slight perturbations damp out to produce the original state.

A flow is said to be subject to a static instability if, when disturbed, its new operating conditions tend asymptotically toward ones that are different from the original ones. In the language of dynamics, it is to say that the original operating point is not a stable equilibrium point, and the system moves to a different equilibrium point which is a stable one.

Known types of static instabilities include:

1. Flow excursions (Ledinegg instability).

2. Relaxation instabilities, such as flow pattern transitions, nucleation instabilities, bumping, chugging, geysering.

A flow is said to be subject to a dynamic instability when there is sufficient interaction and delayed feedback between the inertia of the flow and the compressibility of the two-phase mixture or it may result from multiple feedbacks between flow rate, pressure drop and the change in density as a result of the rate of vapor generation in a boiling channel. Dynamic instabilities can be characterized as:

1. Density wave type oscillations.

2. Pressure drop type oscillations.

3. Acoustic oscillations.

4. Thermal oscillations.

The mechanism at the basis of the dynamic instabilities can be explained by propagation time lags and feedback phenomena present in any two-phase flow system. The temporary disturbances take some time, which is proportional to the propagation wave speed, in reaching other points along the system. These delayed disturbances along the system are then reflected back to the initial point of the disturbance creating a new disturbance, and so on.

An important consideration about the stability of two-phase flow system is the specification of the boundary conditions. Boundary conditions generally determine which parts of the system may participate in the transients and which components will operate in a steady mode. However, boundary conditions are seldom exact: they usually represent an idealization of complex physical situations that are useful in simplifying the problem.

1.3 Two-phase flow instability mechanisms

In this section main two-phase flow instability mechanisms are illustrated: the Ledinegg instability, the instability from density wave oscillations and pressure drop oscillations.

Other types of minor instabilities are briefly treated at the end of the section.

1.3.1 The Ledinegg instability

Two-phase flow channels occasionally exhibit the particular S-shaped steady state pressure drop versus flow rate characteristic, shown in Figure 1.1.

Operations in the negative slope part of the characteristic is unstable and generally leads to flow excursion (Ledinegg instability).

The Ledinegg instability is a static instabilty that occurs when the slope of the channel demanded pressure drop (Δp) versus flow rate (w) curve (internal characteristic curve) is negative and steeper than the loop supplied pressure drop versus flow rate (external characteristic curve) and when there are multiple intersections of the internal and external characteristic.

The scenario of Ledinegg instability is shown in Figure 1.1. With an external char-

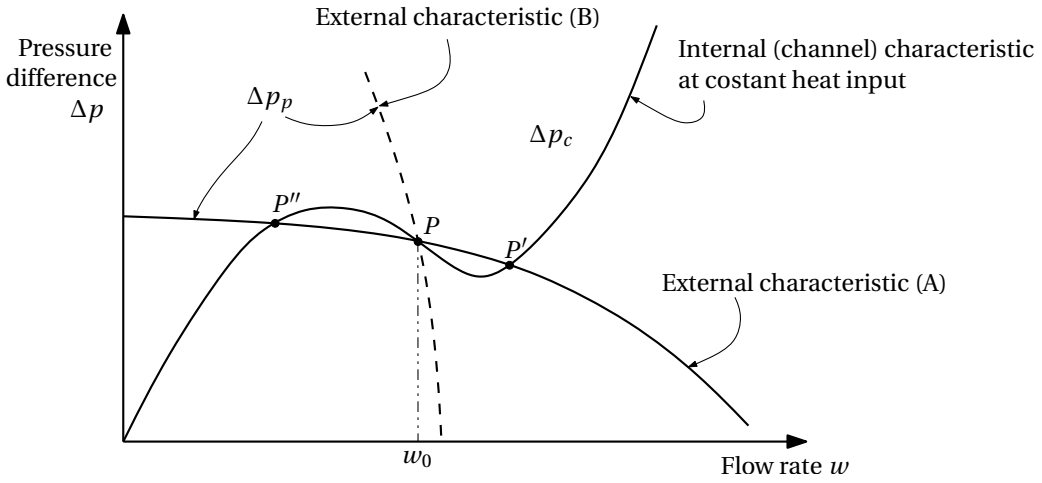

Figure 1.1: Ledinegg instability

acteristic (A) less steeper than the internal characteristic, the operation at point P is impossible. A small disturbance to a lower flow would lead to a condition where more pressure drop is required to sustain the flow than what is available from the external system, thus the flow rate would decrease further. Therefore, a slight decrease in flow rate will cause a spontaneous shift to point P''. The new equilibrium point usually corresponds to a flow rate where burn-out occurs. It is apparent that it would not possible to operate to the left of the minimum point on the internal characteristic curve with a flat eternal characteristic curve. The standard way to avoid Ledinegg instability is to make the slope of the external characteristic curve steeper than on the internal one (curve B).

This fact can be easily shown by considering the simple two-phase flow system of Figure 1.2. Characteristic curve of a typical centrifugal pump is represented by curve A of Figure 1.1.

The pressure difference between points 1 and 2 is given by:

$$p_2 - p_1 = \Delta p_p - I_p \frac{dw}{dt} \tag{1.1}$$

where I_p represents the inertia of this leg (proportional to L_p/A_p). For simplicity any frictional and gravitational pressure drops in this external part of the system has been neglected.

The pressure difference across the heated channel is given by:

$$p_2 - p_3 = \Delta p_c + I_c \frac{dw}{dt} \tag{1.2}$$

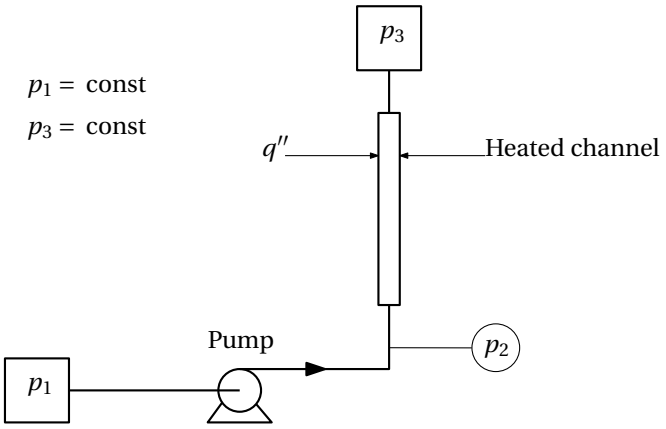

Figure 1.2: A simple two-phase flow system.

where Δp_c is the steady state internal characteristic of the channel shown in Figure 1.1 and w is the flow rate. The temporal acceleration effects have been approximately represented by means of the last term of equation (1.2), where I_c (proportional to L_c/A_c) represents the inertia of the "internal" leg of the system. At any time the following relation must be satisfy:

$$p_3 - p_1 = \Delta p_p - \Delta p_c - \left(I_p + I_c\right) \frac{dw}{dt} = \text{const} \tag{1.3}$$

Considering a small perturbation around an equilibrium point it is possible to write:

$$\Delta p_p(t) = \Delta p_p^0 + \delta \Delta p_p(t) \cong \Delta p_p^0 + \left.\frac{\partial \Delta p_p}{\partial w}\right|_0 \delta w(t) \tag{1.4}$$

$$\Delta p_c(t) = \Delta p_c^0 + \delta \Delta p_p(t) \cong \Delta p_c^0 + \left.\frac{\partial \Delta p_c}{\partial w}\right|_0 \delta w(t) \tag{1.5}$$

$$w(t) = w^0 + \delta w(t) \tag{1.6}$$

Substituting these expressions into equation (1.3) and eliminating the steady state terms, the governing equation for the flow rate perturbation is the following:

$$I \frac{dw}{dt} = A \delta w(t) \tag{1.7}$$

where

$$I = I_p + I_c$$

$$A \equiv \left.\frac{\partial \Delta p_p}{\partial w}\right|_0 - \left.\frac{\partial \Delta p_c}{\partial w}\right|_0$$

The solution of equation (1.7) for an initial flow perturbation δw_0 is:

$$\delta w = \delta w_0 \, e^{(A/I)\,t}$$

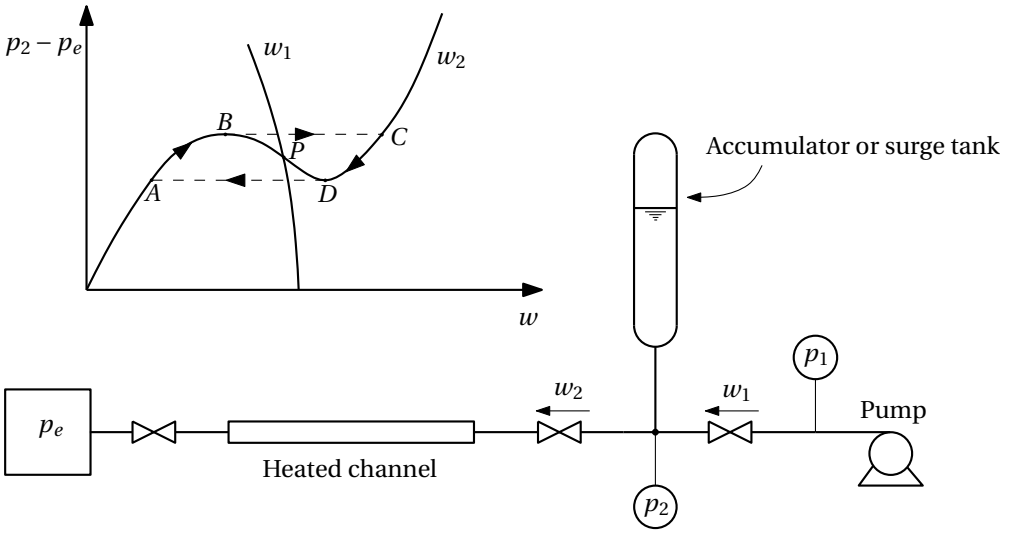

Figure 1.3: Schematic flow diagram and limit cycle of pressure drop type oscillations.

and it shows that the perturbation will grow if A is positive. Thus, it is possible to conclude that the system will be unstable if the slope of the channel characteristic is more negative than the slope of the external characteristic.

This stability criterion (negative value of parameter A) has been derived using the time-dependent momentum conservation equation, however it is based only on steady state considerations. Thus, the Ledinegg instability is classified as a static instability.

1.3.2 Pressure drop oscillations

A multivalued $(w, \Delta p)$ channel characteristic may lead to flow oscillation, rather than flow excursion (Ledinegg type), if there is sufficient interaction between the inertia of the flow and the compressibility of the two-phase mixture. The required compressible volume may be situated outside the heated section, but it might be provided even by the internal compressibility of long test sections.

With reference to Figure 1.3, the following steady state relations are considered:

$$p_1 - p_2 = K_1 \, w_1^2 \tag{1.8}$$

$$p_2 - p_e = \Psi(w_2) \tag{1.9}$$

Here p_1 is the external imposed pressure (pump), p_2 the surge tank pressure, p_e the exit pressure, K_1 is an experimentally determined constant for the inlet restric-

tion, w_1 is the mass flow rate into the surge tank and w_2 is the mass flow rate out of the surge tank (compressible volume).

Equation (1.8) represents the pressure drop across the inlet restriction and is a statement of the momentum equation across the restriction.

Equation (1.9) is the pressure drop between the surge tank and the system exit section and it is the system curve shown in Figure 1.3.

While operating in the negative slope portion, a slight increase in the surge tank pressure would cause more fluid to enter it than leave it. The surge tank pressure now increases due to accumulation of fluid. The operating point moves up until it reaches the peak (point B). Any higher pressure can be sustained only by a higher mass flow rate as given by the system curve. This point is found to be in the single-phase liquid region (point C). At C, the amount of fluid leaving the surge tank is more than the amount entering it. Therefore, the surge tank pressure decreases till the operating point reaches the curve minimum at D. Any lower pressure can now be obtained only if the mass flow rate reduces to the value at point A. Hence, an excursion to A is observed. Now the mass leaving the surge tank is less than that entering it. Hence pressure goes up pushing up the operating point till B is reached, where once again a flow excursion is observed. Thus, a perturbation at any point in the negative slope region results in a flow oscillation tracing the limit cycle $ABCDA$. This is essentially the mechanism of pressure drop oscillations. They can occur, as said, only if the system possesses a compressible volume, either external or internal.

If the compressible volume is situated upstream the heated section, the oscillations can be damped by throttling the inlet of the channel. Throttling may of course not be effective when compressibility is internal to the channel.

1.3.3 Density wave oscillations

Density wave oscillations are probably the most common type of instabilities encountered in two-phase flow systems, and result from the multiple feedbacks between the flow rate, the vapor generation rate and the pressure drop in a boiling channel (Figure 1.4).

The physical mechanism leading to density wave oscillations can be described in

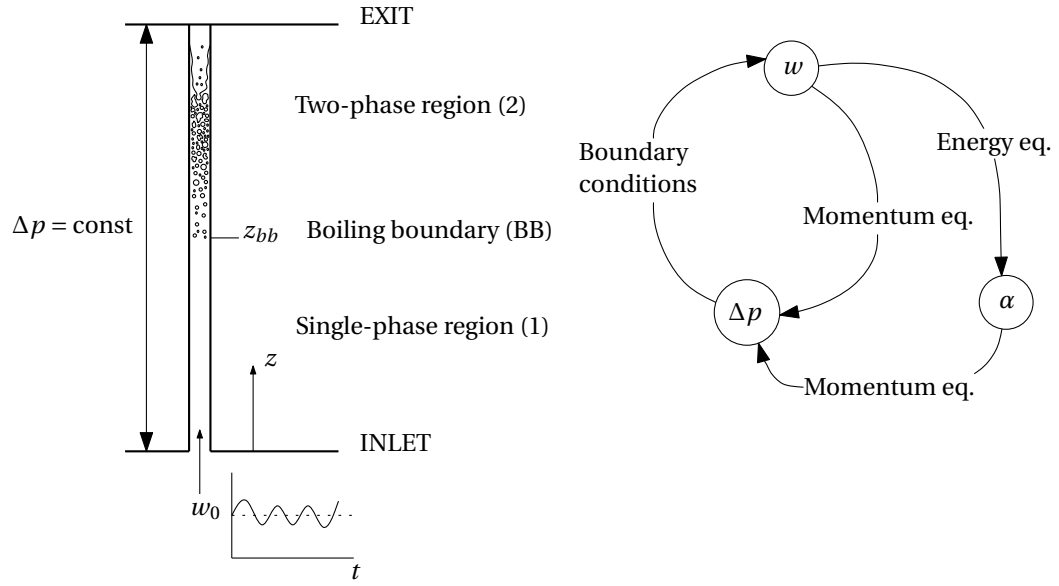

Figure 1.4: Boiling channel and various feedbacks.

several different ways. One such description by Yadigaroglu [1] follows.

With reference to Figure 1.4, the istantaneous position of boiling boundary BB, that is, the point where the bulk of the fluid reaches saturation, divides the channel into a single-phase region and a two-phase region.

If an oscillatory subcooled inlet flow enters the channel, the inlet flow oscillations δw will create propagating enthalpy perturbations in the single-phase region. The boiling boundary will respond by oscillating according to the amplitude and the phase of the enthalpy perturbations at the point where the flows reaches saturation. Changes in the flow and in the length of the single-phase region will combine to create an oscillatory, single-phase, pressure drop perturbation $\delta\Delta p_1$. Enthalpy perturbations in the two-phase region will appear as quality and void fraction perturbations and will travel with the flow along the heated channel. The combined effects of flow and void fraction perturbations and the variations of the two-phase length will create a two-phase pressure drop perturbation $\delta\Delta p_2$. Since the total pressure drop across the boiling channel is imposed by the external characteristic of the channel (for example, a large parallel channel connected to the test section by lower and upper plena), the two-phase pressure drop perturbations will create feedback pressure perturbations of the opposite sign in the single-phase region, which can either reenforce or attenuate the imposed oscillation by creating a feedback flow perturbation δw_{fdb}.

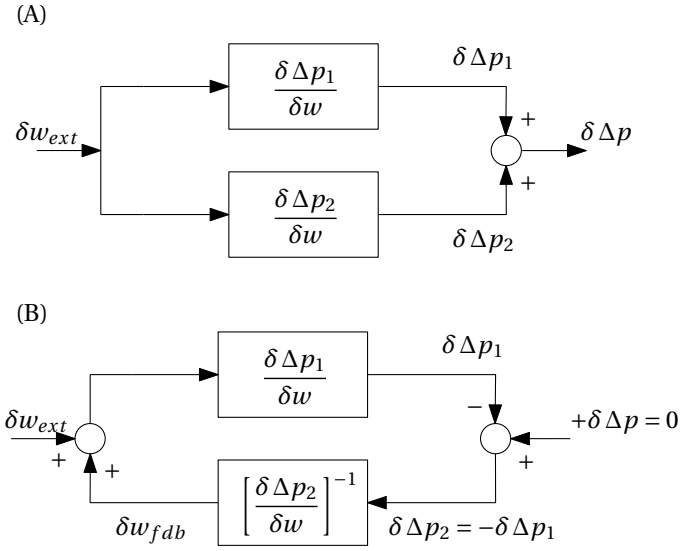

Figure 1.5: Block diagrams of a boiling channel.

With correct timing, the perturbations can acquire appropriate phases and become self-sustained. Under these conditions the system would be at the threshold of instability since it would have the capability of oscillating without externally imposed perturbations, while satisfying the boundary conditions; this situation is illustrated in Figure 1.5.

Alternatively one can say that the system crosses the threshold of instability when for a set of operating conditions and for a given inlet flow oscillation frequency ω, the total pressure drop perturbations vanishes, that is:

$$\delta \Delta p(\omega) = \delta \Delta p_1(\omega) + \delta \Delta p_2(\omega) = 0 \tag{1.10}$$

Under these conditions, since the boundary conditions imposed on the system are satisfied with oscillatory flow, the system tends to be unstable. Also this stability criterion is illustrated in Figure 1.5.

1.3.4 Other types of oscillations

The major types of instabilities have been discussed in the previous sections. Several other types of two-phase flow instabilities have been observed and are briefly reviewed in the following for the sake completeness.

Periodic expulsion or Chugging and Geysering

Chugging and geysering are relaxation instabilities characterized by periodic expulsion of coolant from the channel. The resulting transient behavior may be very mild or may lead to violent ejection of the mixture out of the heated channel from one or both ends. Chugging seems to be the term used to describe periodic expulsion phenomena in a flow situation, while geysering often refers to no net-flow situations.

The expulsion of the fluid results from sudden vaporization. The bulk of the fluid must be therefore superheated for this vaporization to occur, hence bubble formation, growth and collapse phenomena are of importance to chugging and geysering.

Chugging and geysering cycles can be divided into an incubation, an expulsion and a refill period. The incubation period is needed to produce that superheating required for violent nucleation. Since the delay to nucleation may vary randomly, the period of chugging or geysering phenomena may be irregular.

Acoustic oscillations

Acoustic oscillations are associated with dynamic pressure waves, and their periods are of the order of magnitude of the transit time of such waves through the system. Indeed commonly observed frequencies are in the range of $10 \div 100\,\text{Hz}$.

Acoustic oscillations have been observed in subcooled boiling, bulk boiling and film boiling and generally they have small amplitudes [1]. They often seem to be triggered by or coupled to heat transfer mechanism such as subcooled boiling (collapse of the bubbles), and film boiling (variations of the film thickness and vapor generation rate owing to change in pressure).

Thermal oscillations

Thermal oscillations are related to the instability of boiling heat transfer. They are characterized by large amplitude fluctuations in the heater wall temperature. The flow oscillates between annular flow, transition boiling and droplet flow at a given point and thus produces large amplitude temperature oscillations. Density wave oscillations are required to trigger the thermal oscillations [2].

1.4 Two-phase flow instability analysis

Every study on the dynamics of two-phase flow starts from the analytical expression of the conservation laws and from a specification of the boundary conditions. The system of resulting equations must be closed by specifying an appropriate number of constitutive laws.

Two general approaches are possible for the thermohydrodynamic stability analyses:

- time-domain (direct numerical analysis), non-linear models
- frequency-domain, linearized models

In time-domain analyses the conservation equations for two-phase flow are solved directly by numerical methods. For this kind of models the stability analysis is performed like described below.

The steady state is perturbed with small stepwise changes of some operating parameter simulating an actual transient, such as power escalation in a real system. The stability threshold is reached when undamped or diverging oscillations appear following such a small change. Stability can also be investigated by temporarily perturbing the steady state, for example, with a delta-function variation of a boundary condition.

Time-domain techniques are very time consuming when used for stability analyses, since a large number of cases must be run to produce a stability map, and each run is itself time consuming because of the limits on the allowable time step. It is also sometimes difficult to clearly distinguish between the true hydrothermodynamic oscillations and numerical instabilities.

In frequency-domain analyses the conservation equations and the necessary constitutive laws governing fluid flow (and heat transfer) are linearized around an operating point. The resulting linear equations are used to perform the stability analysis as described below.

The linear differential equations are Laplace-transformed and the transfer functions that can be obtained in this manner are used to arrive at a stability evaluation of the system using classic control-theory techniques. This method can predict only

the threshold of instability since the characteristics of the limit-cycle oscillation appearing beyond this threshold can be obtained only from non linear models of the system.

The method is inexpensive with respect to computational time, relatively straightforward to implement, yields results that are easy to interpret, and is free from numerical stability problems of finite-difference (and finite-element) techniques.

1.4.1 Stability Maps

The stability features of a two-phase flow system can be efficiently described by means of the so-called stability maps. These charts are useful instruments that describe the stability characteristics of the boiling system in terms of the externally imposed parameters.

The operating state of a boiling channel is, indeed, generally specified by the following parameters:

- fluid;
- channel geometry (length, hydraulic diameter, heated perimeter, frictional characteristics, local variations of geometry, etc...);
- operating pressure level;
- axial linear heat input distribution $q'(z)$ and total heat input q;
- flow rate w or, alternative, channel pressure drop Δp;
- coolant inlet temperature T_{in} or inlet subcooling Δh_{in} (in enthalpy units).

For stability investigations, the first three items in the list and the axial heat input distribution are generally specified. The regions of stable and unstable operation must therefore be found in the three-dimensional space $(w, q, \Delta h_{in})$. A mapping of these regions in two dimensions is referred to as the stability map of the system.

It is so clear that there is no universal stability map. Furthermore, the stability boundary in the $(w, q, \Delta h_{in})$ space is a surface and can be represented only by a family of curves in any two dimensional map. Several such alternative representations are

possible. Although no unique pair of non-dimensional parameters describes completely the behavior of a given system, an opportune choice of non-dimensional parameters can lead to a clustering of the family of stability lines useful in understanding system behavior.

Two useful couples of non-dimensional parameters have been proposed [1].

The first one is formed by the non-dimensional enthalpy difference and the non-dimensional subcooling defined respectively as:

$$\frac{q}{w\,h_{LV}} \qquad \frac{\Delta h_{in}}{h_{LV}} \tag{1.11}$$

where h_{LV} is the heat of vaporization, equal to $h_V - h_L$.

The second one is formed by the phase change number N_{pch} and the subcooling number N_{sub}. The phase change number is the ratio of the characteristic frequency of phase change Ω to the inverse of a single-phase transit time in the system.

The characteristic frequency of phase change Ω is defined as:

$$\Omega = \frac{q'''}{h_{LV}}\, v_{LV} = \frac{q'''}{h_{LV}}\,(v_V - v_L)$$

where $v_{LV} = (v_V - v_L)$ is the volume change resulting from vaporization and q''' is the heat input per unit volume of fluid. Therefore the phase change number and the subcooling number are respectively:

$$\begin{aligned} N_{pch} &= \frac{\Omega}{V_{in}/L_h} = \frac{q}{w\,h_{LV}}\,\frac{v_{LV}}{v_L} \\ N_{sub} &= \frac{\Delta h_{in}}{h_{LV}}\,\frac{v_{LV}}{v_L} \end{aligned} \tag{1.12}$$

where V_{in} is the inlet velocity and L_h is the heated length.

At a given pressure level, the $\left(q/wh_{LV},\, \Delta h_{in}/h_{LV}\right)$ and $\left(N_{pch},\, N_{sub}\right)$ maps are identical. The advantage of the latter parameters couple is that they include the effects of pressure variation.

Figure 1.6 shows a qualitative stability map for boiling systems. The constant-mass-flux and the costant-heat-flux threshold lines are clustered together.

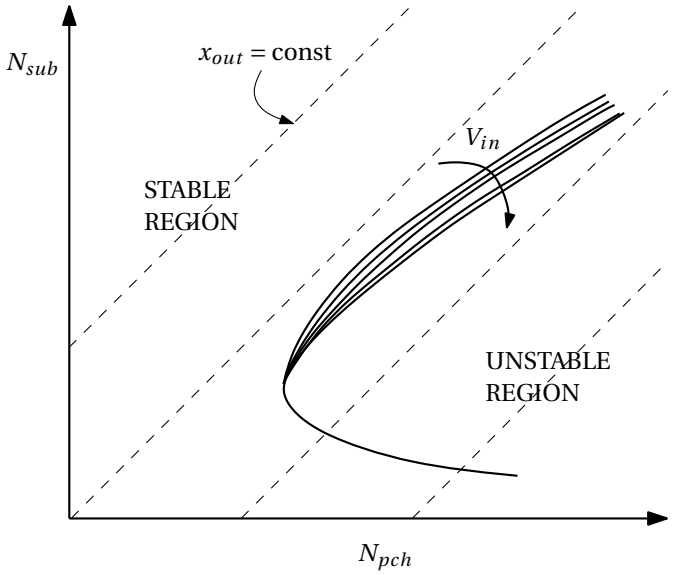

Figure 1.6: A typical stability map for a boiling channel.

1.4.2 Effect of parameters on the stability

In this section the effects of main parameters influencing the stability of boiling systems are summarized.

Effect of heat input, flow rate and exit quality

A stable system is brought into unstable operating region by increases in the heat input or decreases in flow rate; both effects increase the exit quality.

Figure 1.7 shows the various perturbations in the complex plane during an increase of heat flux at constant mass flux and constant inlet subcooling. The perturbation vectors clearly rotate as the heat flux is increased. The single-phase pressure drop perturbation does not depend much on the heat flux since it is essentially controlled by the inlet throttling. The two-phase pressure drop perturbation grows and rotates with increases in the heat flux and at the threshold becomes equal but opposite in direction to the single-phase perturbation.

The destabilizing effect of increasing the ratio q/w are universally accepted. Stability experiments conducted at constant heat input and constant inlet subcooling has shown that the reduction of the flow rate brings the system into the unstable region [1].

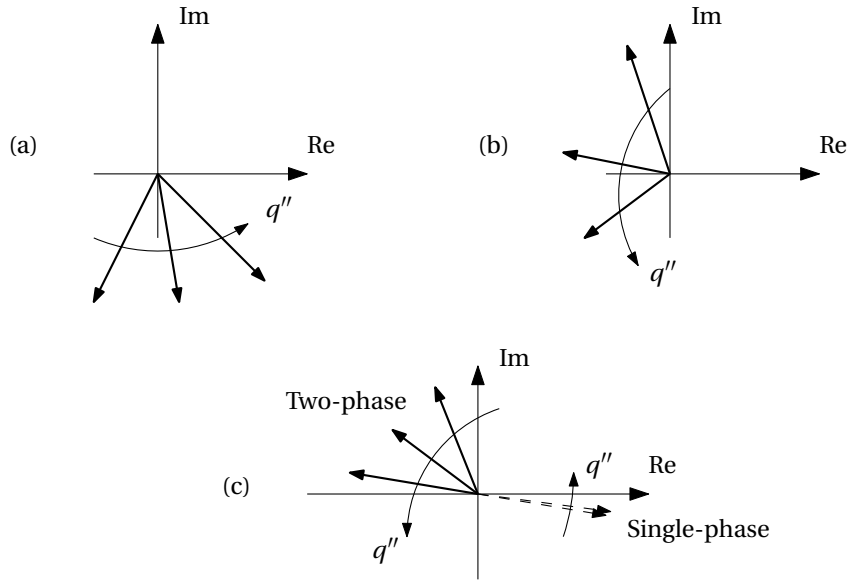

Figure 1.7: Variation of the perturbations in the complex plane as the threshold power is approached (at constant mass flux). (a) Perturbation of the boiling boundary $\delta z_{bb}/\delta w$. (b) Perturbation of the exit flow rate $\delta w_{out}/\delta w$. (c) Pressure drop in single-phase and two-phase region $\delta\Delta p/\delta w$.

Effect of pressure level

An increase in pressure level is in general stabilizing. At constant values of the dimensionless enthalpy difference and subcooling, that is, at constant dimensionless inlet subcooling and exit quality, the pressure effect is made apparent by the density ratio v_{LV}/v_L appearing in the definitions (1.12) of phase change and subcooling number.

Although these two dimensionless number do not describe completely all the effects of the pressure level on the stability of the system, stability boundaries at three different pressure levels could not be differentiated in the (N_{pch}, N_{sub}) plane. Thus the density ratio v_{LV}/v_L (approximately equal to ρ_L/ρ_V) could be used to extrapolate data obtained at a given pressure level and produce a map for a different pressure level.

Effect of inlet subcooling

The effect of inlet subcooling is stabilizing at high subcoolings and destabilizing at low subcoolings as shown in Figure 1.6.

Intuitively this effect may be explained by the fact that, as we increase or decrease the inlet subcooling, the two-phase channel tends towards stable single-phase liquid and vapor operation, respectively. Thus both increases and decreases of subcooling tend to pull the system out of the unstable two-phase operating mode.

The value of the inlet subcooling determines the location of the boiling boundary. In turn the phase and the amplitude of the oscillations of the boiling boundary depend on the length of the single-phase region. The location and the behavior of the boiling boundary control to a large extent the phase of the exit flow rate perturbation and the stability of the system.

Effect of nonuniform, axial, heat input distribution

The axial heat input distribution in BWRs is often assumed to be a cosine distribution. In steam generators the heat flux peaks generally near the inlet of the channel.

The effect of a cosine distribution is to move the boiling boundary toward the center of the channel; this has an effect on the length of the single-phase region and on the phase of the oscillation of the boiling boundary. The effect seems to be largest and most destabilizing when the boiling boundary is high in the channel. Thus the cosine distributions could be moderately stabilizing at low subcoolings and destabilizing at high subcoolings [1].

This effect is illustrated in Figure 1.8 and can also be explained with the established effect of inlet subcooling. Indeed, lowering a high subcooling brings the boiling boundary down toward the center of the channel, much the same way that the cosine distribution does at high subcooling.

The effect of nonuniform distributions on pressure drop is generally minor, since most of the two-phase pressure drop takes place near the exit of the channel, where the quality (at constant power) is independent of the heat flux distribution.

Effect of inlet and exit throttling

The effect of inlet (single-phase) throttling is always strongly stabilizing and is used to assure the stability of otherwise unstable channels. On the contrary, the effect of flow resistances near the exit of the channel (two-phase flow region) is strongly

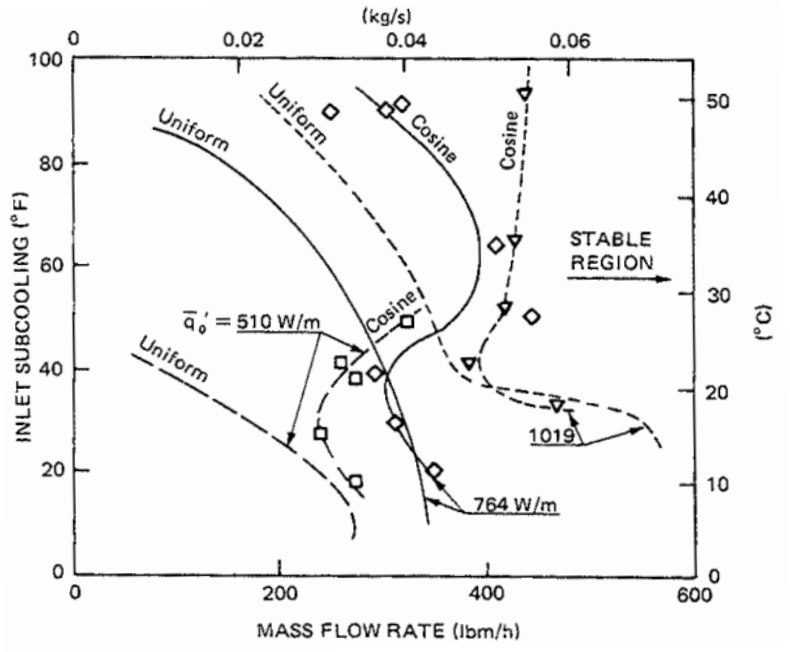

Figure 1.8: Comparison of the stability boundaries obtained obtained with a uniform and a cosine heat input distribution at three different power levels.

destabilizing. For example, stable channels can become unstable if an orifice is added at the exit, or a riser section is provided.

These effects can be understood by examining the pressure drop perturbations of Figure 1.7. Starting from a low power level, the threshold of instability is crossed when the single-phase and the two-phase pressure perturbations become equal but diametrically opposed in the complex plane. Figure 1.7 shows how the two-phase pressure drop perturbation grows progressively and finally matches the single-phase pressure drop perturbation as the power level is increased. It is evident that any increase of the single-phase term will retard, while increases of the two-phase term will precipitate crossing the threshold.

1.5 Conclusions

Three main instability types have been described rather extensively.

The first one is a static one and is related to the pressure drop versus flow rate characteristic curve shape of the two-phase system.

The latter ones are dynamic ones and they are linked to perturbation propagation

phenomena in two-phase flow because feedback mechanisms involve delays created by the finite propagation time of perturbations in the system.

While static instabilities can be studied by means of static considerations only, dynamic ones must be studied using time dependent flow models. Such a study can be carried on using both non-linear or linearized models.

Whatever the adopted technique is, a stability map of the system can be drawn in the space of the input parameters that physically influence the stability of the system in different manners. Stability maps can be used to deduce how a parameter actually influence the system stability.

Bibliography

[1] J.M. Delhaye et al. *Thermohydraulics of two-phase systems for industrial and nuclear engineering*. Hemisphere, 1981.

[2] S. Kakac and B. Bon. A review of two-phase flow dynamic instabilities in tube boiling systems. *International Journal of Heat and Mass transfer*, 2007.

Chapter 2

Modeling steam and water mixtures flowing through heated channels

Abstract

A one dimensional model able to describe water and mixtures of steam and water flowing through heated channels has been developed.

This task has been achieved with a procedure which can be divided in three different steps.

The first step is the set up of a mathematical model. Mass, moment and energy balance equations have been deduced for the physical system: a monodimensional circular heated pipe. Closure equations have been collected on the basis of the hypotheses made and they have been used to close the equations set so as to complete the mathematical formulation of the problem.

In the second step the mathematical model has been translated in a computer language so as to compute its numerical solution. This task has been achieved mainly by means of *COMSOL Multiphysics* code.

Finally, in the last step, numerical results have been compared with some experimental data collected at SIET thermal hydraulic laboratories in Piacenza (Italy).

2.1 Introduction

In the present chapter the creation of a mathematical model able to reproduce the behavior of steam and water mixtures flowing through heated channels is illustrated.

First of all, a set of mathematical equations and empirical relations has been deduced to mathematically formulate the problem. The deduction of such equations required simplifying hypothesis both physical and geometrical. Obviously these assumptions, adopted to conciliate calculations accuracy and simplicity, irrevocably outline model validity limits.

Secondly, the equation system has been implemented by means of an adequate computer language in order to calculate the numerical solution of the mathematical problem.

Finally, the model has been validated by means of comparison between experimental data and simulated data obtained in the same conditions. Experimental data have been collected thanks to experiences carried out at SIET thermal hydraulics laboratories in Piacenza (Italy). The experimental campaigns have been conducted on a helically coiled steam generator prototype, built for innovative nuclear reactor studies.

A detailed description of each of these stages is presented in the following sections.

2.2 The mathematical model

Models used to describe the behavior of phase changing fluids flowing through heated channels derive from two main assumptions: the existence or not of thermodynamic equilibrium and the existence or not of slip between the two phases.

Whatever the assumption made are, all models are constituted by mass, momentum and energy balance equations for the fluid together with the initial and boundary conditions and the model closure equations.

A first division which can be made among these models is between mixture models and multi-fluid models.

Mixture models are usually those models in which the hypothesis of thermody-

namic equilibrium between the two phases is assumed.

The simplest one is the *Equilibrium Homogeneous Model* (HEM). It assumes that there is no relative velocity between the two phases (homogeneous flow) and that the vapor and liquid are in thermodynamic equilibrium. In this case mass, momentum and energy balance equations of the mixture are sufficient to describe the flow for certain conditions.

Mixture models other than HEM add some complexity to the two-phase flow description. A well known example for such mixture models is the *Thermal Equilibrium Drift Flux Model*, which allows the vapor velocity to be different from that of the liquid by providing an algebraic relation for the velocity differential between the two phases.

In the *Two-fluid Model*, three conservation equations are written both for the vapor and the liquid phases and there is not any restriction about both the thermodynamic and the velocity conditions. This model allows a more general description of the two-phase flow. However it requires a larger number of constitutive equations.

In the present work the *Thermal Equilibrium Drift Flux Model* has been chosen to model the velocity difference between the two phases. The reasons for that choice are that this model allows to realize a good compromise between results accuracy and simplicity in the calculations.

Later on, the basic assumptions made and the equations set are illustrated in detail.

2.2.1 Basic assumptions

The physical system modeled is made by a straight duct of length L with circular section of diameter D and slope angle θ (with respect to the horizontal direction).

It is assumed that the fluid flowing through the channel is water and that the system is uni-dimensional.

From the computational point of view, the latter assumption allows to realize a simpler system which can reasonably represents physical systems of interest: their length is usually much greater than the (hydraulic) diameter.

The value of the generic property $c(z,t)$ (like h, p, T, ...) in the point of spatial

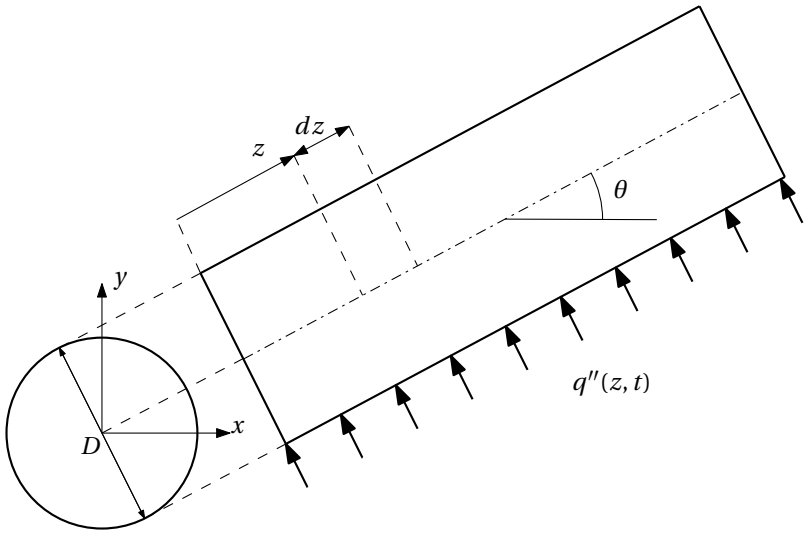

Figure 2.1: A schematic representation of the modeled physical system.

coordinate z, evaluated at time t, is assumed to be uniform on the section and equal to its mean value on it. Therefore:

$$c(z,t) = \frac{1}{A_z} \iint_{A_z} c(x,y,z,t)\, dx\, dy$$

where A_z is the surface of the transversal section corresponding to the same z coordinate.

The system heating is obtained by means of an externally imposed heat flux[1] $q''(z,t)$, while axial heat conduction and heat losses towards the ambient are neglected.

A sketch of the system is illustrated in Figure 2.1.

2.2.2 Conservation equations

The mass, momentum and energy balance equations form depends on the physical state of the fluid.

In a single-phase flow, the mass, momentum and energy balance equations take, for the physical system considered, the following form:

$$\frac{\partial \rho}{\partial t} + \frac{\partial G}{\partial z} = 0 \tag{2.1}$$

[1] if the system works with an external imposed temperature, the heat flux term has to be adequately replaced.

$$\frac{\partial G}{\partial t} + \frac{\partial}{\partial z}\left(\frac{G^2}{\rho}\right) = -\frac{\partial p}{\partial z} - \rho\, g\, \sin\theta - \left(\frac{\partial p}{\partial z}\right)_{\text{fric}} \tag{2.2}$$

$$\frac{\partial}{\partial t}\left(\rho\, h - p + \frac{G^2}{2\,\rho}\right) + \frac{\partial}{\partial z}\left(G\, h + \frac{G^3}{2\,\rho^2}\right) = q''\,\frac{P}{A} + \frac{G}{\rho}\left(\frac{\partial p}{\partial z}\right)_{\text{fric}} - G\, g\, \sin\theta \tag{2.3}$$

In place of the equation (2.3) an enthalpy balance equation can be used. This one can be obtained manipulating equation (2.2) in a convenient way and subtracting it from equation (2.3), and takes the following form:

$$\frac{\partial}{\partial t}(\rho\, h - p) + \frac{\partial}{\partial z}(G\, h) = q''\,\frac{P}{A} + \frac{G}{\rho}\left[\left(\frac{\partial p}{\partial z}\right)_{\text{fric}} + \frac{\partial p}{\partial z}\right] \tag{2.4}$$

The term $\left(\partial p/\partial z\right)_{\text{fric}}$, present in equations (2.2), (2.3) and (2.4), represents the pressure drop due to the friction between the fluid and the channel wall. Its evaluation requires specific models and empiric correlations which will be specified later.

In a two-phase flow, the mass, momentum and energy balance equations take, instead, the following form:

$$\frac{\partial \rho_m}{\partial t} + \frac{\partial G}{\partial z} = 0 \tag{2.5}$$

$$\frac{\partial G}{\partial t} + \frac{\partial}{\partial z}\left(\frac{G^2}{\rho_m^+}\right) = -\frac{\partial p}{\partial z} - \rho_m\, g\, \sin\theta - \left(\frac{\partial p}{\partial z}\right)_{\text{fric}}^{\text{TP}} \tag{2.6}$$

$$\frac{\partial}{\partial t}\left(\rho_m\, h_m - p + \frac{G^2}{2\,\rho_m^+}\right) + \frac{\partial}{\partial z}\left[G\, h_m^+ + \frac{G^3}{2\,(\rho_m^2)^+}\right] = q''\,\frac{P}{A} + \frac{G}{\rho_m}\left(\frac{\partial p}{\partial z}\right)_{\text{fric}}^{\text{TP}} - G\, g\, \sin\theta \tag{2.7}$$

Although equations (2.1), (2.2) and (2.3) have the same form of equations (2.5), (2.6) and (2.7), the quantities present in them are characteristic of two-phase mixtures:

- ρ_m and ρ_m^+ represent the static and the dynamic density respectively;
- h_m and h_m^+ respresent the static and the dynamic enthalpy respectively.

As for equations (2.3) and (2.4), also equation (2.7) can be replaced by an enthalpy balance equation: indeed, the kinetic energy terms in equation (2.7) can be eliminated with a procedure similar to the one used for equation (2.3). Such equation is:

$$\frac{\partial}{\partial t}\left(\rho_m\, h_m - p\right) + \frac{\partial}{\partial z}\left(G\, h_m^+\right) = q''\,\frac{P}{A} + \frac{G}{\rho_m}\left[\left(\frac{\partial p}{\partial z}\right)_{\text{fric}}^{\text{TP}} + \frac{\partial p}{\partial z}\right] \tag{2.8}$$

Also for the $\left(\partial p/\partial z\right)_{\text{fric}}^{\text{TP}}$ present in equations (2.6), (2.7) and (2.8) specific models and empirical correlations must be used. They will be explained later.

Finally it should be noted that in equations (2.3) and (2.4) and in equations (2.7) and (2.8) the heat flux q'' can be replaced by a convenient relation if the channel is heated as an imposed temperature system, like in a steam generator or a generic heat exchanger, rather than as an imposed heat flux system.

The equations (2.1), (2.2), (2.3) and (2.4) and the equation (2.5), (2.6), (2.7) and (2.8) have, as already mentioned, the same mathematical form. Hence a mathematical model valid both for a single-phase fluid and for a two-phase fluid can be obtained using equation (2.5), (2.6), (2.7) and (2.8) and noting that for a subcooled liquid or a superheated vapor:

$$\rho_m = \rho_m^+ = \rho$$
$$h_m = h_m^+ = h$$

2.2.3 Initial and boundary conditions

Three initial and three boundary conditions are required for the three differential equations (2.5), (2.6) and (2.8) in order to make the mathematical problem a well placed problem.

Initial conditions must be specified for three state variables: their spatial distribution at the initial time t_0 has to be known to find out the evolution of the system.

Boundary conditions are constraints applied at the system boundaries (i.e. channel entrance and exit sections). Three kind of boundary conditions can be specified:

- Dirichlet boundary conditions: these are the ones that fix the values of some quantities at the domain borders;
- Neumann boundary conditions: these are the ones that impose a constraint on the conservative fluxes at the domain borders;
- Robin boundary conditions: these are a combination of conditions between the previous ones.

Anyway, regarding the heated channel, it can be solved by two methods, namely, either by specifying the inlet flow, or the pressure drop across, the channel. Each method has its own set of boundary conditions.

The first boundary condition, the inlet subcooling, and the second boundary condition, the inlet pressure, are identical in both methods.

For the method in which the flow rate is specified, the third boundary condition is the exit pressure, which comes out directly from the specified pressure drop across the heated channel.

2.2.4 Constitutive laws

Two kinds of constitutive laws are necessary: the relations which provide fluid thermodynamical properties, namely, the state equations, as well as the relations which provide fluid physical properties.

In a single-phase flow condition, fluid thermodynamical properties depend on two unrelated quantities: indeed, according to the Gibb's law, the fluid has two degrees of freedom. Therefore the state equations used are:

$$\rho = \rho(p, h) \tag{2.9}$$

$$T = T(p, h) \tag{2.10}$$

In a two-phase flow condition, instead, fluid thermodynamical properties are functions of a single parameter: each phase has, indeed, one degree of freedom. Therefore the state equations used in this case are:

$$\begin{aligned} \rho_L &= \rho_L(p) \\ \rho_V &= \rho_V(p) \end{aligned} \tag{2.11}$$

$$\begin{aligned} h_L &= h_L(p) \\ h_V &= h_V(p) \end{aligned} \tag{2.12}$$

$$T = T_{\text{sat}}(p) \tag{2.13}$$

Among the physical properties of the fluid, viscosity and surface tension are the ones that the model needs.

Viscosity depends on pressure and temperature if the phase change does not take place, it depends on pressure only if phase change occurs. Therefore, in the first case:

$$\mu = \mu(p, h) \tag{2.14}$$

and in the second case:

$$\begin{aligned} \mu_L &= \mu_L(p) \\ \mu_V &= \mu_V(p) \end{aligned} \tag{2.15}$$

Finally, surface tension used is only pressure-dependent, being the one in saturation condition. Hence, the equation used is:

$$\sigma = \sigma(p) \tag{2.16}$$

2.2.5 Closure equations

Closure equations are those ones required to solve the problem, by means of equalizing the number of equations with the number of unknown quantities.

Closure equations that the single-phase flow model requires are the ones used to describe the frictional pressure drops. No other relations are necessary.

Much more expressions are necessary to close the two-phase flow model because of its greater complexity compared with the single-phase one. In fact, the relations needed for changing phase fluid flow modeling are:

1. the expressions which defines the characteristic two-phase mixture quantities in terms of thermodynamical properties of each phase (h_L, h_V, ρ_L, ρ_V), the void fraction α, the thermodynamic quality x, the slip ratio S;

2. the $S-\alpha-x$ relation;

3. the equations given by the vapor slip model;

4. the equations given by the frictional pressure drop model.

The frictional pressure gradient in the single-phase flow systems is usually expressed by a relation like the following:

$$\left(\frac{\partial p}{\partial z}\right)_{\text{fric}} = f_M \frac{G^2}{2\,\rho\,D} \tag{2.17}$$

where f_M is the so-called Moody's friction factor (Darcy's factor kind).

The factor f_M is usually not easy to evaluate.

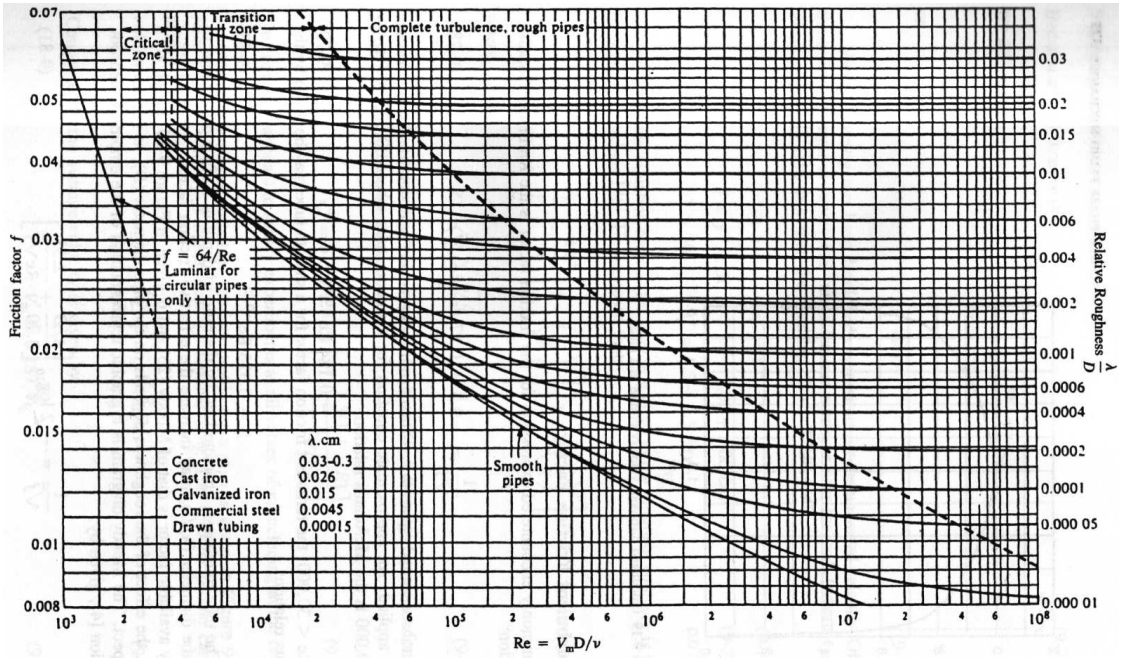

Figure 2.2: Moody's chart.

It depends on the fluid motion regime, described by the Reynolds number, and on the wall roughness, and it can be estimated by means of diagrams, like Moody's chart, represented in Figure 2.2, or by means of convenient empirical correlations.

In the case of laminar flow inside the channel the friction factor can be evaluated using the exact theoretical result, valid for circular pipes:

$$f_M = \frac{64}{\mathrm{Re}} \tag{2.18}$$

In the case of turbulent flow no exact results are available. There are several different correlations which can be used. Three of them are reported in the following.

A commonly encountered expression for the friction factor is the Karman - Nikuradse equation:

$$\frac{1}{\sqrt{f_M}} = -0.8 + 0.87 \ln\left(\mathrm{Re}\sqrt{f_M}\right) \tag{2.19}$$

This trascendental equation is difficult to use in practice and simplified relations are often applied. Approximate equations for a smooth tube are the Blausius and McAdams relations:

$$\begin{cases} f_M = 0.316 \cdot \mathrm{Re}^{-0.25} & \text{if} \quad \mathrm{Re} < 30\,000 \\ f_M = 0.184 \cdot \mathrm{Re}^{-0.2} & \text{if} \quad 30\,000 < \mathrm{Re} < 1\,000\,000 \end{cases} \tag{2.20}$$

Finally, the tube roughness, characterized by the ratio of depth of surface protrusion to tube diameter (λ/D), can be taken into account using the Colebrook equation:

$$\frac{1}{\sqrt{f_M}} = -2\log_{10}\left[\frac{\lambda/D}{3.70} + \frac{2.51}{\mathrm{Re}\sqrt{f_M}}\right] \tag{2.21}$$

Let us now specify the relations needed to close the two-phase flow model.

First of all the quantities ρ_m, ρ_m^+, h_m, h_m^+ need to be specified, as said before, in terms of h_L, h_V, ρ_L, ρ_V, α and x:

$$\rho_m = \alpha\,\rho_V + (1-\alpha)\,\rho_L \tag{2.22}$$

$$\rho_m^+ = \left[\frac{x^2}{\alpha\,\rho_V} + \frac{(1-x)^2}{(1-\alpha)\,\rho_L}\right]^{-1} \tag{2.23}$$

$$h_m = \frac{\alpha\,\rho_V\,h_V + (1-\alpha)\,\rho_L\,h_L}{\rho_m} \tag{2.24}$$

$$h_m^+ = x\,h_V + (1-x)\,h_L \tag{2.25}$$

Moreover, the $S-\alpha-x$ relation is:

$$\alpha = \left[1 + \frac{1-x}{x}\,\frac{\rho_V}{\rho_L}\,S\right]^{-1} \tag{2.26}$$

The value of the slip ratio S depends on the chosen two-phase flow model. In the *Thermal Equilibrium Drift Flux Model* case it can be expressed by the following relation [1]:

$$S = C_0 + \frac{(C_0-1)\,x\,\rho_L}{(1-x)\,\rho_V} + \frac{V_{vj}\,\rho_L}{(1-x)\,G} \tag{2.27}$$

The quantities C_0 and V_{vj} indicate respectively the concentration parameter and the effective drift flux velocity: the first one represents the global effect due to nonuniform void distribution and velocity profiles on the channel section, the second one represents the local relative velocity effect.

For the calculation of the concentration parameter several correlations exist. A general expression for all flow regimes has been suggested by Dix [1] and has been used in the present work. It is given by:

$$C_0 = \beta\left[1 + \left(\frac{1}{\beta} - 1\right)^b\right] \tag{2.28}$$

where:

$$b = \left(\frac{\rho_V}{\rho_L}\right)^{0.1} \tag{2.29}$$

while β is the volumetric ratio, given by:

$$\beta = \left[1 + \frac{1-x}{x}\frac{\rho_V}{\rho_L}\right]^{-1} \tag{2.30}$$

So as for the concentration parameter C_0 as for the effective drift velocity V_{vj} several correlations exist. Nevertheless, unlike for the C_0 parameter, a general expression valid in any flow regime for V_{vj} is not known; hence its expression has to be selected case by case.

Some expressions valid for different flow regimes are the following [2]:

- *Bubbly flow:*
$$V_{vj} = \sqrt{2}\left[\frac{(\rho_L - \rho_V)\, g\, \sigma}{\rho_L^2}\right]^{1/4} (1-\alpha)^{0.75} \tag{2.31}$$
- *Slug flow:*
$$V_{vj} = 0.37\left[\frac{(\rho_L - \rho_V)\, g\, D}{\rho_L}\right]^{1/2} \tag{2.32}$$
- *Churn flow:*
$$V_{vj} = \sqrt{2}\left[\frac{(\rho_L - \rho_V)\, g\, \sigma}{\rho_L^2}\right]^{1/4} \tag{2.33}$$
- *Annular flow:* in this flow regime the local relative velocity can be approximated to be zero, resulting in $V_{vj} \approx 0$.

Finally, frictional pressure drop relations need to be specified to close the model.

Two-phase frictional pressure drop can be modeled according to two different approaches.

The first one, the *liquid-only* approach, consists in relating two-phase pressure drop to single-phase one due to an identical flow rate supposed to be liquid (or vapor) only. This relation is represented by their ratio, the so-called friction factor multiplier ϕ_{lo}^2:

$$\left(\frac{\partial p}{\partial z}\right)_{\text{fric}}^{\text{TP}} = \phi_{lo}^2 \left(\frac{\partial p}{\partial z}\right)_{\text{fric}}^{lo} = \phi_{lo}^2 f_{lo} \frac{G^2}{2\,\rho_L D} \tag{2.34}$$

where f_{lo} represents Moody's friction factor of the liquid-only equivalent flow rate.

The second approach (*only-liquid*), instead, consists in relating the two-phase friction pressure drop to the pressure drop of the liquid or of the vapor as it were the only fluid in the channel. The choice between those last two options is usually

taken according to the system that is going to be modeled. For example, the two-phase pressure drop of a boiling fluid are usually related to the liquid ones, while the two-phase pressure drop of a condensing fluid is usually related to the vapor ones. Anyway, following this approach, the friction pressure drop is given by:

$$\left(\frac{\partial p}{\partial z}\right)_{\text{fric}}^{\text{TP}} = \phi_l^2 \left(\frac{\partial p}{\partial z}\right)_{\text{fric}}^{L} = \phi_v^2 \left(\frac{\partial p}{\partial z}\right)_{\text{fric}}^{V} \tag{2.35}$$

Diagrams and empiric correlations are available to estimate the two-phase friction factor multipliers ϕ_{lo}^2, ϕ_v^2, ϕ_l^2.

In the present work the first approach has been chosen. Hence only some diagrams and correlations to compute ϕ_{lo}^2 are reported later on.

A first simple expression for ϕ_{lo}^2 factor is Becker's correlation, valid for qualities smaller than 30 % and for pressures greater than 70 bar [3]:

$$\phi_{lo}^2 = 1 + 10\, x\, \frac{p_{\text{crit}}}{p} \tag{2.36}$$

Another quite simple correlation is the expression proposed by Jones [1]:

$$\phi_{lo}^2 = 1.2 \left(\frac{\rho_L}{\rho_V} - 1\right) x^{0.824} + 1.0 \tag{2.37}$$

This expression is an analytical form of the Martinelli-Nelson diagram showed in Figure 2.3.

However this expression does not take into account of the flow rate effect which can be introduced by means of a corrective factor:

$$\phi_{lo}^2 = \Omega(p, G) \left[1.2 \left(\frac{\rho_L}{\rho_V} - 1\right) x^{0.824}\right] + 1.0 \tag{2.38}$$

where $\Omega(p, G)$ is given by [1]:

$$\Omega(p, G) = \begin{cases} 1.36 + 0.0005\, p + 0.1 \left(\dfrac{G}{10^6}\right) - 0.000714\, p \left(\dfrac{G}{10^6}\right) & \text{if} \quad \left(\dfrac{G}{10^6}\right) \leq 0.7 \\ \\ 1.26 - 0.0004\, p + 0.119 \left(\dfrac{10^6}{G}\right) + 0.00028\, p \left(\dfrac{10^6}{G}\right) & \text{if} \quad \left(\dfrac{G}{10^6}\right) > 0.7 \end{cases} \tag{2.39}$$

in which G is in $\text{lb}\,\text{ft}^{-2}\,\text{h}^{-1}$ and p is in psia.

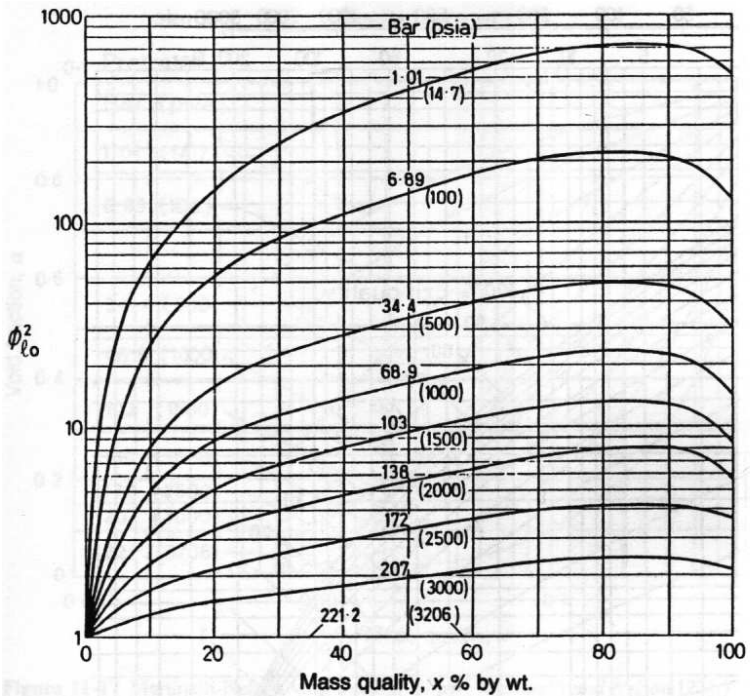

Figure 2.3: Martinelli-Nelson's ϕ^2_{lo} as a function of quality and pressure.

2.3 Model implementation

The implementation of the mathematical model illustrated in the previous section has been done firstly by the implementing thermodynamical and physical properties and then by implementing the equations set. Everything has been made by means of *COMSOL Multiphysics* code.

COMSOL Multiphysics is an interactive system capable to solve the mathematical problems based on partial differential equations using the finite element method. This characteristic renders it particularly suitable to solve scientific and engineering problems: indeed, apposite modules allow to cope with acoustic or electromagnetic problems, with chemical or thermodynamical problems.

Later on, the procedure used for this purpose is described in detail.

2.3.1 Implementation of thermodynamical and physical properties

Data provided by IAPWS (*"International Association for the Properties of Water and Steam"*) have been used to implement water thermodynamical and physical properties of interest. These data have been used by means of *XSteam for Matlab*.

XSteam for Matlab is an implementation of the data provided by IAPWS IF97 standard formulation. It provides accurate data for water and steam and mixtures of water and steam properties from 0 to 1000 bar and from 0 to 2000 °C. It is programmed as a Matlab .m file.

Using *XSteam for Matlab*, files containing IAPWS's data have been created. The reason of that is the following: *COMSOL Multiphysics* provides a tool to create functions by interpolation of external data. By using this tool, thermodynamical and physical properties of interest have been arranged in a suitable form for COMSOL compiler.

Equations (2.9), (2.10), (2.11), (2.12) and (2.13) have been implemented using this procedure, illustrated more in detail in [4].

Two examples of Matlab script used to generate the data file inserted in COMSOL are now shown. The following sample script has been used to create functions of one variable ($\rho_L(p)$ in this case):

```
p = [1:1:220];
rhoL = zeros(1,length(p));
for i=1:length(p)
    rhoL(i) = XSteam('rhoL_p',p(i));
end
postwriteinterpfile('rhoL_p.txt',p*1e5,rhoL);
```

Instead, the following one has been used to generate two-variable functions data files ($\rho(p,h)$ in this case):

```
p = [1:1:220];
h = [50:20:3000];
rho_ph = zeros(length(p),length(h));
for i=1:length(p)
    for j=1:length(h)
        rho_ph(i,j) = XSteam('rho_ph',p(i),h(j));
    end
end
```

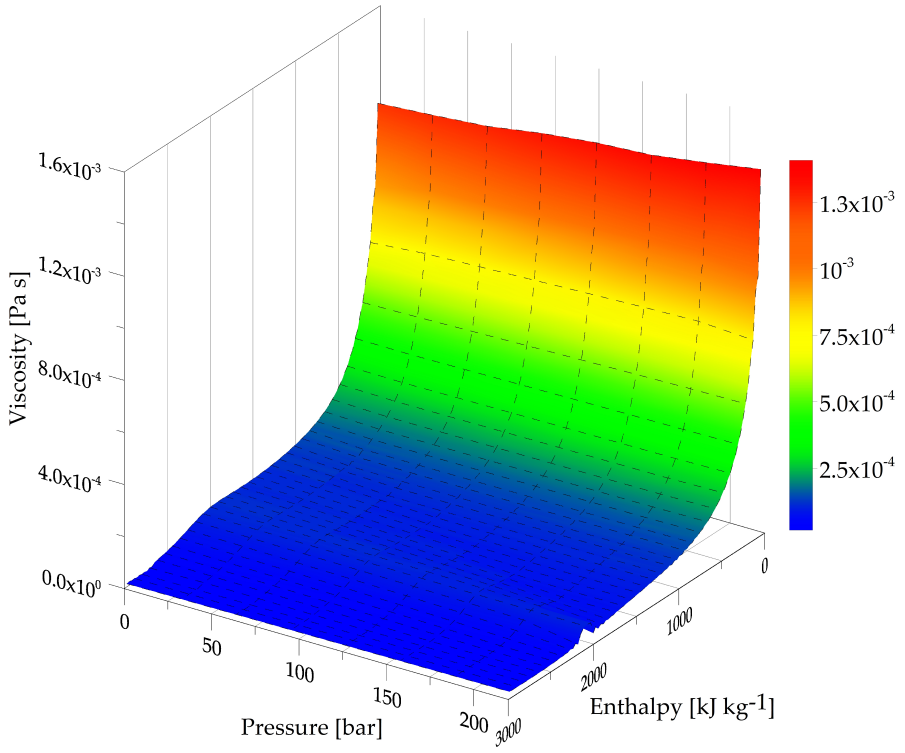

Figure 2.4: IAPWS's water viscosity data.

```
postwriteinterpfile('rho_ph.txt',p*1e5,h*1e3,rho_ph);
```

A different procedure has been used for water viscosity.

In a single-phase condition, an accurate analysis of IAPWS data has shown that water viscosity dependence on pressure can be ignored compared to its dependence on enthalpy. This fact can be easily shown observing Figure 2.4. Therefore, the implementation of equation (2.14) has been done such as viscosity were a function of a single independent variable, the enthalpy indeed.

In the two-phase condition the implementation of equations (2.15) has been done manually, using data provided by Caruso [3]. In fact, *XSteam for Matlab* does not provide viscosity data for those conditions. The functions obtained are shown in Figure 2.5.

2.3.2 Equations implementation

The implementation of the equations set has been done using *COMSOL Multiphysics*. The tool used for this purpose is the *PDE General Form* module which allows

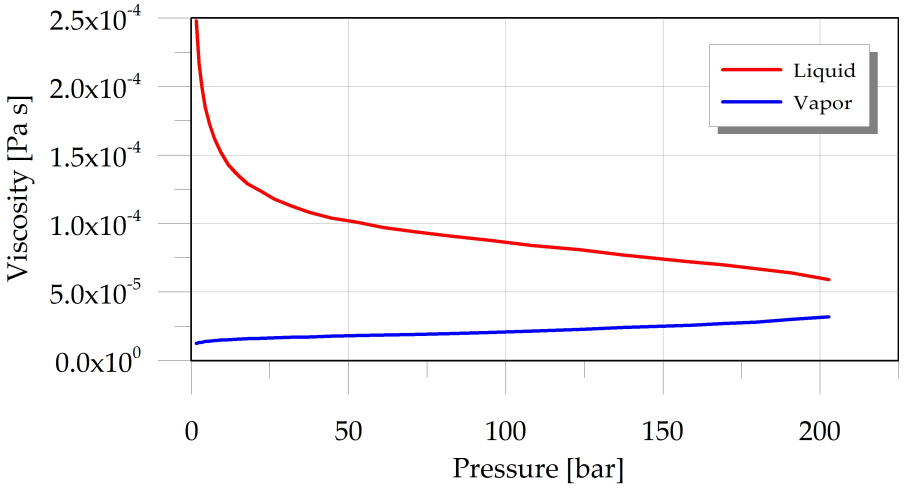

Figure 2.5: Function obtained by means of interpolation of water viscosity data.

the translation of the equations in a language that can be interpreted by COMSOL compiler.

This tool is able to numerically solve an equations system written in the form:

$$\boldsymbol{e_a}\frac{\partial^2 \boldsymbol{u}}{\partial t^2} + \boldsymbol{d_a}\frac{\partial \boldsymbol{u}}{\partial t} + \nabla \cdot \boldsymbol{\Gamma} = \boldsymbol{F} \tag{2.40}$$

The model implemented in this work is constituted by three partial differential equations, so the equations set is a 3×3 system.

First of all, unknown vector $\boldsymbol{u}$ has been specified. The dynamic variables chosen are pressure, mass flux and dynamic enthalpy; so:

$$\boldsymbol{u} = \begin{bmatrix} p \\ G \\ h_m^+ \end{bmatrix} \tag{2.41}$$

Consequently the terms $\boldsymbol{e_a}$ and $\boldsymbol{d_a}$, also called "mass coefficients", have been set in the following way:

$$\boldsymbol{e_a} = \begin{bmatrix} 0 & 0 & 0 \\ 0 & 0 & 0 \\ 0 & 0 & 0 \end{bmatrix} \tag{2.42}$$

$$\boldsymbol{d_a} = \begin{bmatrix} \dfrac{\partial \rho_m}{\partial p} & \dfrac{\partial \rho_m}{\partial G} & \dfrac{\partial \rho_m}{\partial h_m^+} \\ \dfrac{\partial G}{\partial p} & \dfrac{\partial G}{\partial G} & \dfrac{\partial G}{\partial h_m^+} \\ \dfrac{\partial}{\partial p}(\rho_m h_m - p) & \dfrac{\partial}{\partial G}(\rho_m h_m - p) & \dfrac{\partial}{\partial h_m^+}(\rho_m h_m - p) \end{bmatrix} \tag{2.43}$$

According to equations (2.5), (2.6) and (2.8) the flux term $\boldsymbol{\Gamma}$ is given by:

$$\boldsymbol{\Gamma} = \begin{bmatrix} G \\ \dfrac{G^2}{\rho_m^+} \\ G h_m^+ \end{bmatrix} \tag{2.44}$$

The source term $\boldsymbol{F}$ is, instead, given by:

$$\boldsymbol{F} = \begin{bmatrix} 0 \\ -\dfrac{\partial p}{\partial z} - \rho_m g \sin\theta - \left(\dfrac{\partial p}{\partial z}\right)^{\mathrm{TP}}_{\mathrm{fric}} \\ q'' \dfrac{P}{A} + \dfrac{G}{\rho_m}\left[\left(\dfrac{\partial p}{\partial z}\right)^{\mathrm{TP}}_{\mathrm{fric}} + \dfrac{\partial p}{\partial z}\right] \end{bmatrix} \tag{2.45}$$

The boundary conditions can be implemented in two different ways.

The first one is the Dirichlet mode: COMSOL compiler is able to take into account of Dirichlet boundary conditions implementing the following equation system [5]:

$$\begin{cases} -n_i \Gamma_i = G_i + \left(\dfrac{\partial R_i}{\partial u_j}\right)\mu_j & \text{on } \partial\Omega \equiv \{z=0\} \cup \{z=L\} \\ R_i(u_j) = 0 & \text{on } \partial\Omega \equiv \{z=0\} \cup \{z=L\} \end{cases} \tag{2.46}$$

for $i, j = 1,2,3$, where μ_j is the Lagrange multiplier, used to adjust the flux at the boundaries G_i in order to respect the generalized Dirichlet boundary conditions specified by the user:

$$R_i(u_j) = 0 \tag{2.47}$$

The term $\left(\partial R_i / \partial u_j\right)$ is called "ideal reaction force" and n_i is the outgoing normal versor at the boundaries.

The second mode is the Neumann one. Neumann boundary conditions are taken into account by COMSOL compiler with the equations:

$$-n_i \Gamma_i = G_i \qquad \text{on } \partial\Omega \equiv \{z = 0\} \cup \{z = L\} \tag{2.48}$$

in which G_i has to be specified by the user.

Finally, closure equations have been implemented as algebraic expressions.

As said in previous section, a mathematical model valid both for a single-phase fluid and for a two-phase fluid can be obtained from the equations valid for the latter case. That model can be easily implemented, assuming:

$$\begin{cases} x = 0 \\ \alpha = 0 \\ \beta = 0 \\ \rho_m^+ = \rho_L = \rho(p,h) \\ h_m^+ = h_L = h(p,h) \\ \phi_{lo}^2 = 1 \\ f_{lo} = f_M \\ \mu = \mu_L = \mu(p,h) \end{cases} \tag{2.49}$$

when the quality is smaller than 0;

$$\begin{cases} x = 1 \\ \alpha = 1 \\ \beta = 1 \\ \rho_m^+ = \rho_V = \rho(p,h) \\ h_m^+ = h_V = h(p,h) \\ \phi_{lo}^2 = 1 \\ f_{lo} = f_M \\ \mu = \mu_V = \mu(p,h) \end{cases} \tag{2.50}$$

when the quality is greater than 1.

If the quality is greater than 0 but smaller than 1, the implemented equations are the same valid for the two-phase flow.

In order to obtain the described result in COMSOL, the check variable v_c has been introduced:

$$v_c = \frac{h_m^+ - h_L}{h_V - h_L} \tag{2.51}$$

and the condition (2.49) and (2.50) have been imposed on the basis of its value, being

$$v_c = x$$

for a two-phase flow.

2.4 Model validation

In this section the procedure used to validate the model is reported.

Such a procedure consisted in the comparison between the numerical results of steady state simulations with the experimental data obtained at SIET thermal hydraulics labs in Piacenza (Italy).

Later on the facility and the simulations run are described in detail, and the results of the comparison between numerical data and experimental data are shown as well.

2.4.1 Facility description

The facility is an helically coiled shape steam generator prototype. It is composed by a supply section and a test section.

The supply section is designed to supply a feedwater flow rate to the test section in certain conditions. The completion of this aim is assured by a booster pump and a feedwater pump (volumetric three-cylindrical pump with a maximum head of about 200 bar), while the flow rate control is performed by means of a throttling valve and a by-pass line.

The test section is constituted instead by a stainless steel tube curved in a helically shape and connected to an upper and a lower header, and is made by two contiguous and independently controllable zones:

Variable	mm
Outer diameter	17.24
Inner diameter	12.53
Coil diameter	1000
Coil pitch	800
Tube length	32 000
Tube height	8000

Table 2.1: Helical steam generator tube main data.

- the first zone, 24 m long, is used to simulate the subcooled and the two-phase zone of the steam generator;
- the second zone, 8 m long, can be used to investigate the post-dryout and the superheating zone.

Other geometric data are summarized in Table 2.1, while a sketch of the test section is shown in Figure 2.6.

The inlet bulk temperature is measured with K-type thermocouples while inlet and outlet pressures are measured by means of absolute pressure trasducers. Nine pressure taps are placed every about four meters of test section's length and they are connected by eight trasducers used for differential pressure measurement. These differential pressure trasducers (calibrated at SIET labs) provide a maximum relative uncertainty of 0.4 % both in diabatic and adiabatic runs.

The unit can be used to carry out steady state experiences both in diabatic and adiabatic conditions.

In the first case the test section is fed with subcooled water at a certain temperature by means of a preheating system. The phase change and the possible superheating are obtained via Joule effect by means of DC generators. During these experiences the inlet temperature and flow rate, the heat flux and the pressure in five different points are measured.

In the second case the test section is fed with saturated water at a certain quality thanks to the preheating system. During these experiences the inlet temperature,

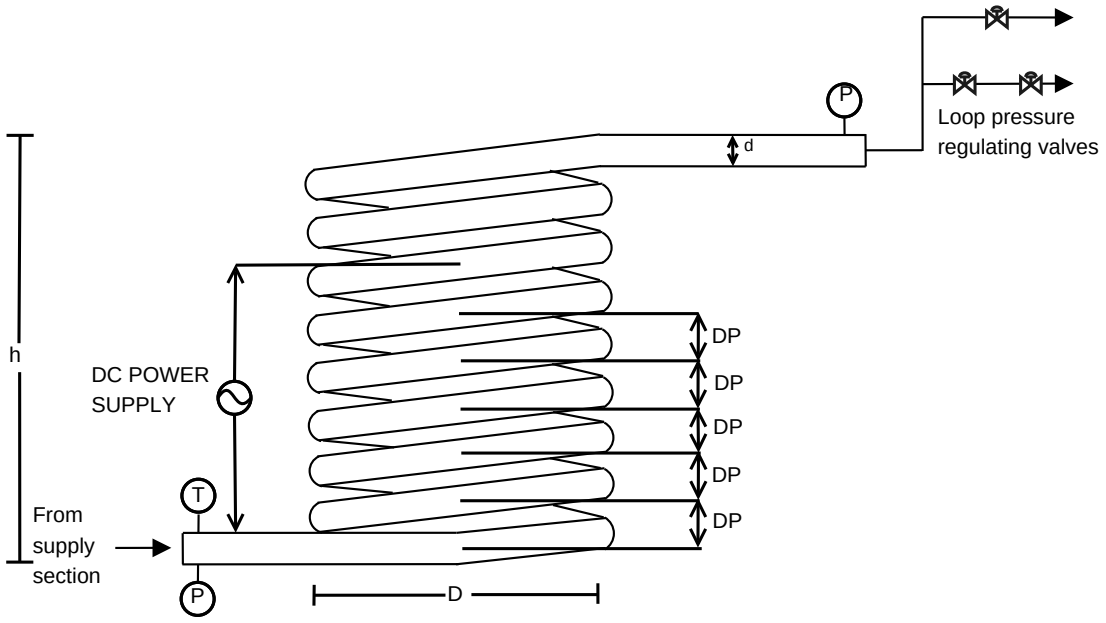

Figure 2.6: Sketch of the experimental test section.

flow rate and quality and the pressure in eight different points are measured.

2.4.2 Simulations

Simulations have been carried out adapting the built up model to the test section described before.

To do that it has been necessary, first of all, to insert the geometrical features of the test section, to adopt the correct empirical correlation for ϕ_{lo}^2, for S and finally to set the steady state regime and boundary conditions.

With regard to the geometry, the parameters D (denoted as d in Figure 2.6) and θ of equations (2.6) and (2.8) have been set equal to 12.53 mm and 14.5° respectively. The built up model is not able to take into account of helix buckling, so the slope angle of the channel has been fixed assuming the test section to be a straight channel with a slope angle equal to the mean slope of the helix:

$$\theta = \arcsin\left(\frac{h}{L_{\mathrm{SG}}}\right) = \arcsin\left(\frac{8\,\mathrm{m}}{32\,\mathrm{m}}\right) \simeq 14.5°$$

With regard to the frictional pressure drops, the coefficient ϕ_{lo}^2 has been calculated by adopting the following empirical correlation [6] (Friedel kind correlation):

$$\phi_{lo}^2 = 0.2185\,E + \frac{0.2365\,F\,H}{\mathrm{Fr}^{-0.0165}\,\mathrm{We}^{-0.1318}} \tag{2.52}$$

in which:

$$E = (1-x)^2 + x^2 \frac{\rho_L f_{vo}}{\rho_V f_{lo}}$$

$$F = x^{0.78} (1-x)^{0.224}$$

$$H = \left(\frac{\rho_L}{\rho_V}\right)^{0.91} \left(\frac{\mu_V}{\mu_L}\right)^{0.19} \left(1 - \frac{\mu_V}{\mu_L}\right)^{0.7}$$

$$\mathrm{Fr} = \frac{G^2}{g\, D\, (\rho_m^+)^2}$$

$$\mathrm{We} = \frac{G^2\, D}{\sigma\, \rho_m^+}$$

The slip has been modeled using the drift-flux relation (2.27) in which the concentration parameter C_0 has been calculated using the Dix correlation (2.28) and the effective drift velocity V_{vj} has been neglected.

With regards to the boundary condition, the system has been solved using the flow forced method: a constant flow rate is indeed provided by the supply section of the facility.

The method has been implemented as follows. At the inlet boundary ($z = 0$) the Dirichlet boundary condition mode has been set and the relation (2.47) have been specified as follows:

$$\begin{cases} R_1 = p_{in} - u_1(0) = 0 \\ R_2 = G_{in} - u_2(0) = 0 \\ R_3 = h_{in} - u_3(0) = 0 \end{cases} \tag{2.53}$$

where p_{in}, G_{in} and h_{in} are respectively the inlet pressure, mass flux and enthalpy. At the exit boundary instead the Neumann boundary conditions have been set, specifying the fluxes at the exit to be the same calculated in the point $z = L$. So the quantity G_i in the relation (2.48) has been set as follows:

$$\begin{cases} G_1 = -\Gamma_1(L) \\ G_2 = -\Gamma_2(L) \\ G_3 = -\Gamma_3(L) \end{cases} \tag{2.54}$$

In this way the conservative fluxes are free to go out from the channel.

Every simulation has been carried out with the same mesh grid consisting in 1921 points for a total number of degrees of freedom of 15364.

The measured spatial distribution of pressure has been compared with the one obtained via simulation for three different values of the inlet pressure: 20 bar, 40 bar and 60 bar.

The considered operating conditions in terms of inlet flow rate and pressure are the following ones:

- mass fluxes of 200 and 400 $\mathrm{kg\,m^{-2}\,s^{-1}}$ for an inlet pressure of 20 bar;
- mass fluxes of 200, 400, 600 and 800 $\mathrm{kg\,m^{-2}\,s^{-1}}$ for an inlet pressure of 40 and 60 bar.

With regards to heat flux, several values have been investigated. Those values depend on the flow rate:

- $q'' \sim 40 \div 60\,\mathrm{kW\,m^{-2}}$ for $G = 200\,\mathrm{kg\,m^{-2}\,s^{-1}}$
- $q'' \sim 100 \div 120\,\mathrm{kW\,m^{-2}}$ for $G = 400\,\mathrm{kg\,m^{-2}\,s^{-1}}$
- $q'' \sim 100 \div 170\,\mathrm{kW\,m^{-2}}$ for $G = 600\,\mathrm{kg\,m^{-2}\,s^{-1}}$
- $q'' \sim 150 \div 220\,\mathrm{kW\,m^{-2}}$ for $G = 800\,\mathrm{kg\,m^{-2}\,s^{-1}}$

2.4.3 Results

In the present section the results obtained from the comparison between simulated data and experimental data are shown.

Figure 2.7 shows some simulated pressure spatial distributions compared with the corresponding measured values along the channel, in particular:

- in Figure 2.7a red line and points have been obtained with:

$$\begin{cases} G = 200\,\mathrm{kg\,m^{-2}\,s^{-1}} \\ q'' = 43.68\,\mathrm{kW\,m^{-2}} \end{cases}$$

  while blue ones have been obtained with:

$$\begin{cases} G = 400\,\mathrm{kg\,m^{-2}\,s^{-1}} \\ q'' = 111.06\,\mathrm{kW\,m^{-2}} \end{cases}$$

- in Figure 2.7b red line and points have been obtained with:

$$\begin{cases} G = 600\,\mathrm{kg\,m^{-2}\,s^{-1}} \\ q'' = 142.38\,\mathrm{kW\,m^{-2}} \end{cases}$$

  while blue ones have been obtained with:

$$\begin{cases} G = 800\,\mathrm{kg\,m^{-2}\,s^{-1}} \\ q'' = 191.59\,\mathrm{kW\,m^{-2}} \end{cases}$$

- in Figure 2.7c red line and points have been obtained with:

$$\begin{cases} G = 400\,\mathrm{kg\,m^{-2}\,s^{-1}} \\ q'' = 85.17\,\mathrm{kW\,m^{-2}} \end{cases}$$

  while blue ones have been obtained with:

$$\begin{cases} G = 600\,\mathrm{kg\,m^{-2}\,s^{-1}} \\ q'' = 117.39\,\mathrm{kW\,m^{-2}} \end{cases}$$

Figure 2.8 shows the simulated temperature distributions in the same conditions. Used colors refer to the same operative conditions listed before.

Figure 2.9 shows instead the comparison between numerical results and experimental data for the different inlet pressures experienced.

The agreement between experimental data and simulated data is very satisfying. Indeed, as Figures 2.7 and 2.9 show, simulations are able to reproduce the examined experimental data with a maximum error lower than 10 %. This can be considered a good result taking into account the simplicity of the model and its implementation.

2.5 Conclusions

The validation procedure has shown the fairness of the modelistic hypotheses adopted and of the tools employed to get numerical results.

The built up model, although deduced on the basis of strong simplifying hypotheses, has allowed to obtain good results. It means that the hypotheses of one dimensional flux and of thermal equilibrium between vapor and liquid phases can be considered acceptable for the purposes of the present work.

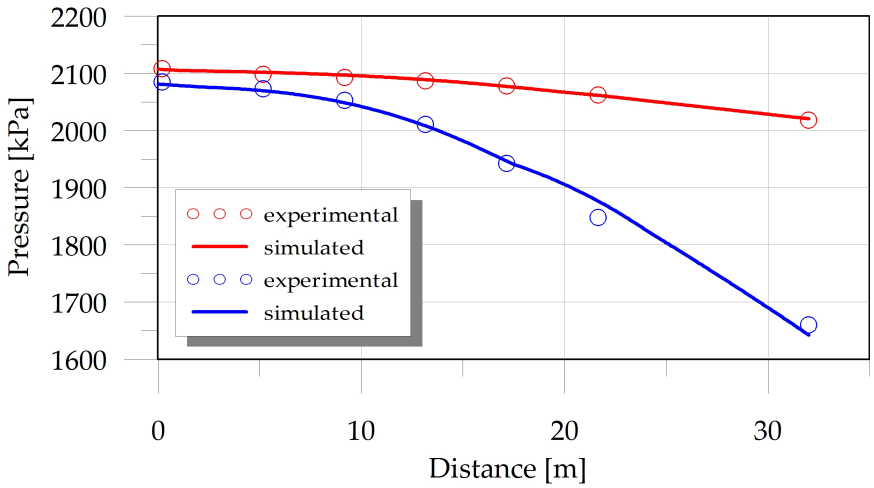

(a) $p_{in} = 20\,\text{bar}$

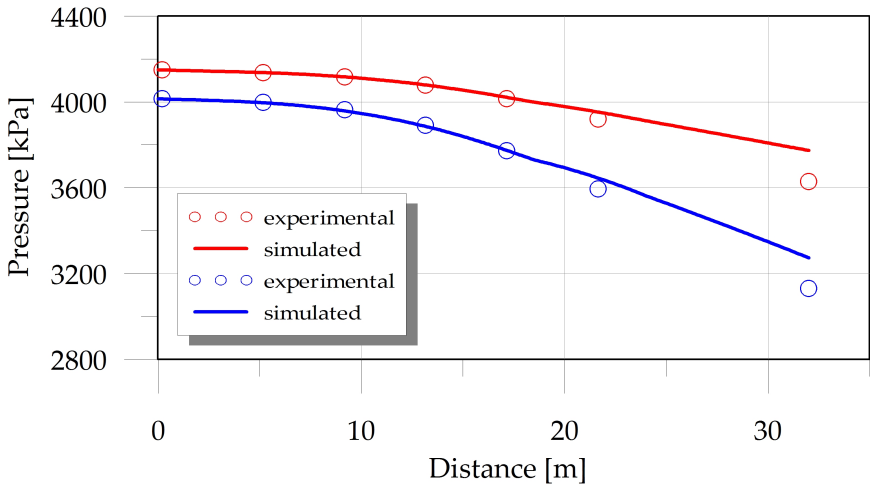

(b) $p_{in} = 40\,\text{bar}$

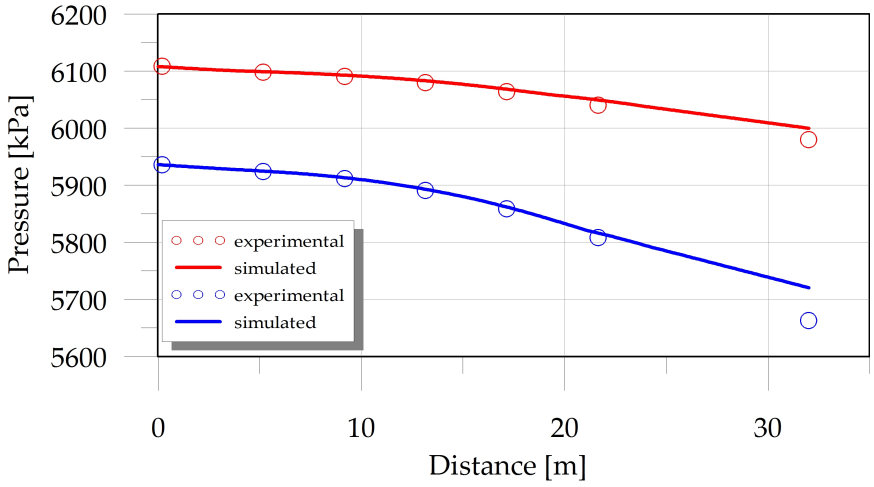

(c) $p_{in} = 60\,\text{bar}$

Figure 2.7: Comparison between simulated pressure spatial shape and experimental data.

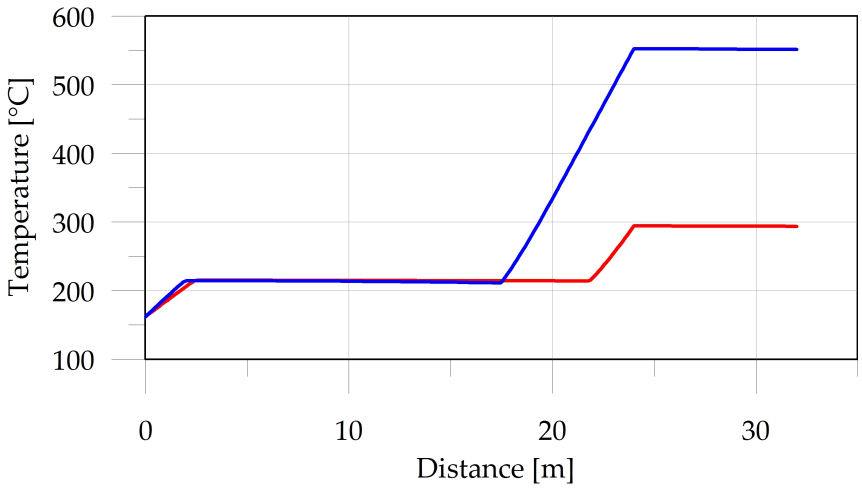

(a) $p_{in} = 20\,\text{bar}$

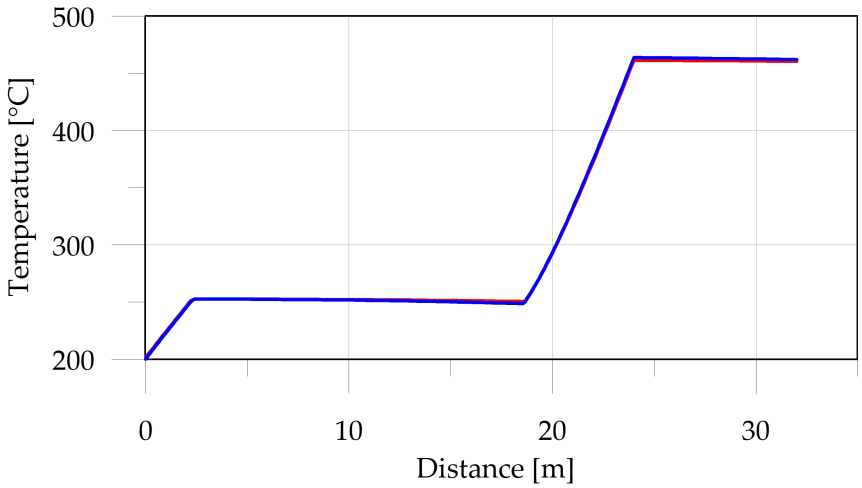

(b) $p_{in} = 40\,\text{bar}$

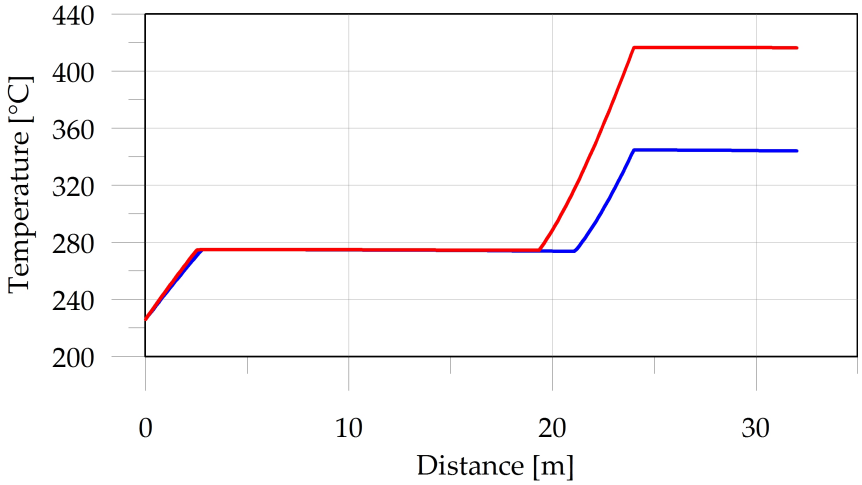

(c) $p_{in} = 60\,\text{bar}$

Figure 2.8: Simulated temperature spatial distributions.

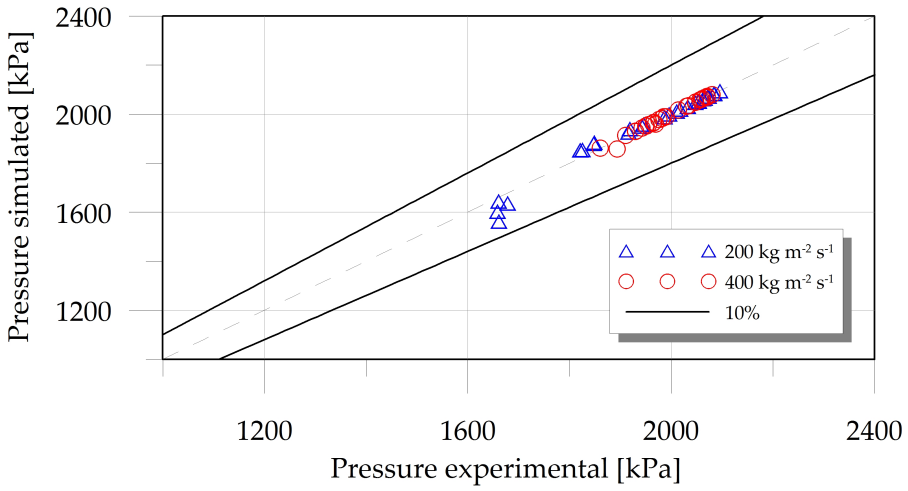

(a) $p_{in} = 20\,\text{bar}$

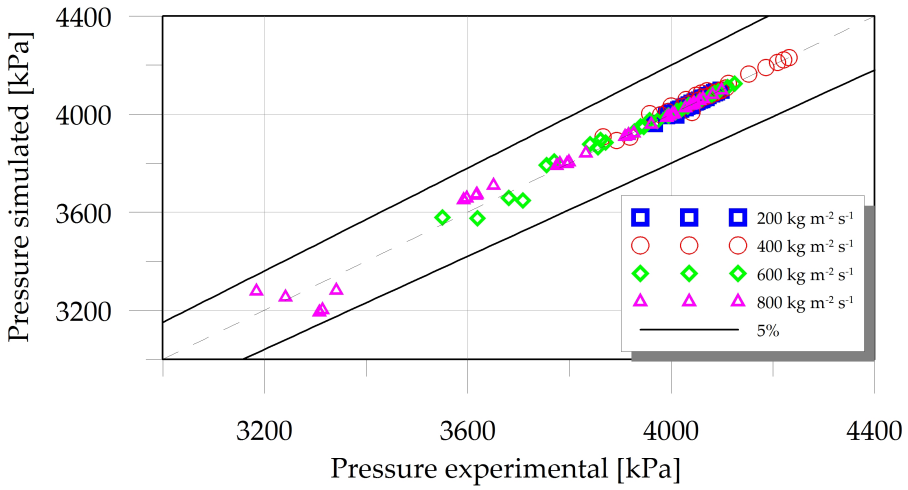

(b) $p_{in} = 40\,\text{bar}$

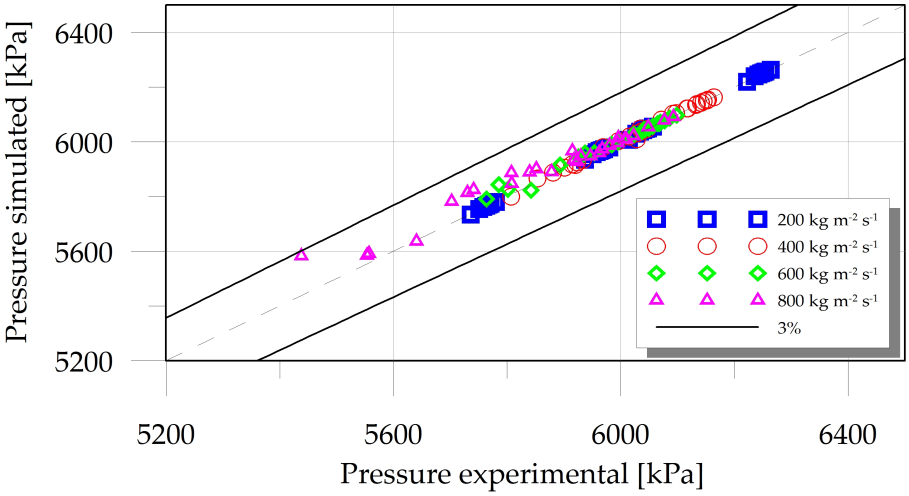

(c) $p_{in} = 60\,\text{bar}$

Figure 2.9: Comparison between simulated and experimental pressure data.

Moreover, the computer implementation of the mathematical model by using *COMSOL Multiphysics* has shown good numerical stability. The compiler revealed to be quite strong in almost all cases and its adoption of *COMSOL Multiphysics* permitted, as said, to get good results, easily and quickly.

Finally, the validation process pointed out a satisfactory reproducibility of the experimental data analyzed, with a maximum error of 10 %.

Bibliography

[1] Neil E. Todreas and Mujid S. Kazimi. *NUCLEAR SYSTEMS I - Thermal Hydraulic Fundamentals*. Taylor&Francis, 1989.

[2] Takashi Hibiki and Mamoru Ishii. One-dimensional drift-flux model and constitutive equations for relative motion between phases in various two-phase flow regimes. *International Journal of Heat and Mass transfer*, 2003.

[3] Gianfranco Caruso. *Esercitazioni di Impianti Nucleari*. Aracne, 2003.

[4] *COMSOL Multiphysics 3.5a User's Guide*.

[5] *COMSOL Multiphysics 3.5a Modeling Guide*.

[6] Private communication.

Chapter 3

Single channel analysis

Abstract

A two-phase single channel system has been analyzed by means of a fluid dynamic model, developed in chapter 2, being conveniently adjusted.

After a detailed explanation of the main modifications made, the performed analysis is illustrated. It is made by three different parts.

The first one illustrates a complete steady state analysis in which steady state simulation results and some system characteristic curves are obtained in function of different slip models and by varying the operating parameters set.

The second one illustrates the linear stability analysis performed on the system and the stability maps drawn, which have been compared to results available from literature. The analysis has been performed, also in this case, using different slip models.

The last one illustrates the results of two types of transient simulations: a stable and an unstable one; both these simulations represent the system response to an input step of thermal power.

3.1 Introduction

In this chapter the analysis of the behavior of a two-phase single channel has been performed and, to do that, the model developed in chapter 2 has been used.

First of all, this model has been modified to comply with the aim referred above: a thermal model of the wall and a fluid dynamic model for local pressure losses have been added; moreover, convenient boundary conditions have been fixed in order to take into account the presence of an upper and a lower plenum.

Then, the model has been used to perform a steady state analysis consisted in two parts: the steady analysis of a test case and the computation of the characteristic curves of the system. The test case is characterized by a set of operating conditions inspired to those ones typical of a BWR subchannel and these steady calculations have been done in order to compare the results given by different slip ratio and two-phase friction models. The system characteristic curves obtained are instead the classical pressure drop versus mass flow rate and the flow rate versus thermal flux curves at constant pressure drop across the channel. These curves have been computed by varying different operating parameters to compare their effect on the system static behavior.

After that, by using both the model and some of the results obtained with the steady analysis (that are the equilibrium operating points) a linear stability analysis has been performed and stability maps have been drawn.

Finally, some transient calculations on the system have been simulated both in stable and unstable conditions, determined by means of the linear stability analysis results. The system transient behavior has been studied as a response to an input step of thermal power.

All the analyses have been carried out by means of *COMSOL Multiphysics* code, using both the Homogeneous Equilibrium Model and the Drift Flux Model. The only exception are the transient calculations in the unstable conditions, in which only the HEM has been used.

3.2 The system and the model

In this section the main features of the physical system and of the model used to analyze it are illustrated.

The description is divided in three parts.

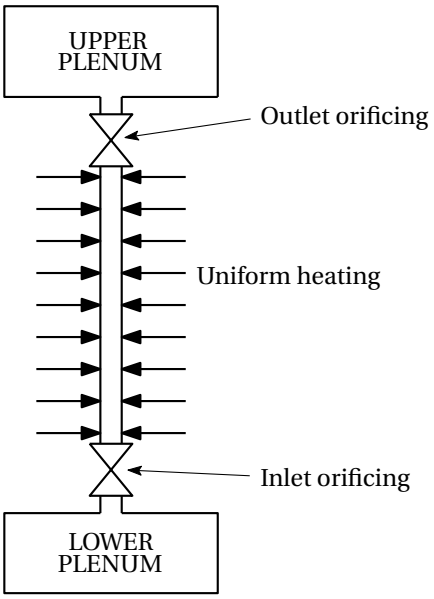

Figure 3.1: Sketch of the boiling channel model.

The first one describes the main physical features of the system, like geometry, thermal properties, operating conditions and so on.

The second one summarizes the mathematical model adopted for the calculations, in particular, being the model already exhaustively explained in chapter 2, only the main modifications are reported.

The last part describes the implementation of those modifications by means of *COMSOL Multiphysics* code.

3.2.1 The physical system

The considered system is a single vertical pipe having circular cross section and subject to uniform heating along its axis. The geometrical features of the channel have been assumed to be:

- the diameter D, equal to 0.0124 m;
- the length L, equal to 3.6576 m (i.e. 12 ft);
- a slope angle θ, equal to 90°;

With reference to Figure 3.1 two inlet and outlet plena can be used to keep imposed pressures, in order to let the flow rate to freely evolve. Alternatively, the system

can be flow forced by imposing the inlet flow rate instead of the outlet pressure. Inlet pressure and enthalpy are always imposed.

The inlet plenum pressure p_{in} determines the pressure level of the system which has been fixed and kept constant to the value of 7.0 MPa.

Local pressure losses at the inlet and the outlet of the channel are accounted for.

The physical size of the channel and the operating pressure, adopted for the calculations, are the same adopted in [1], inspired to classical values characterizing a BWR subchannel.

Moreover, the heater dynamics is taken into account by introducing the thermal inertia of the heated wall. The heating wall has been assumed to be homogeneous and isotropic, made of steel with a thickness t_w of 1 mm; its principal physical characteristics, that is, density ρ_w and specific heat capacity c_w have been assumed to be constant and uniform and they have been fixed as follows:

$$\begin{cases} \rho_w = 8000\,\mathrm{kg\,m^{-3}} \\ c_w = 475\,\mathrm{J\,kg^{-1}\,K^{-1}} \end{cases}$$

Heat exchange process between wall and fluid has been described by a uniform heat transfer coefficient. This choice is very strong, nevertheless the main interest is only to assess the effect of the wall thermal inertia on the system dynamics. The heat transfer coefficient U_{ex} between wall and fluid has been assumed to be equal to $10\,\mathrm{kW\,m^{-2}\,K^{-1}}$ which is also a relatively low value but that allowed to have a time constant not too small to be appreciated. External heat losses have been neglected.

Table 3.1 summarizes the main system operating parameters listed above.

3.2.2 The mathematical model

The mathematical model built up, used to simulate the system, consists of two coupled distinct models. The first one is a model for the fluid dynamics while the second one is a simplified model for the thermal behavior of the channel wall.

Later on these models are illustrated.

Fluid	Water
System pressure	7.0 MPa
Channel type	Cylindrical
Channel diameter	12.4 mm
Slope angle	90°
Flow area	120.8 mm^2
Heated perimeter	38.9 mm
Channel length	3.6576 m
Wall material	Steel
Wall thickness	1 mm
Wall density	8000 $kg\,m^{-3}$
Wall thermal heat capacity	475 $J\,kg^{-1}\,K^{-1}$
Wall-fluid heat transfer coefficient	10 $kW\,m^{-2}\,K^{-1}$

Table 3.1: Main geometry and operating conditions.

Fluid dynamics

The mathematical model structure used for the two-phase fluid dynamics is the same described and used in chapter 2. Thus the fluid dynamic features have been described on the basis of the mixture equations (2.5), (2.6) and (2.8) and of the constitutive laws and the closure equations shown in the sections 2.2.4 and 2.2.5.

Nevertheless, the model has been modified in order to apply with the physical system sketched in Figure 3.1. The main changes concern the inlet and outlet local pressure drops and the correlation adopted for the slip model and for the two-phase friction multiplier.

Local pressure drops are due to sharp variations in the duct cross section or, more in general, to the presence of geometrical discontinuities along the pipe (e.g. valves, curves, etc...), and they are usually modeled by means of a constant K (or K'), as follows:

$$\Delta p_{\text{conc}} = K \frac{\rho V^2}{2} = K \phi_{lo}^2 \frac{G^2}{2\rho} \tag{3.1}$$

otherwise:

$$\Delta p_{\text{conc}} = K' \rho V^2 = K' \phi_{lo}^2 \frac{G^2}{\rho} \tag{3.2}$$

from which:

$$K = 2K'$$

In the present work, definition (3.1) has been used.

In equations (3.1) and (3.2) ρ and V respectively represent the generic fluid density[1] and mean velocity.

An opportune term representing the local losses is required in the momentum (and energy) balance equation. In fact, while equation (3.1) represents an integral pressure drop, that is, if the pressure drop is localized around the point of coordinate z^*:

$$\Delta p_{conc} = \int_{z^*-\varepsilon}^{z^*+\varepsilon} \left(\frac{\partial p}{\partial z}\right)_{conc} dz$$

where 2ε obviously is the length of the segment which contains the entire geometrical discontinuity (e.g. valve length), the model is one-dimensional, that is a distributed parameter model. Thus, the local pressure drops has to be introduced as a pressure variation per unit of length, i.e. as a derivative, to be taken into account of it in the balance equations. This task can be achieved by means of the following relation:

$$\left(\frac{\partial p}{\partial z}\right)_{conc} = K \phi_{lo}^2 \frac{G^2}{2\rho} \delta\left(z - z^*\right) \tag{3.3}$$

where $\delta(z - z^*)$ is the Dirac-delta function. Therefore equation (2.6) takes the form:

$$\begin{aligned} \frac{\partial G}{\partial t} + \frac{\partial}{\partial z}\left(\frac{G^2}{\rho_m^+}\right) = &- \frac{\partial p}{\partial z} - \rho_m g \sin\theta - \phi_{lo}^2 f \frac{G^2}{2\rho D} + \\ &- K_{in} \phi_{lo}^2 \frac{G^2}{2\rho} \delta(z) - K_{out} \phi_{lo}^2 \frac{G^2}{2\rho} \delta(z - L) \end{aligned} \tag{3.4}$$

In equation (3.4) the friction term f is here used to indicate both the single-phase friction factor and the liquid-only friction factor f_{lo} used in the two-phase friction model.

It is also to be noticed that the introduction of these new terms into equation (3.4) allows to generalize the model and to take into account the presence of other segments of the system, before or after the channel, like for example an up riser.

[1] In the case of two-phase mixture, the fluid density ρ must be substituted with the appropriate quantity, that is ρ_L.

As concerns the two-phase friction and the slip ratio, different models have been used. With regards to the slip ratio, both the HEM and the Drift Flux Model have been tested.

Together with the homogeneous model an HEM two-phase flow friction model has been adopted. This model uses the following correlation [2]:

$$\phi_{lo}^2 = 1 + x\left(\frac{\rho_L}{\rho_V} - 1\right) \tag{3.5}$$

The drift flux model has instead been used by assuming a concentration parameter:

$$C_0 = 1.13 \tag{3.6}$$

as reported in [3], and the relation (2.28); for the effective drift velocity the following correlation of Lahey and Moody [2] has been used:

$$V_{vj} = 2.9\left[\frac{\sigma\, g\,(\rho_L - \rho_V)}{\rho_L^2}\right]^{0.25} \tag{3.7}$$

In some cases, that will be specified later on, V_{vj} has been neglected.

Wall model

The model adopted to describe the wall is based on a simple energy balance equation, that is:

$$\frac{\partial E_w}{\partial t} = \dot{Q}_{in} - \dot{Q}_{out} \tag{3.8}$$

Assuming the wall made by steel, homogeneous and isotropic, and neglecting the heat losses outside the channel:

$$M_w\, c_w \frac{\partial T_w}{\partial t} = q''\, P\, L - U_{ex}\, P\, L\, (T_w - T_b) \tag{3.9}$$

then:

$$\frac{\partial T_w}{\partial t} = q'' \frac{P\, L}{M_w\, c_w} - \frac{(T_w - T_b)}{\tau_w} \tag{3.10}$$

where τ_w is the time constant of the wall, given by:

$$\tau_w = \frac{M_w\, c_w}{U_{ex}\, P\, L} \simeq 0.2\,\mathrm{s} \tag{3.11}$$

The first right-hand side term of the balance equation (3.9) represents the thermal power generated inside the wall (e.g. electrically), the second one represents instead the thermal power transfered to the fluid.

The energy balance equation for the mixture (2.8) becomes then the following one:

$$\begin{aligned}\frac{\partial}{\partial t}\left(\rho_m h_m - p\right) + \frac{\partial}{\partial z}\left(G h_m^+\right) = \frac{U_{ex} P \left(T_w - T_b\right)}{A} + \frac{G}{\rho_m}\left[\phi_{lo}^2 f \frac{G^2}{2\rho D} + \right. \\ \left. + K_{in}\phi_{lo}^2 \frac{G^2}{2\rho}\delta(z) + K_{out}\phi_{lo}^2 \frac{G^2}{2\rho}\delta(z-L) + \frac{\partial p}{\partial z}\right]\end{aligned} \tag{3.12}$$

In equation (3.12) the first right-hand side term represents the thermal coupling between the wall and the fluid.

3.2.3 Model implementation

The implementation of the mathematical model described above has been done, also in this case, by means of *COMSOL Multiphysics* code. The differential equations (2.5), (3.4), (3.12) and (3.9) have been set up by means of the *PDE General Form* module already described in chapter 2. The same considerations are valid for the constitutive laws and the closure equations illustrated in sections 2.2.4 and 2.2.5, respectively.

The main innovation with respect to chapter 2 is the introduction of the wall model and of the function $\delta(z - z^*)$.

The implementation of equation (3.9) has been done in the same way already explained in chapter 2 for what concerns the balance equations. The wall equation has been instead implemented in this way[2]:

$$\begin{aligned} d_a \frac{\partial T_w}{\partial t} + \nabla \cdot 0 &= q'' - U_{ex}\left(T_w - T_b\right) \\ \text{Neumann b.c.:} \qquad \Gamma(0) &= 0 \qquad \Gamma(L) = 0 \end{aligned} \tag{3.13}$$

where the mass coefficient d_a is:

$$d_a = \frac{M_w c_w}{P L}$$

[2] cf. equation (2.40).

With regards to the Dirac delta function $\delta(z-z^*)$, COMSOL code is capable to simulate it as derivative of the Heaviside step function. This function can be built up with the commands:

```
flsmhs(x-x0,sc)
flc1hs(x-x0,sc)
flc2hs(x-x0,sc)
```

These commands allow to introduce the discontinuous Heaviside smoothed step function by means of 7th degree polynomial interpolation. The function is centered around the point $x0$ and has an amplitude specified by *sc* parameter. More detailed information can be found in [4].

The Dirac-delta function can instead be implemented with the commands:

```
fldsmhs(x-x0,sc)
fldc1hs(x-x0,sc)
fldc2hs(x-x0,sc)
```

The parameter *sc* has been kept constant and equal to 0.01 in all the performed simulations. This value corresponds to a length of the discontinuity segment of 1 cm.

3.3 Steady state analysis

In this section the results of steady state simulations are reported.

At first, some simulations in a test case have been run using two different drift flux model and the homogeneous equilibrium model in order to compare the obtained results.

Secondly, by using a drift flux model and the homogeneous equilibrium model, some steady characteristic curves of the channel have been computed. These curves have been obtained as function of different parameters, among which the inlet subcooling ΔT_{sub} (or the inlet enthalpy h_{in}), the thermal power q (or the thermal flux q''), the coefficients K_{in} and K_{out}. Such characteristic curves are the following ones:

- Δp vs G, with h_{in}, q'', K_{in}, K_{out} as parameters;
- G vs q'', with h_{in}, Δp, K_{in}, K_{out} as parameters.

3.3.1 Steady state simulations

Steady state simulations have been run using two different drift flux models and the homogeneous equilibrium model (HEM).

The main task of such study is to compare the results given by these models. To do that some operating conditions which are representative of a BWR subchannel have been fixed. Such conditions are the following:

- $p_{in} = 7.0\,\mathrm{MPa}$;
- $T_{in} = 274\,^{\circ}\mathrm{C}$, i.e. $h_{in} = 1205\,\mathrm{kJ\,kg^{-1}}$;
- $q = 71.24\,\mathrm{kW}$, i.e. $q'' = 500\,\mathrm{kW\,m^{-2}}$;
- $K_{in} = 25$ and $K_{in} = 5$;
- $G_{in} = 2000\,\mathrm{kg\,m^{-2}\,s^{-1}}$, that is $w_{in} = 0.242\,\mathrm{kg\,s^{-1}}$ (i.e. $V_{in} = 2.7\,\mathrm{m\,s^{-1}}$).

The equation system solved is:

$$\begin{cases} \dfrac{dG}{dz} = 0 \\ \dfrac{d}{dz}\left(\dfrac{G^2}{\rho_m^+}\right) = -\dfrac{dp}{dz} - \rho_m\, g\, \sin\theta - \phi_{lo}^2\, f\, \dfrac{G^2}{2\,\rho\, D} - \sum_{j=in}^{out} K_j\, \phi_{lo}^2\, \dfrac{G^2}{2\,\rho}\, \delta\left(z - z_j\right) \\ \dfrac{d}{dz}\left(G\, h_m^+\right) = \dfrac{U_{ex}\, P\, (T_w - T_b)}{A} + \dfrac{G}{\rho_m}\left[\phi_{lo}^2\, f\, \dfrac{G^2}{2\,\rho\, D} + \sum_{j=in}^{out} K_j\, \phi_{lo}^2\, \dfrac{G^2}{2\,\rho}\, \delta\left(z - z_j\right) + \dfrac{dp}{dz}\right] \\ 0 = q'' - U_{ex}\, (T_w - T_b) \\ + \text{boundary conditions} \\ + \text{constitutive laws and closure equations} \end{cases} \tag{3.14}$$

The two drift flux models adopted are differs each other because of the different specification of the concentration parameter C_0. The first one used, model A from now on, fixes the value of C_0 according to (3.6). The second one, model B from now on, uses instead the Dix correlation (2.28) for the parameter. Both models have been used adopting the general correlation of Lahey and Moody (3.7) for the effective drift velocity V_{vj} and the Jones correlation (2.38) for the two-phase friction multiplier evaluation.

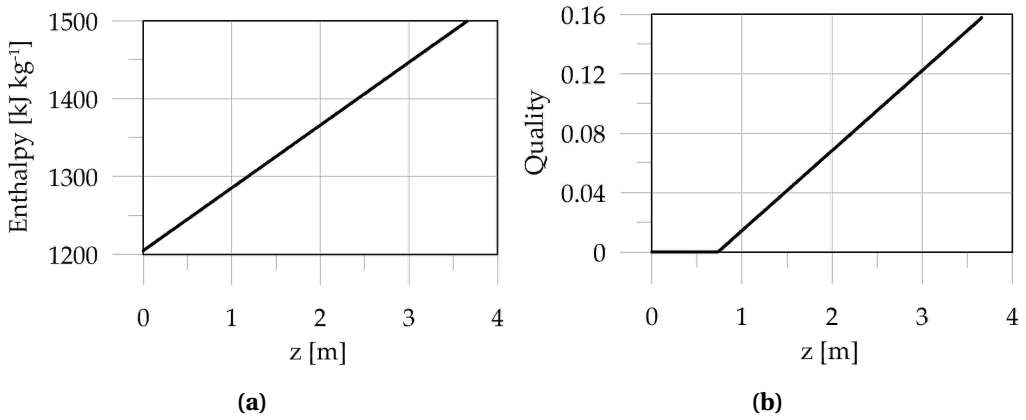

Figure 3.2: Simulated enthalpy and quality distributions.

Homogeneous model has been instead implemented by fixing:

$$\begin{cases} C_0 = 1.0 \\ V_{vj} = 0.0 \end{cases}$$

and by using equation (3.5) to compute the two-phase friction multiplier.

In order to run these simulations, COMSOL steady state solver has been used and it has been set up with a direct linear system solver (PARDISO [5]). In all the simulations run, a meshgrid composed by 1921 points has been used, for a number of degrees of freedom of 15364. About the finite element type, the default one has been adopted: the quadratic Lagrange finite element.

The boundary conditions set used is the one that provides the inlet flow rate w_{in} (mass flux G_{in}), that is, the flow forced method. The constitutive laws and the closure equations are the one reported respectively in section 2.2.4 and 2.2.5.

The main numerical results are reported.

At first, the fluid enthalpy h_m^+, the dynamic quality x_d, the wall and the fluid temperatures T_w and T_b are plotted versus the channel axial coordinate z. The spatial distribution of these quantities are independent from the adopted model: indeed, they only depend on the thermal power input, that is constant. Although the same consideration is not valid for the temperatures, practically their spatial distribution does not vary: the pressure variation along the channel is not different enough between the three models to affect the temperatures spatial shapes significantly.

Figures 3.2a and 3.2b show the spatial distributions respectively of the fluid en-

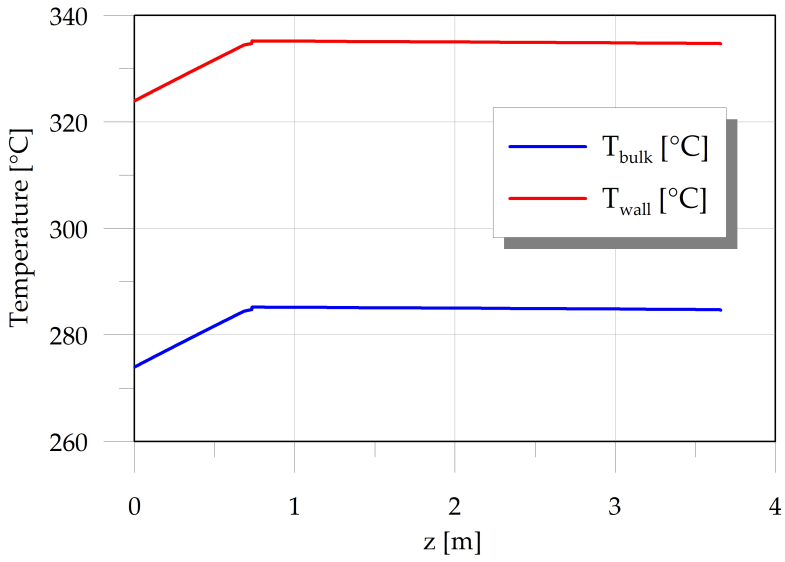

Figure 3.3: Wall and fluid bulk temperature axial distribution.

thalpy and of the mixture quality. The linear trend of the first one is due to the fact that the thermal flux q'' is uniform along the axis.

Figure 3.3 shows the wall and the fluid temperature distributions: it is evident that the difference between the wall and the bulk temperatures is constant and about equal to 50 °C. That is because the heat transfer coefficient U_{ex} is constant. In fact:

$$T_w - T_b = \frac{q''}{U_{ex}} = 50\,^{\circ}\mathrm{C}$$

It can be also noticed that along the two-phase zone of the channel the temperatures slightly decrease due to pressure drops. The pressure distribution in the channel is not sensibly affected by the adopted model.

Figure 3.4 shows the fluid pressure plotted versus the axial coordinate z. It can be noticed the effect of the inlet and the outlet local pressure losses and the slightly higher drop in the case of the drift flux models. The reason of that is ascribed to the higher two-phase friction multiplier calculated in the latter two cases compared with the HEM case: there are no substantial differences between the pressure distribution computed with the drift model A and with the drift model B.

Unlike the pressure profile, the slip ratio S differs very much from model to model. This fact is clearly shown in Figure 3.5a. The effect of this difference in terms of velocity of the liquid and vapor phases is shown instead in Figure 3.5b . As can be seen in that Figure, a decrease of the liquid phase velocity corresponds to an increase of the

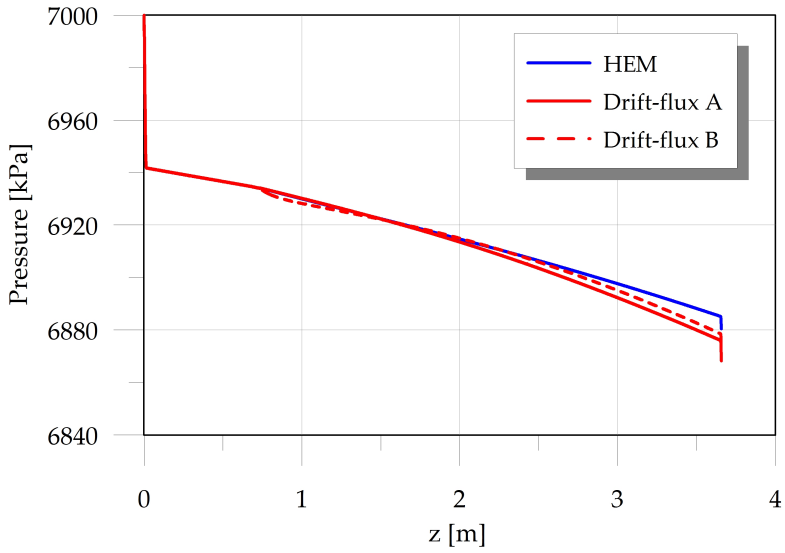

Figure 3.4: Fluid pressure axial distribution.

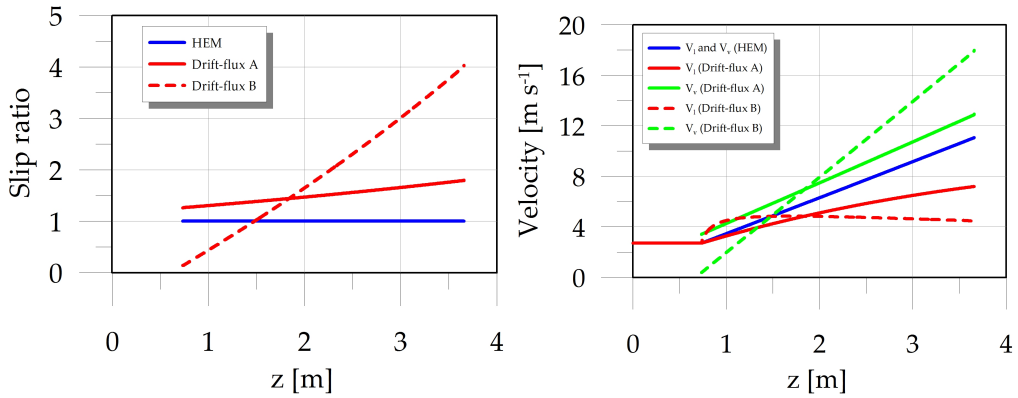

(a) Slip ratio.

(b) Liquid and vapor velocity profile.

Figure 3.5: Slip ratio and phase velocities axial distributions.

vapor phase velocity. This effect is a direct consequence of the momentum conservation.

The mixture density profile reflects the phenomena described above. Figure 3.6a shows that HEM provides a value for the density that is lower compared with the ones provided from the two drift flux models. The reason of that fact is the following: the HEM, because of the assumption of equal phase velocities, forces the void fraction to be higher than the one computed with the drift flux models, in which the vapor volume results faster than the liquid one. The void fraction distribution is shown in Figure 3.6b.

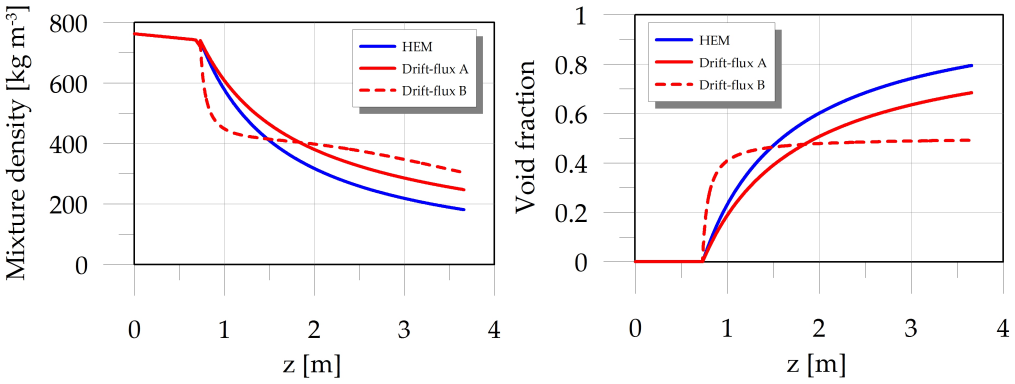

(a) Mixture density. **(b)** Void fraction.

Figure 3.6: Mixture density and void fraction axial distribution.

As final results of this first part of the steady state analysis, the different contributions to the total pressure drop are reported.

The pressure drops can be divided in two main different types: the concentrated (local) pressure drops and the distributed pressure drops.

The concentrated pressure drops are the ones due to the local losses. For the considered system they are given by:

$$\Delta p_{c1} = \int_0^L \phi_{lo}^2 K_{in} \frac{G^2}{2\rho} \delta(z)\, dz \tag{3.15}$$

and

$$\Delta p_{c2} = \int_0^L \phi_{lo}^2 K_{out} \frac{G^2}{2\rho} \delta(z-L)\, dz \tag{3.16}$$

The distributed pressure drops can be divided into the sum of three different contributions: frictional, gravitational and accelerative.

The frictional contribution is the following one:

$$\Delta p_{\text{fric}} = \int_0^L \phi_{lo}^2 f \frac{G^2}{2\rho D} dz \tag{3.17}$$

and it can be separated in the sum of the single-phase and of the two-phase contributions:

$$\Delta p_{\text{fric}} = \int_0^{z_{bb}} f \frac{G^2}{2\rho D} dz + \int_{z_{bb}}^L \phi_{lo}^2 f_{lo} \frac{G^2}{2\rho_L D} dz = \Delta p_{f1} + \Delta p_{f2} \tag{3.18}$$

In a similar way, the gravitational contribution is given by:

$$\begin{aligned} \Delta p_{\text{grav}} &= \int_0^L \rho_m g \sin\theta\, dz = \int_0^{z_{bb}} \rho g \sin\theta\, dz + \int_{z_{bb}}^L \rho_m g \sin\theta\, dz = \\ &= \Delta p_{g1} + \Delta p_{g2} \end{aligned} \tag{3.19}$$

	HEM		Drift A		Drift B	
Contribution	[kPa]	% of total	[kPa]	% of total	[kPa]	% of total
Δp_{f1}	2.20	1.84%	2.20	1.67%	2.20	1.70%
Δp_{f2}	22.63	18.94%	36.04	27.36%	36.02	27.88%
Δp_{g1}	5.39	4.51%	5.39	4.10%	5.39	4.18%
Δp_{g2}	9.70	8.12%	11.47	8.71%	11.95	9.25%
Δp_{a1}	0.31	0.26%	0.31	0.23%	0.31	0.24%
Δp_{a2}	16.75	14.02%	10.81	8.20%	7.80	6.04%
Δp_{c1}	58.13	48.65%	58.13	44.13%	58.13	45.01%
Δp_{c2}	4.58	3.83%	7.60	5.77%	7.59	5.88%

Table 3.2: Various contributions to the total channel pressure drop.

Finally the accelerative pressure drops are give by the relation:

$$\begin{aligned}\Delta p_{\text{acc}} &= \left.\frac{G^2}{\rho_m^+}\right|_L - \left.\frac{G^2}{\rho}\right|_0 = \left[\left.\frac{G^2}{\rho_m^+}\right|_{z_{bb}} - \left.\frac{G^2}{\rho_m^+}\right|_0\right] + \left[\left.\frac{G^2}{\rho}\right|_L - \left.\frac{G^2}{\rho}\right|_{z_{bb}}\right] = \\ &= \Delta p_{a1} + \Delta p_{a2}\end{aligned} \tag{3.20}$$

The contribution listed above can be also identified by integrating over the domain the steady state momentum equation of the system (3.14) in order to obtain:

$$\begin{aligned}&\Delta p + \Delta p_{\text{fric}} + \Delta p_{\text{grav}} + \Delta p_{\text{acc}} + \Delta p_{\text{conc}} = \Delta p + \left[\Delta p_{f1} + \Delta p_{f2}\right] + \\ &+ \left[\Delta p_{g1} + \Delta p_{g2}\right] + \left[\Delta p_{a1} + \Delta p_{a2}\right] + \left[\Delta p_{c1} + \Delta p_{c2}\right] = 0\end{aligned} \tag{3.21}$$

The results of these calculations are summarized in Table 3.2.

As the table shows, the main contribution to channel pressure drop is the inlet local loss which consists in quite a half of the total, and its absolute value is the same in the three cases. The reason of that is: the inlet conditions are the same and, moreover, the fluid is still a single-phase mixture. This fact is true for every single-phase contribution because they are independent from the adopted fluid model. Obviously the relative weights are different from case to case.

With regards to the two-phase contributions, it can be noticed that the gravitational terms calculated with the drift flux models are slightly higher than the one cal-

culated with the HEM. The reason is related to the higher void fraction (thus lower mixture density) computed with the latter one (Figure 3.6b).

The main differences can be observed in the outlet local loss, the frictional and the accelerative terms. The latter ones are higher in the HEM case, intermediate in the drift flux A model case and lower in the drift flux B case. The reason is directly connected to the mixture density values which are high for high slip ratios and low for low slip ratios (Figure 3.6a and 3.6b). The outlet local loss and the two-phase frictional pressure drop values are instead strictly related to the two-phase friction multiplier ϕ_{lo}^2, as can be easily deduced from Table 3.2.

In order to conclude this first part of the steady state analysis, some considerations about the results follow.

The simulations run have shown that the response of the model is physically sensitive. In particular, they revealed some main features of the two drift flux models tested. Model A seems to have an *average* behavior compared with model B and it can be considered as an acceptable approximation of the latter one. Its main limit is the fact that, since model A uses a constant average value for the parameter C_0, it is not able to accurately describe the spatial distribution as model B; nevertheless it is a simple model assumption which can take into account the slip ratio variation along the channel axis unlike HEM can do.

3.3.2 Steady state characteristic curves

The steady state characteristic curves are plots whose points represent a single steady state operating condition. The importance of the steady state curves of the system are due to their usefulness to deduce lots of informations about the system, among which some instability concerns (chapter 1).

These curves have been obtained by solving the same equations system (3.14) and by varying the operating condition parameters. Two kind of characteristic curves have been obtained.

The first one is the classical Δp vs G curve, useful to understand if static instabilities, i.e. flow excursions (Ledinegg), may occur and to deduce important design considerations.

Secondly some G vs q'' curves have been computed and used to perform the linear stability analysis.

Pressure drop versus mass flux

The Δp vs G curves have been obtained by solving the system (3.14) several times in correspondence of different values of inlet mass flow rate G_{in}. This procedure has been repeated for different values of the inlet subcooling ΔT_{sub} (inlet enthalpy h_{in}), thermal power input q_{in} (thermal flux q''), K_{in} and K_{out} (local pressure losses). The calculations have been done by using both the drift flux model A and the HEM.

Unlike the simulations described in section 3.3.1, here the effective drift flux velocity has been neglected. The reason for this choice is in the fact that for high exit qualities, i.e. low mass fluxes, the flow pattern becomes annular and for annular flow V_{vj} is usually neglected [6]. Nevertheless, the main reason is related to the drift flux slip ratio definition (2.27). For high qualities the last term would lead, indeed, to too high slip ratio values ($S \sim 100$), being[3] $V_{vj} \sim 0.2 \div 0.5\,\mathrm{m\,s^{-1}}$.

In order to obtain these curves, COMSOL parametric solver [5] has been used. The parameters set is an inlet mass flux interval: from 500 to $5000\,\mathrm{kg\,m^{-2}\,s^{-1}}$ compound by a total of 35 elements. The other settings, like the meshgrid elements number and the linear system solver, are the same used in the previous section 3.3.1.

Later on, some results are reported and briefly discussed.

Figure 3.7 This figure shows the characteristic curves obtained by fixing an high value both for the inlet subcooling and the thermal power input:

$$\begin{cases} \Delta T_{sub} = 140\,^{\circ}\mathrm{C} & \text{i.e.} \qquad h_{in} = 618.72\,\mathrm{kJ\,kg^{-1}} \\ q'' = 1.4\,\mathrm{MW\,m^{-2}} \end{cases}$$

The effect of the inlet and outlet local pressure losses coefficients is shown: the curves are plotted for three different couples of K_{in} and K_{out}. It can be noticed that the total pressure drop in the two-phase zone of the plot, that is, from about 500 to $2500\,\mathrm{kg\,m^{-2}\,s^{-1}}$, seems to be mostly controlled by the outlet local loss, especially in the drift flux model case (plot 3.7b); indeed the inlet local loss

[3] if computed with the correlations (2.33) and (3.7)

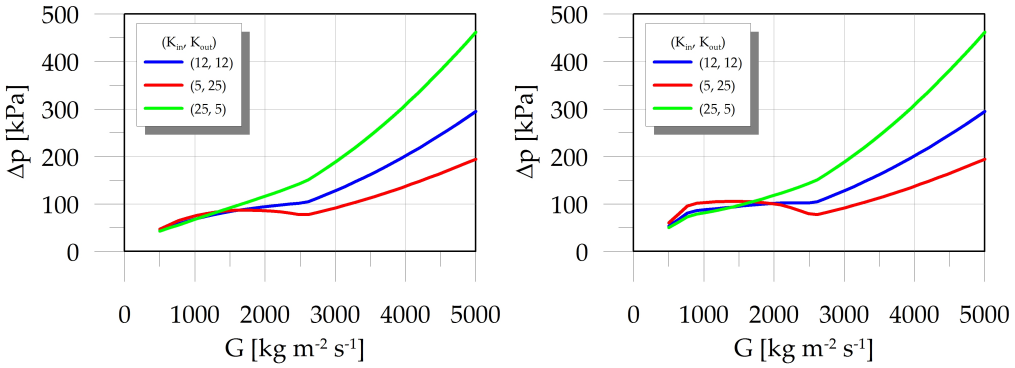

(a) Curves obtained with the HEM. **(b)** Curves obtained with the Drift flux model.

Figure 3.7: Characteristic curves as function of K_{in} and K_{out}. High thermal power and subcooling.

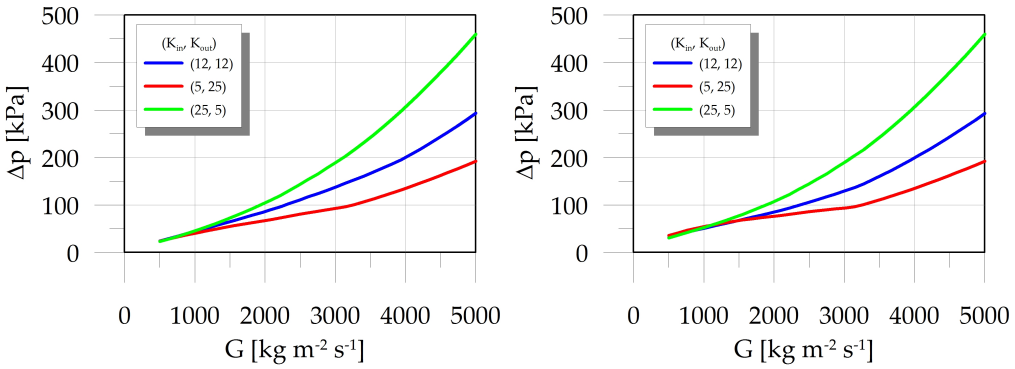

(a) Curves obtained with the HEM. **(b)** Curves obtained with the Drift flux model.

Figure 3.8: Characteristic curves in function of K_{in} and K_{out}. Low thermal power and subcooling.

seems to affect more the total pressure drop in the single-phase zone, i.e. for $G \gtrsim 2500\,\mathrm{kg\,m^{-2}\,s^{-1}}$.

Moreover, as it can be more clearly deduced from plot 3.7b, the negative slope of the curve seems to appear when the outlet local loss becomes greater than the inlet one.

Figure 3.8 This figure shows the same Δp vs G curves computed in Figure 3.7 by using a low value both for the inlet subcooling and the thermal power input. In-

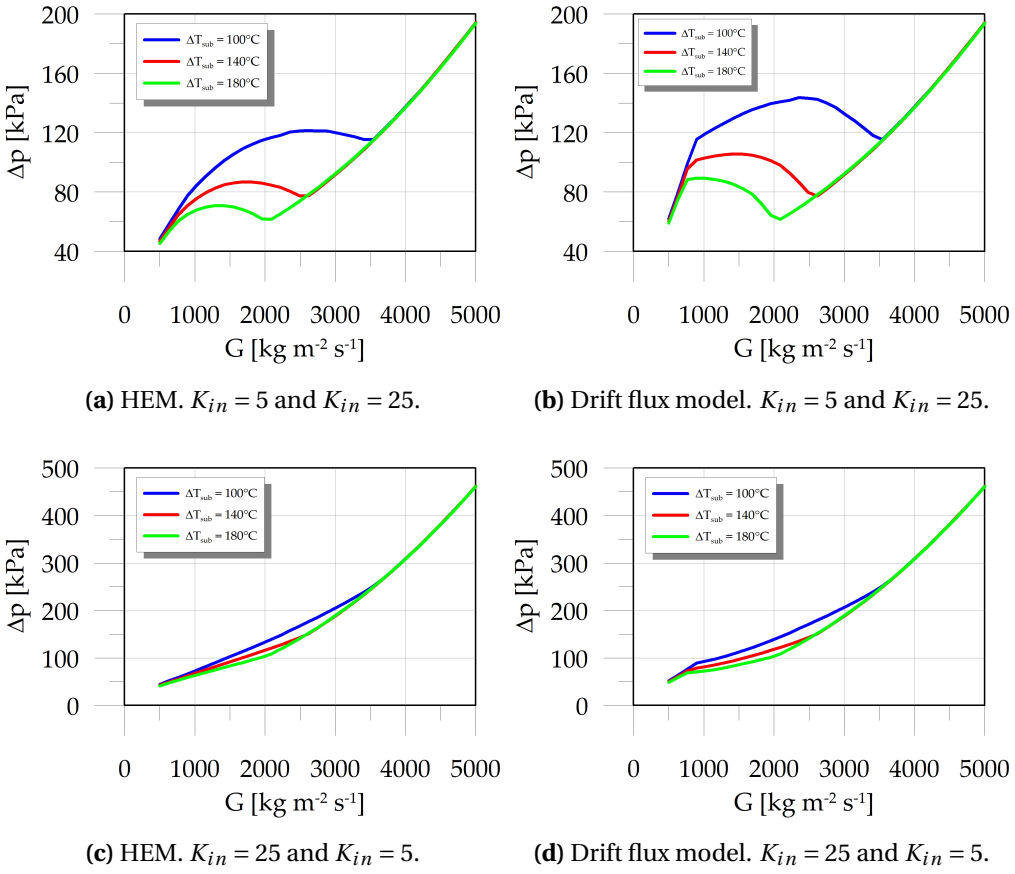

(a) HEM. $K_{in} = 5$ and $K_{in} = 25$.

(b) Drift flux model. $K_{in} = 5$ and $K_{in} = 25$.

(c) HEM. $K_{in} = 25$ and $K_{in} = 5$.

(d) Drift flux model. $K_{in} = 25$ and $K_{in} = 5$.

Figure 3.9: Characteristic curve as function of the inlet subcooling for high thermal power.

deed these parameters have been set as follow:

$$\begin{cases} \Delta T_{sub} = 30\,^{\circ}\mathrm{C} & \text{i.e.} \qquad h_{in} = 1113.98\,\mathrm{kJ\,kg^{-1}} \\ q'' = 0.4\,\mathrm{MW\,m^{-2}} \end{cases}$$

Unlike the curves of Figure 3.7 these ones seem to be more monotonic: the total pressure drop raises monotonically with the inlet local loss. In particular the pressure drop is different between the three cases as the mass flux increases; for low values, it is more and more slightly affected by K_{in} and K_{out} values.

These curves never show a negative slope.

Figure 3.9 This figure shows the effect of the inlet subcooling on the curve shape in the case of high thermal power inputs and inlet subcoolings. Figure 3.9a and 3.9b have been obtained for the local pressure drop coefficients couple:

$$K_{in} = 5 \qquad K_{in} = 25$$

while Figure 3.9c and 3.9d have been obtained for the couple:

$$K_{in} = 25 \qquad K_{in} = 5$$

In all the four cases, the thermal power input has been kept constant by fixing the thermal flux to $1.4\,\mathrm{MW\,m^{-2}}$. The plots clearly show how an outlet local loss coefficient greater than the inlet one does not stabilize the system, while, on the contrary, a considerable inlet local loss eliminates the negative slopes so that the curve becomes monotone making the system stable. This behavior results to be coherent with what is illustrated in chapter 1. Nevertheless, by comparing the plots, it can be noticed that the system can be stabilized at the price of a significantly increase of the total pressure drop.

With regards to the inlet subcooling, it seems that the reduction of inlet subcooling (i.e. the increasing of h_{in}) has the effect of increasing the pressure drop of the two-phase zone and of increasing the mass flux at which single-phase flow occurs (both liquid and vapor). This behavior is supported, almost qualitatively, by the experimental results reported in [3].

Finally the pressure drop evaluated with the drift flux model results slightly higher in the two-phase zone than the one computed by means of the HEM.

Figure 3.10 This curves set has been obtained so as the one in Figure 3.9 but, in this case, the inlet subcooling has been kept constant to the value of 140 °C (i.e. $h_{in} = 618.72\,\mathrm{kJ\,kg^{-1}}$). In these figures is shown indeed the effect of thermal power input variations. Also in these figures it is evident the stabilizing effect of the inlet local loss. The main effect that can be noticed is the increase of the pressure drop in the two-phase zone with the thermal flux and of the mass flux at which the single-phase flow occurs.

Figure 3.11 This figure shows the effects of the thermal flux and of the inlet subcoolings in the usual two local pressure losses conditions of the previous figures but with low subcoolings and thermal flux conditions set. The plot of Figure 3.11a and 3.11c have been obtained with a constant thermal flux of $400\,\mathrm{kW\,m^{-2}}$

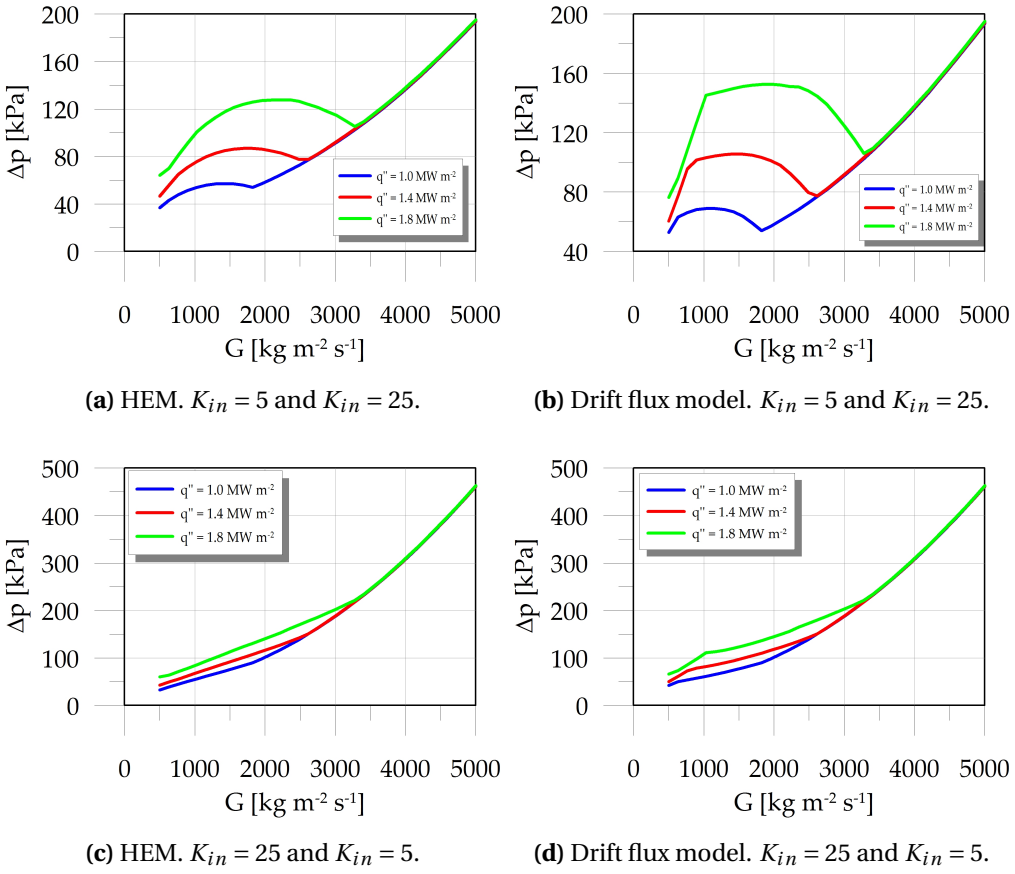

(a) HEM. $K_{in} = 5$ and $K_{in} = 25$.

(b) Drift flux model. $K_{in} = 5$ and $K_{in} = 25$.

(c) HEM. $K_{in} = 25$ and $K_{in} = 5$.

(d) Drift flux model. $K_{in} = 25$ and $K_{in} = 5$.

Figure 3.10: Characteristic curve as function of the thermal power for high inlet subcooling.

for different inlet subcoolings. In this case non negative slope plots can be observed but the behavior is similar to the one found in the previous figures. Also in this case, the pressure drop is higher for the second couple of K_{in} and K_{out}.

Similar considerations are valid for both figure 3.11b and 3.11d in which the inlet subcooling has been kept constant to 30 °C (i.e. $h_{in} = 1113.98\,\mathrm{kJ\,kg^{-1}}$).

All the curves shown in these figures have been computed by means of the HEM: indeed there are no appreciable differences between the results given by the two models.

Figure 3.12 This figure evidences the differences between the Drift flux model and the HEM results in the case of:

$$\begin{cases} \Delta T_{sub} = 140\,^{\circ}\mathrm{C} & \text{i.e.} \qquad h_{in} = 618.72\,\mathrm{kJ\,kg^{-1}} \\ q'' = 1.4\,\mathrm{MW\,m^{-2}} \end{cases}$$

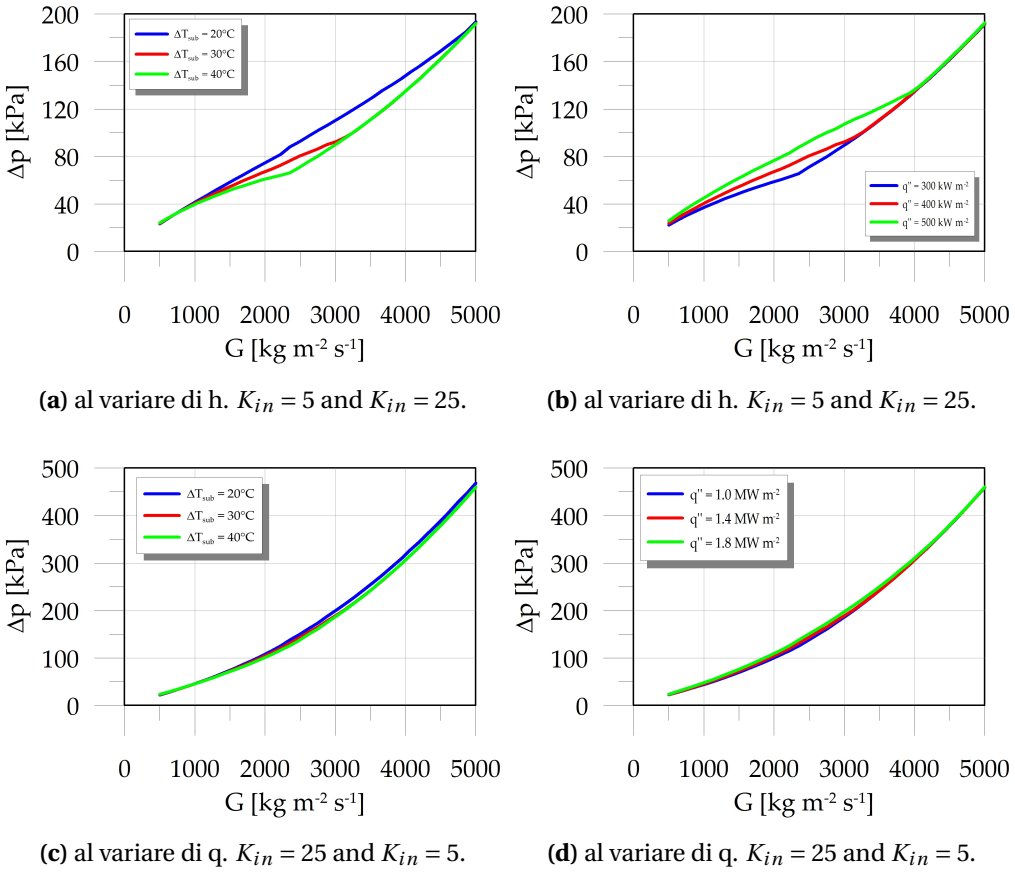

(a) al variare di h. $K_{in} = 5$ and $K_{in} = 25$.

(b) al variare di h. $K_{in} = 5$ and $K_{in} = 25$.

(c) al variare di q. $K_{in} = 25$ and $K_{in} = 5$.

(d) al variare di q. $K_{in} = 25$ and $K_{in} = 5$.

Figure 3.11: Characteristic curve in function of both the thermal power and the inlet subcooling. Low values.

for two different couples of K_{in} and K_{out}. The main difference is obviously in the two-phase flow part of the curves. The pressure drop computed by means of the drift flux model is higher for low mass fluxes, that is at high exit qualities, and becomes more and more similar to the one computed with the HEM as the mass flux increases.

The analysis of these curves have shown the various effects of the parameters on the system characteristic curve.

First of all, the stabilizing effect of an increased inlet local loss has been effectively observed, together with the destabilizing effect of an increased outlet pressure loss.

Secondly, it can be said that the system tends to be more unstable for high inlet subcoolings and high thermal power inputs. For low subcooling and low thermal power levels no S-shaped curves (with negative slope) have been found.

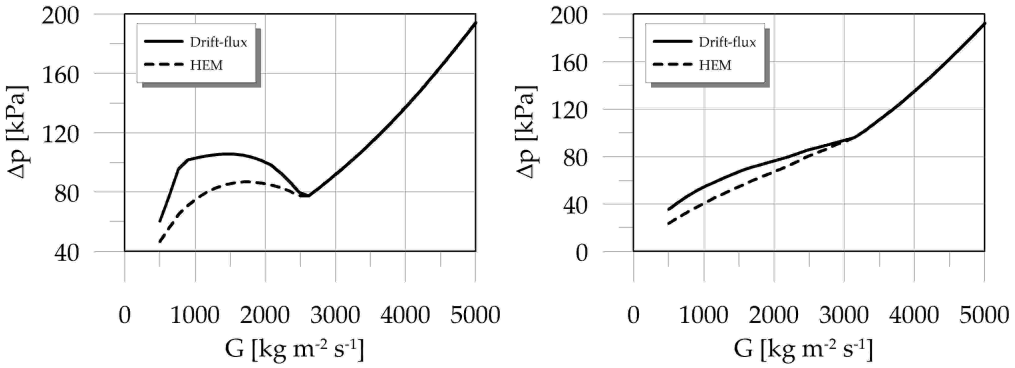

(a) $K_{in} = 5$ and $K_{in} = 25$.

(b) $K_{in} = 25$ and $K_{in} = 5$.

Figure 3.12: Comparison between HEM and Drift flux model at high thermal power and subcooling.

Mass flux versus thermal flux

This kind of curves has been obtained from the Δp vs G characteristic. The main reason for which they have been computed is the linear stability analysis shown in the next section. They provide indeed a set of steady states at constant pressure drop across the channel.

The points of the G vs q'' curves have been obtained again by solving the system (3.14) in order to obtain the Δp vs G characteristic in the same way described above, being from these latter plots the mass flux corresponding to a certain pressure drop extrapolated. The curves have been obtained for three different couples of K_{in} and K_{out} and, for each one, for several different subcooling values. The pressure drop across the channel has been chosen to be 80 kPa and 70 kPa for one of the three couples of K_{in} and K_{out}. The entire procedure has been repeated by using both the HEM and the drift flux model A.

Some of the obtained plots are reported later on and briefly discussed.

The shape of the obtained curves evidences two main different trends. The single-phase zone can be clearly distinguished from the two-phase zone. The single-phase zone is the part on the left of the plot that slightly increases, while the two-phase one is the part that strongly decreases with the thermal flux. The difference between the two trends is due to the density variation with the thermal power input. In the case of single-phase flow, the density variation is very small compared with the two-phase

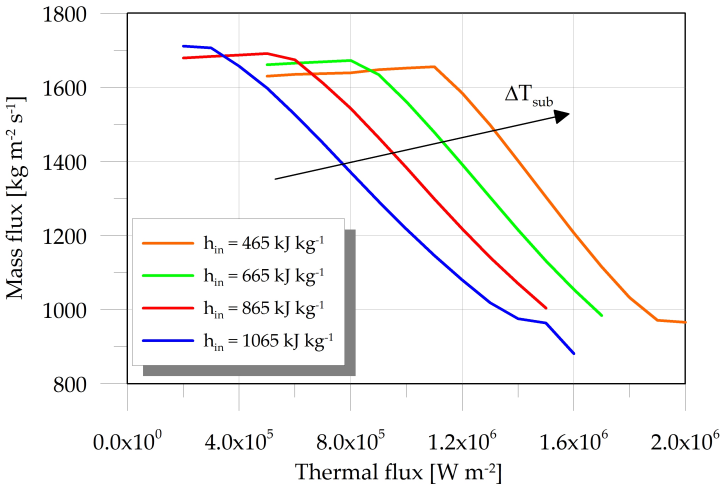

(a) Curves obtained with $K_{in} = 25$ and $K_{out} = 5$ with the HEM.

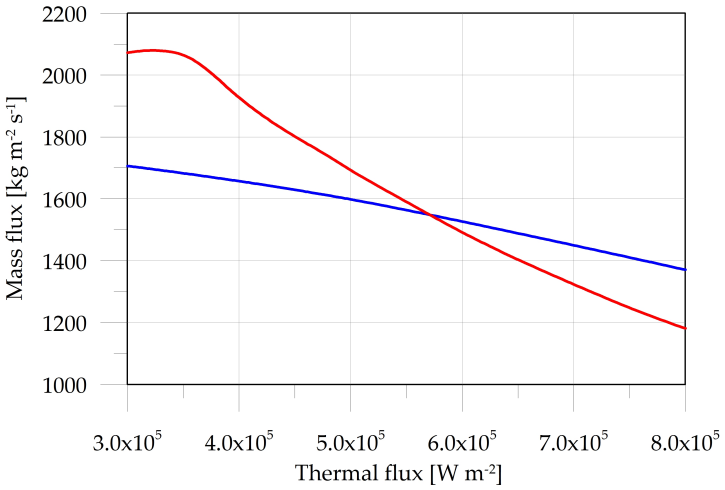

(b) Curves obtained with $K_{in} = 25$ and $K_{out} = 5$ (blue line) and with $K_{in} = 12$ and $K_{out} = 30$ (red line) with the HEM. The inlet enthalpy has been fixed to $1065\,\mathrm{kJ\,kg^{-1}}$.

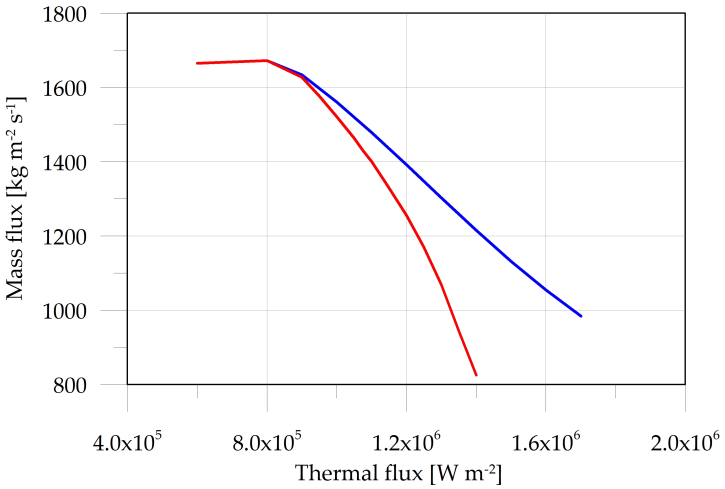

(c) Curves obtained with $K_{in} = 25$ and $K_{out} = 5$ using the HEM (blue line) and the drift flux model (red line). The inlet enthalpy has been fixed to $1065\,\mathrm{kJ\,kg^{-1}}$

Figure 3.13: Curves obtained with a total pressure drop of 80 kPa.

case: the mass flux variation is minimal. In the two-phase part of the plot, instead, the mass flux strongly decreases.

Figure 3.13a shows the effect of the inlet subcooling. Its increase causes the shift of the curve towards the right side of the (q'', G) plane and a small decrease of the two-phase zone slope.

A similar effect can be observed in Figure 3.13b, in which the slope of the two-phase zone of the curve decreases by throttling the channel exit section (increasing K_{out}) more than the inlet one. To decrease the curve slope means to increase the value of q''/G ratio and, consequently, to move the system toward a less stable operating point (chapter 1).

Finally, the differences between a curve computed with the HEM and the drift flux model are shown in Figure 3.13c. As expected, there is a difference only in the two-phase flow zone of the curve. The decreasing of the mass flux is more rapid for the drift flux model case: the pressure drop computed with the HEM and with the drift flux model with the same mass are in fact higher for the latter model, as already observed in Figure 3.12.

3.4 Linear stability analysis

In this part of the chapter the results of the linear stability analysis performed on a single boiling channel by means of the model described are illustrated.

Such analysis has been done by means of *COMSOL Multiphysics* code, in particular, its eigenvalue solver has been used on the model described above, put in a suitable form.

Later on, the following topics are illustrated:

- the adopted stability criterion;
- the methodology of analysis;
- the results.

3.4.1 The stability criterion

The stability criterion used to perform the respective analysis is quite different from the classical criterion of the Automatic Control Theory. According to this one, a linear or linearized model can be represented with the state equation system:

$$\begin{cases} \dot{x}(t) = A\,x(t) + B\,h(t) \\ y(t) = C\,x(t) + D\,h(t) \end{cases} \tag{3.22}$$

where x is the state vector, y is the output vector, h is the input one while A, B, C, D are constant element matrix. In particular, the system stability analysis can be performed by evaluating the real part of the eigenvalues of matrix A, which is the so-called dynamics matrix. If s_i is a generic eigenvalue, the intrinsic stability condition is:

$$\Re\{s_i\} \leq 0 \qquad \text{for} \qquad i = 1, \ldots \tag{3.23}$$

being the system modes:

$$\widetilde{x}_i(t) = \widetilde{x}_{i0}\, e^{s_i t} = x_0\, e^{\Re\{s_i\} t}\, [\cos(\Im\{s_i\}\, t) + i \sin(\Im\{s_i\}\, t)] \qquad \text{for} \qquad i = 1, \ldots$$

in the sum of which every time-dependent solution can be divided [7].

In order to apply this criterion to the boiling channel model, which is non-linear model based on PDE, it should be transformed in a ODE system like the (3.22). Practically, linearizing the equation system around an equilibrium point allows to write a ODE for each degree of freedom. This operation can be done by *COMSOL Multiphysics*, nevertheless another approach has been used, being the total number of degrees of freedom too big. This approach consisted in the use of the *COMSOL Multiphysics* eigenvalue solver. By using it, the equation system is linearized around an equilibrium point, the constant source terms are neglected and the temporal derivative operator is substituted in this way [8]:

$$\frac{\partial}{\partial t} \quad \longmapsto \quad -\lambda$$

where λ is the eigenvalue. The standard PDE problem solved by *COMSOL Multiphysics* is[4]:

$$\boldsymbol{e_a}\,\frac{\partial^2 \boldsymbol{u}}{\partial t^2} + \boldsymbol{d_a}\,\frac{\partial \boldsymbol{u}}{\partial t} + \nabla \cdot \boldsymbol{\Gamma} = \boldsymbol{F}$$

[4] cf. equation (2.40)

and being, in this case, the term $\boldsymbol{e_a}$ equal to 0 the equation system solved becomes:

$$\boldsymbol{d_a} \cdot \frac{\partial \boldsymbol{u}}{\partial t} = \boldsymbol{F} - \nabla \cdot \boldsymbol{\Gamma} = \boldsymbol{F}' \quad \longmapsto \quad -\lambda \, \tilde{\boldsymbol{d}}_{\boldsymbol{a}} \cdot \tilde{\boldsymbol{u}} = \tilde{\boldsymbol{F}}' \tag{3.24}$$

where $\tilde{\boldsymbol{u}}$ is the eigensolution and λ is the associated eigenvalue. In equation (3.24) the terms $\tilde{\boldsymbol{d}}_{\boldsymbol{a}}$ and $\tilde{\boldsymbol{F}}$ are the linearized and versions of the previous ones, moreover $\tilde{\boldsymbol{F}}'$ is also deprived of the constant source terms. This solver is generally used to study the system's natural oscillations [5].

The stability criterion deriving from the use of this solver is, also in this case, based on the sign of the real part of the eigenvalues, but it is expressed in a different way:

$$\Re\{\lambda\} \geq 0 \qquad \text{for} \qquad i = 1, \ldots \tag{3.25}$$

In fact, it can be easily demonstrated that the system modes are:

$$\tilde{u}_i(t) = \tilde{u}_{0i} \, e^{-\lambda_i t} \qquad \text{for} \qquad i = 1, \ldots$$

from which descends the stability condition (3.25).

In order to better clear this condition, let us consider the following simple example represented by the Cauchy problem:

$$\begin{cases} \dot{x}(t) = a \, x(t) \\ x(t_0) = x_0 \end{cases} \tag{3.26}$$

its solution is:

$$x(t) = x_0 \, e^{a \, t}$$

The stability of the system described by the (3.26) depends on the sign of the parameter a that, in this simple case, coincides with the entire dynamics matrix A of the general state-space model (3.22) and also with its eigenvalues set. According to the classic Liapunov stability definition [7], it results:

$$\begin{cases} a \leq 0 \quad \Longrightarrow \quad \text{(linearly) stable system} \\ a > 0 \quad \Longrightarrow \quad \text{(linearly) unstable system} \end{cases}$$

The implementation of the problem (3.26) in an acceptable form for the *COMSOL*

Multiphysics compiler is the following one:

$$\begin{cases} \boldsymbol{u} \equiv x(t) \\ \boldsymbol{F} \equiv a\,x(t) \\ \boldsymbol{u}(t_0) \equiv x_0 = 1.0 \\ \boldsymbol{e_a} = 0 \\ \boldsymbol{d_a} = 1 \\ \boldsymbol{\Gamma} = 0 \end{cases}$$

which has been implemented on a one-dimensional geometry characterized by a length of 1 m and the boundary conditions have been fixed to be the homogeneous Neumann type. The formulation of the problem, thanks to the absence of spatial derivative terms, is independent from the domain length and, more in general, from the geometry type: the value of the unknown is the same in every point.

By solving the problem implemented in this way using the *COMSOL Multiphysics* eigenvalue solver gives the result:

$$-\lambda = a$$

from which the stability criterion (3.25).

Obviously, even if the example is a very simple model formed by a single ODE, analogous considerations are easily applicable to more complex system as in the examined case of the boiling system: thousands of different eigenvalues can be computed from the software, sorted from the one with the smallest real part to the one with the greatest one, if just one of them has a negative real part the system is linearly unstable around that equilibrium point.

The described approach has already been used successfully by Lahey and Podowsky [9].

3.4.2 Adopted procedure

The methodology adopted for the stability analysis led to the drawing of stability maps for the system.

The procedure used for the accomplishment of the task can be divided in four main points:

- calculation of the equilibrium points set;
- adaptation of the model by changing the boundary conditions;
- running of the eigenvalue solver to investigate the stability of the point;
- localization of the stability boundary and its representation.

The linearization of the equation system has to be done around an equilibrium point. Since the task of this analysis is to analyze the stability of a boiling channel with fixed pressure drop across, the equilibrium points must be computed at fixed outlet pressure.

The calculation of such a steady state solution by means of a technique equal to the one used for the Δp vs G curves has not been possible. Indeed, the calculation of steady solutions with an imposed pressure drop across the channel gave some numerical problems. This is the reason why the G vs q'' curves have been computed as described in section 3.3.2: they are used to compute steady state solutions, useful for stability analysis.

Once the steady solutions were available and have stored, the boundary conditions have been changed from the imposed inlet flow rate case[5]:

$$\begin{cases} \text{Dirichlet:} \\ R_1 = p_{in} - u_1(0) = 0 \\ R_2 = G_{in} - u_2(0) = 0 \\ R_3 = h_{in} - u_3(0) = 0 \end{cases} \qquad \begin{cases} \text{Neumann:} \\ G_1 = -\Gamma_1(L) \\ G_2 = -\Gamma_2(L) \\ G_3 = -\Gamma_3(L) \end{cases} \tag{3.27}$$

to the imposed outlet pressure case:

$$\begin{cases} \text{Dirichlet:} \\ R_1 = p_{in} - u_1(0) = 0 \\ R_2 = 0 \\ R_3 = h_{in} - u_3(0) = 0 \end{cases} \qquad \begin{cases} \text{Dirichlet:} \\ R_1 = p_{out} - u_1(L) = 0 \\ R_2 = 0 \\ R_3 = 0 \end{cases} \tag{3.28}$$

In this way, *COMSOL Multiphysics* compiler solves an eigenvalue problem which contains the reaction forces due to the new boundary conditions set.

[5] cf. equations (2.53) and (2.54)

In correspondence to each steady solution the eigenvalue solver has been run and the stability information, that is the sign of the real part of the eigenvalue, has been got. These informations allowed the build up of stability maps. Each map has been drawn in terms of the subcooling number N_{sub} and the phase-change number N_{pch}, as suggested by [10]. The computed G vs q'' steady states can be easily converted in a phase change number set, being:

$$N_{pch} = \frac{q'' P L}{G A (h_V - h_L)} \frac{\rho_L - \rho_V}{\rho_V}$$

so, to build the map, the eigenvalues have to be determined for the N_{pch} set for different values of the inlet subcooling, i.e. for different values of N_{sub}, being the latter one:

$$N_{sub} = \frac{h_L - h_{in}}{h_V - h_L} \frac{\rho_L - \rho_V}{\rho_V}$$

The entire procedure has been repeated for different values of K_{in} and K_{out} and both with HEM and the drift flux model A.

3.4.3 Results

In this final part of this section, the obtained results are illustrated. The object of this analysis is, as said above, a single boiling channel uniformly heated, whose pressure drop across is kept constant by means of two plena, like shown in Figure 3.1.

In order to test the fairness of the results of the analysis, the calculations have been performed by using operating conditions similar to the one used both in [1] and [11] in terms of system geometry, pressure, K_{in} and K_{out}.

About the geometry of the system, the same values of Table 3.1 have been used, while, with regards to the operating conditions, the system pressure has been fixed to 7.0 MPa (inlet plenum), the couples of K_{in} and K_{out} and the respective pressure drop across the channel that have been investigated are:

$$\begin{aligned} &1.\quad K_{in} = 25 \;-\; K_{out} = 5 \quad \text{with} \quad \Delta p = 80\,\text{kPa} \\ &2.\quad K_{in} = 12 \;-\; K_{out} = 5 \quad \text{with} \quad \Delta p = 70\,\text{kPa} \\ &3.\quad K_{in} = 12 \;-\; K_{out} = 30 \quad \text{with} \quad \Delta p = 80\,\text{kPa} \end{aligned} \tag{3.29}$$

The first and the second couples are identical to the ones used in [1] and in [11]

respectively, the third one has been chosen in order to evaluate the effects of an outlet throttling greater than the inlet one.

With regards to channel pressure drop values, they have been chosen arbitrarily in order to get not too high values of the mass flux. Anyway, the stability maps should not be affected too much [10].

The obtained results, that is, the stability maps, have been compared with the ones obtained by Ambrosini et al. with a simple linearized HEM widely described and discussed in [12] and in [13].

Later on, the maps obtained are shown and briefly discussed.

In Figure 3.14a is represented the comparison between the results obtained with both the HEM and the drift flux model and the results obtained in [1]. As it is shown, there is a quite good agreement. The stability boundaries calculated with the models used in this work are very close each others and they are also close to the curve obtained by Ambrosini [1].

It can be noticed that the boundary computed with the drift flux model is the one more shifted to the left: the effect of the slip ratio is a destabilizing effect. In fact, being the instability region at the right of the boundary, each effect that cause the shift of the boundary toward the left of the plane is to be considered destabilizing. Nevertheless, there is not great difference between the boundaries obtained in this work.

The smallness of this difference is more evident in Figure 3.14b, in which the curves are enveloped for low subcooling number values and begin to detach for increasing subcooling. This is maybe due to the fact that the increase of the subcooling degree leads to the appearing of the Ledinegg type instability, as in [1]. Indeed, as observed from the results of the static analysis of the previous section, the Δp vs G curve shown a negative slope as the subcooling increases and this effect is underlined if the drift flux model is used.

The map resulting from the last couple of K_{in} and K_{out} is shown in Figure 3.14c. Also in this case the boundaries obtained with the two different models are quite enveloped, with the drift flux boundary slightly shifted on the left: this trend seems then to be common to the three maps. The effect of Ledinegg instability can be observed

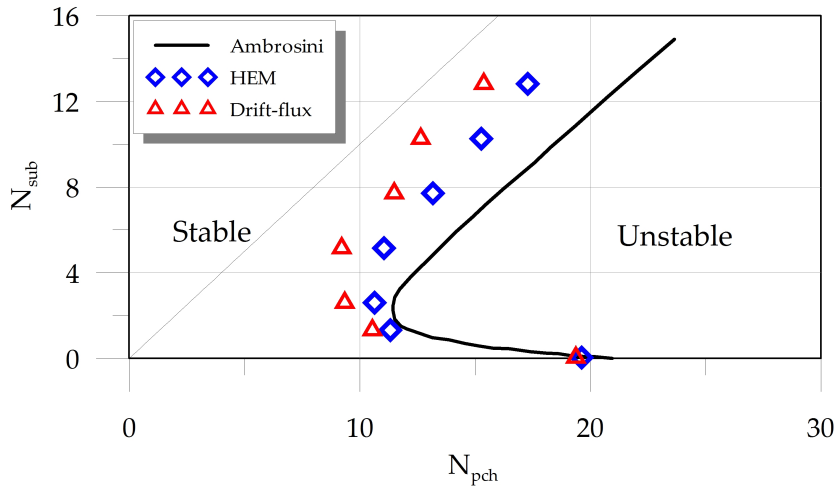

(a) Stability maps obtained with $K_{in} = 25$ and $K_{out} = 5$.

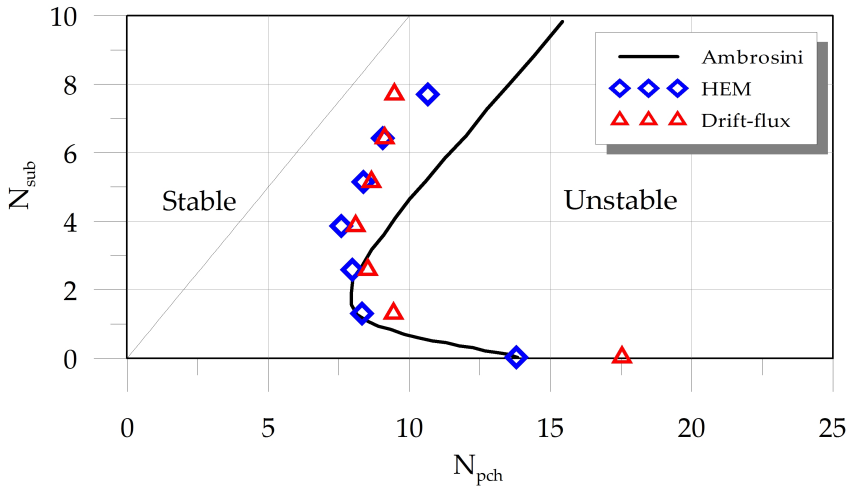

(b) Stability maps obtained with $K_{in} = 12$ and $K_{out} = 5$.

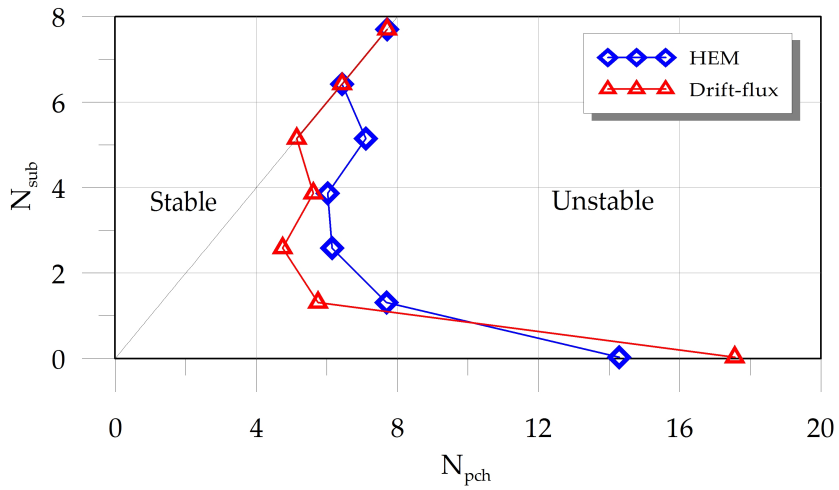

(c) Stability maps obtained with $K_{in} = 12$ and $K_{out} = 30$.

Figure 3.14: Comparison between stability maps obtained with different models.

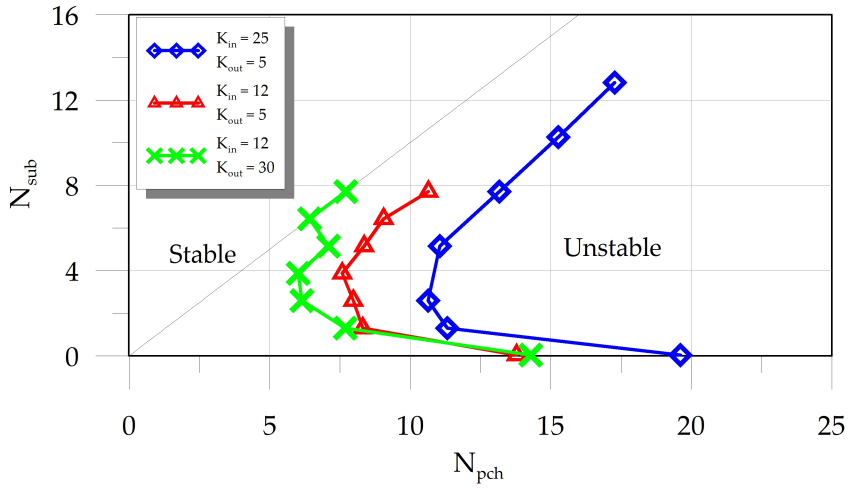

(a) Stability maps obtained with HEM.

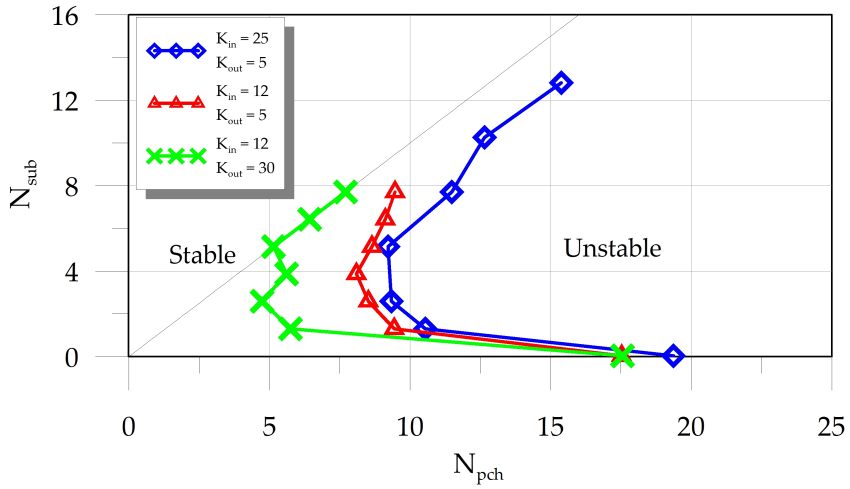

(b) Stability maps obtained with the drift flux model.

Figure 3.15: Comparison between stability maps obtained at different values of K_{in} and K_{out}.

to appear as the subcooling number increases. Also this result supports the results of static stability analysis made by means of the Δp vs G curves, which showed a sharp *"S"* shape in these throttling conditions. Furthermore, the drift flux model boundary shows the characteristic shape due to the Ledinegg instabilities a little before than the HEM one. The main reason that leads to this behavior is maybe the different two-phase friction models: the friction multiplier computed by means of the drift flux model is much higher than the one computed by means of HEM and it accentuates the negative slope of the curve.

Finally, Figure 3.15 shows the comparison between the curves obtained in corre-

spondence to the three couples of K_{in} and K_{out}. As expected, an increase of the inlet throttling is stabilizing (the stability boundary shifts to the right) while an increased outlet throttling destabilizes the system (the stability boundary shifts to the left). This effect is observed for both the models used.

3.5 Transient analysis

In this section, the results of some time dependent simulations are reported. These simulations have been run starting from two different operating conditions: a stable one and an unstable one.

Transient analyses performed in stable conditions have been realized by computing the system response to a thermal power step and, in these analyses, both the HEM and the drift flux model have been used. The effect of the presence of the wall has been investigated as well by simulating the responses both with and without the wall.

Also transient analyses starting from an unstable conditions have been done but, in this case, the system has been let free to evolve from this unstable steady state, that is, none external input has been given (free dynamics). In these simulations the wall effect has been studied while, about the slip model, just HEM has been used because of numerical problems due to the drift flux model correlations.

In the following, a single section is dedicated to each of these analyses.

3.5.1 Stable response of the system

The stable response of the system to an input step of thermal power has been obtained, as said, both with HEM and drift flux model and with and without the wall.

The stable steady state used as initial condition is the one obtained by solving the system (3.14) with the following parameters:

- $p_{in} = 7.0\,\mathrm{MPa}$;
- $h_{in} = 1165\,\mathrm{kJ\,kg^{-1}}$, i.e. $T_{in} = 266\,^{\circ}\mathrm{C}$;
- $K_{in} = 25$ and $K_{out} = 5$;

- $\Delta p = 80\,\text{kPa}$, i.e. $p_{out} = 6.92\,\text{MPa}$;
- $q = 57\,\text{kW}$, i.e. $q'' = 400\,\text{kW m}^{-2}$.

which correspond to the point of the $(N_{pch} - N_{sub})$ plane of coordinates:

$$\begin{cases} N_{pch} = 3.84 \\ N_{sub} = 1.31 \end{cases}$$

The transient analysis have been done by solving the complete system:

$$\begin{cases} \dfrac{\partial \rho_m}{\partial t} + \dfrac{\partial G}{\partial z} = 0 \\ \dfrac{\partial G}{\partial t} + \dfrac{\partial}{\partial z}\left(\dfrac{G^2}{\rho_m^+}\right) = -\dfrac{\partial p}{\partial z} - \rho_m g \sin\theta - \phi_{lo}^2 f \dfrac{G^2}{2\rho D} - \sum_{j=in}^{out} K_j \phi_{lo}^2 \dfrac{G^2}{2\rho}\delta\left(z - z_j\right) \\ \dfrac{\partial}{\partial t}\left(\rho_m h_m - p\right) + \dfrac{\partial}{\partial z}\left(G h_m^+\right) = \dfrac{U_{ex} P \left(T_w - T_b\right)}{A} + \\ \quad + \dfrac{G}{\rho_m}\left[\phi_{lo}^2 f \dfrac{G^2}{2\rho D} + \sum_{j=in}^{out} K_j \phi_{lo}^2 \dfrac{G^2}{2\rho}\delta\left(z - z_j\right) + \dfrac{\partial p}{\partial z}\right] \\ \dfrac{M_w c_w}{P L}\dfrac{\partial T_w}{\partial t} = q'' + \Delta q''(t) - U_{ex}\left(T_w - T_b\right) \\ + \text{boundary conditions} \\ + \text{constitutive laws and closure equations} \end{cases} \tag{3.30}$$

in which the term $\Delta q''(t)$ is the thermal power step:

$$\Delta q''(t) = \Delta q_0'' \, H(t - t_0)$$

where $\Delta q_0''$ is the power step amplitude, equal to $5\,\text{kW m}^{-2}$, that is about the 1.25% of the steady thermal flux, and $H(t - t_0)$ is the Heaviside step function, where t_0 has been fixed to 5 s.

In order to run simulations by using HEM and the drift flux model, the concentration parameter and the effective drift flux velocity have been fixed as follows:

$$\begin{cases} \text{HEM:} \\ C_0 = 1.0 \\ V_{vj} = 0.0 \end{cases} \qquad \begin{cases} \text{Drift flux:} \\ C_0 = 1.13 \\ V_{vj} = 0.0 \end{cases}$$

The effective drift flux velocity has been neglected also in the drift flux model calculations because of numerical problems given by the correlations.

With regards to the wall effect, it can be removed simply by vanishing its thickness $(t_w = 0)$.

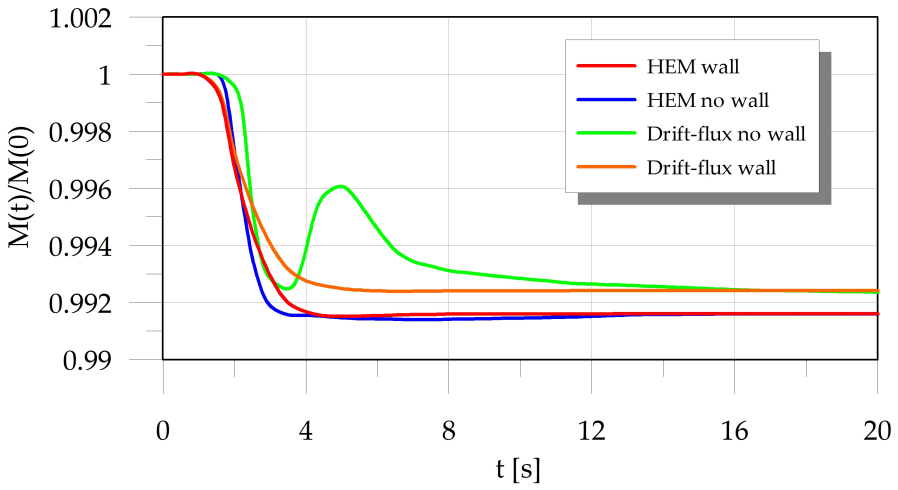

Figure 3.16: Water mass inside the channel.

Finally, Heaviside step function has been implemented in a way similar to that one used for local inlet and outlet pressure drops (section 3.2.2). Hereby the step has been given in time, rather than in space, with a maximum width of 0.1 s.

The simulations have been run by using *COMSOL Multiphysics* time dependent solver with the default settings, in which the computational time step amplitude is automatically chosen from the compiler.

Later on the main results are reported and briefly discussed.

In Figure 3.17a the system response in terms of outlet mixture enthalpy is shown. It can be seen that the response of the system without the wall is stiffer, as expected, because of the absence of the time delay introduced by the wall. The drift flux model gives an oscillating transient response (with non-minimum phase features) which damps out if the wall is present.

Figure 3.17b shows, instead, the boiling boundary shifting toward the channel inlet in response to an increase of the thermal power given to the fluid.

Figure 3.17 shows the transient response of both the inlet and the outlet flow rate and of the outlet vapor and liquid mass flow rate. In all the four examined cases, the inlet mass flow rate decreases at first, then slightly increases to reach the new final steady state. The outlet mass flow rate shows an opposite behavior. This fact is due to the instantaneous fluid expansion that tends to contrast the fluid entrance and to force the outgoing. In confirmation of this fact, the variation of the fluid mass inside

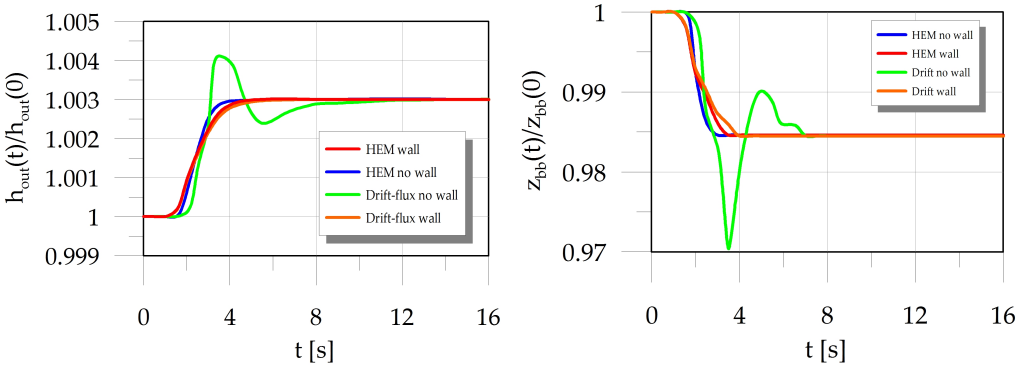

(a) Enthalpy.

(b) Boiling boundary.

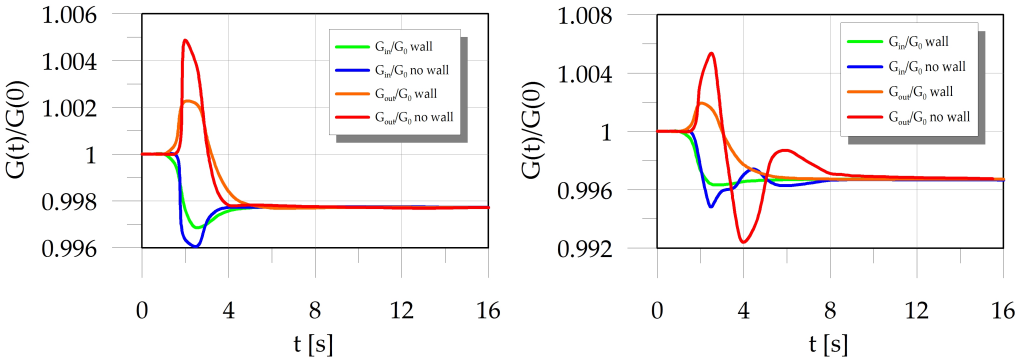

(c) Inlet and outlet mass fluxes. HEM.

(d) Inlet and outlet mass fluxes. Drift flux model.

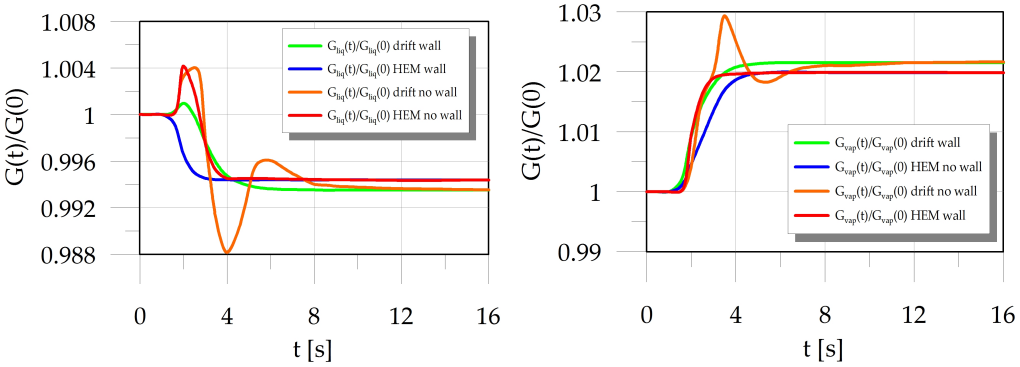

(e) Liquid mass flux at channel exit.

(f) Vapor mass flux at channel exit.

Figure 3.17: Enthalpy, boiling boundary and mass fluxes transient responses.

the channel is shown in Figure 3.16: the static fluid mass in the channel decreases as the average density ρ_m is affected by the extension of the two-phase flow zone, due to the decreasing of the boiling boundary position, which is very little dense because of the presence of the vapor phase.

Figures 3.18 and 3.19 show the different contributions to the channel pressure drop.

As expected, the frictional two-phase contribution increases while the single-phase contribution decreases, exactly in opposition, in agreement with the variation of the boiling boundary position. However, the total frictional pressure drop increases as expected (Figure 3.21a).

Similar consideration can be drawn about the accelerative pressure drop (Figures 3.18e and 3.18f). Nevertheless, the single-phase contribution can be neglected without problems as can be easily deduced from the comparison between Figures 3.18e, 3.18f and 3.21c: it is evident that accelerative pressure drop dynamics is made by the two-phase contribution only.

About the gravitational pressure drops, Figure 3.21b shows the decrease of the total contribution due to the fact that the fluid becomes lighter because of the already mentioned decrease of the fluid density.

With regards to the single components of the gravitational pressure drop, it can be noticed from Figures 3.18c and 3.18d that the single-phase contribution decreases more than the two-phase one in response to the decrease of the boiling boundary position, this is due to the greater density (heavy) of the single-phase mixture: a decrease of its length influences sensibly the single-phase gravitational pressure drop. On the contrary, the two-phase contribution variation is very small.

Finally, the local pressure drops transient behavior is shown in Figure 3.19. The figure shows that the inlet pressure drop contribution increases, while the outlet one decreases and both the transients follow the inlet and outlet mass flux behavior.

All the transients are affected by the presence of the wall: the response of a system without wall is stiffer than the one of the system with the wall. The latter one seems to be more physically sensitive.

The reason for which the presence of the wall influence so much the responses

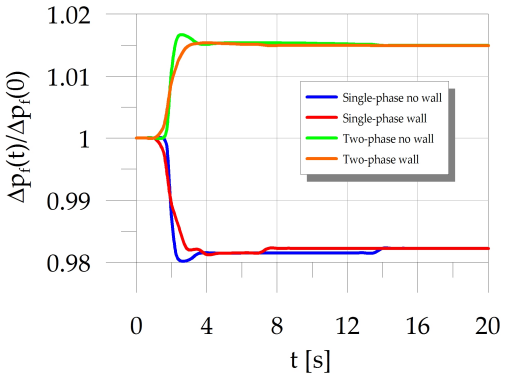

(a) Single and two-phase contributions to the frictional pressure drops. HEM.

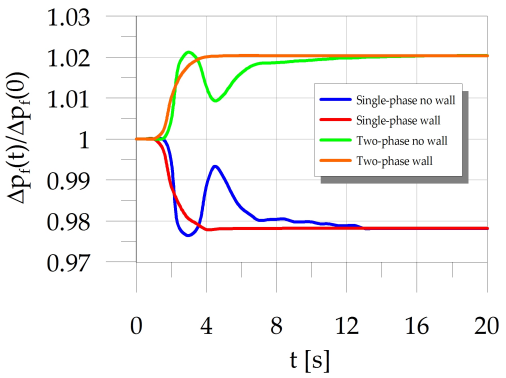

(b) Single and two-phase contributions to the frictional pressure drops. Drift flux model.

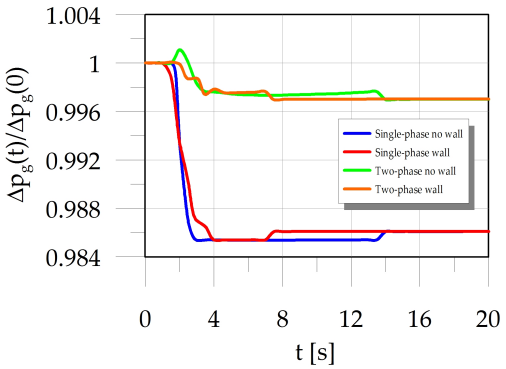

(c) Single and two-phase contributions to the gravitational pressure drops. HEM.

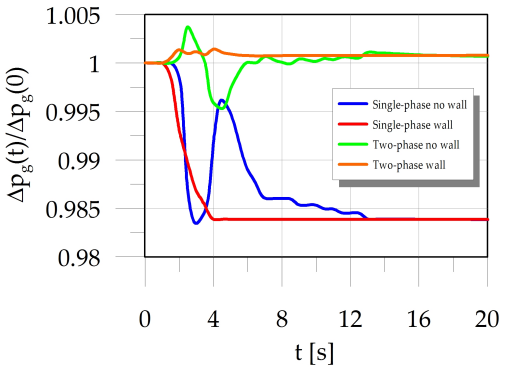

(d) Single and two-phase contributions to the gravitational pressure drops. Drift flux model.

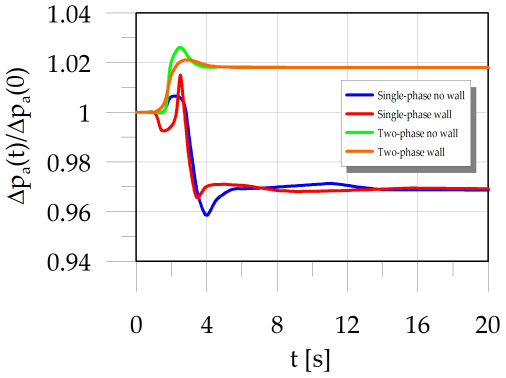

(e) Single and two-phase contributions to the accelerative pressure drops. HEM.

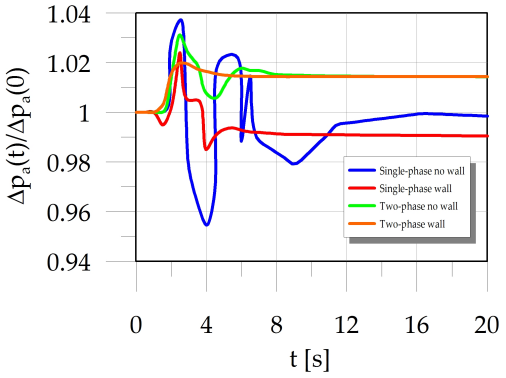

(f) Single and two-phase contributions to the accelerative pressure drops. Drift flux model.

Figure 3.18: Distributed contributions to the pressure drop.

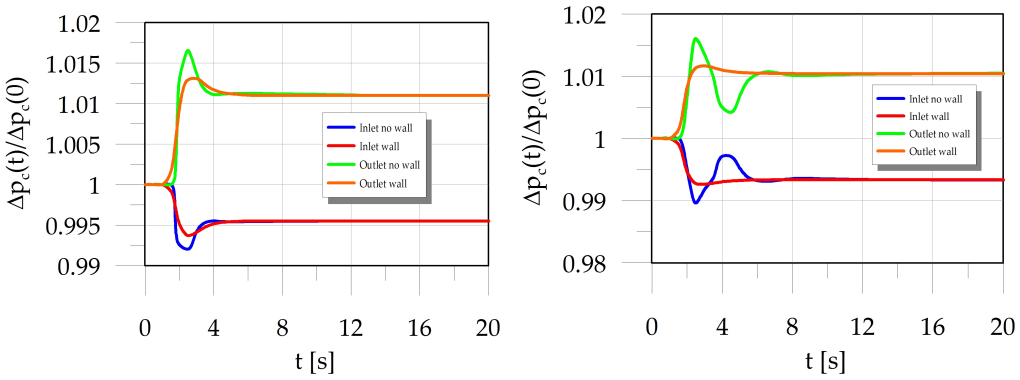

(a) Inlet and outlet local pressure drops contributions. HEM.

(b) Inlet and outlet local pressure drops contributions. Drift flux model.

Figure 3.19: Concentrate contributions to the pressure drop.

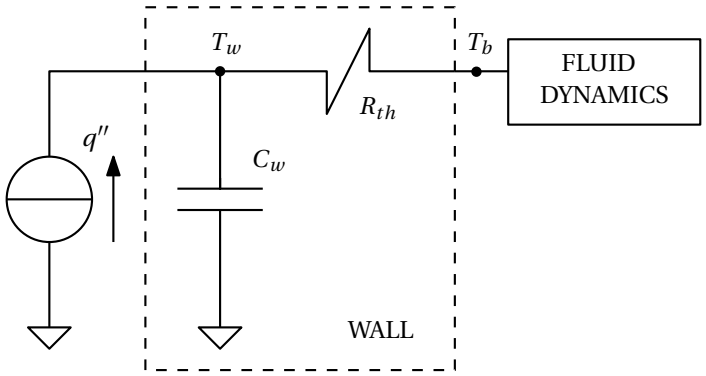

Figure 3.20: Wall electrical analogy representation.

can be easily understood by consider a simple electrical analogy. The simple wall model (3.9) can be represented by means of the circuit of figure 3.20, in which the capacitor C_w represents the wall energy storage capacity given by:

$$C_w = \frac{M_w\, c_w}{P\, L}$$

and R_{th} is the thermal resistance between wall and fluid, given simply by $1/U_{ex}$. The DC supply is representative of the constant thermal power input. The time constant calculated in the previous section is the inverse of the product $R_{th}C_w$, that is the circuit time constant. It can be noticed that the wall model acts as a low-pass filter placed between the arbitrary external source and the fluid dynamics part of the model: the input given to this one results then attenuated thanks to the high frequency cutting.

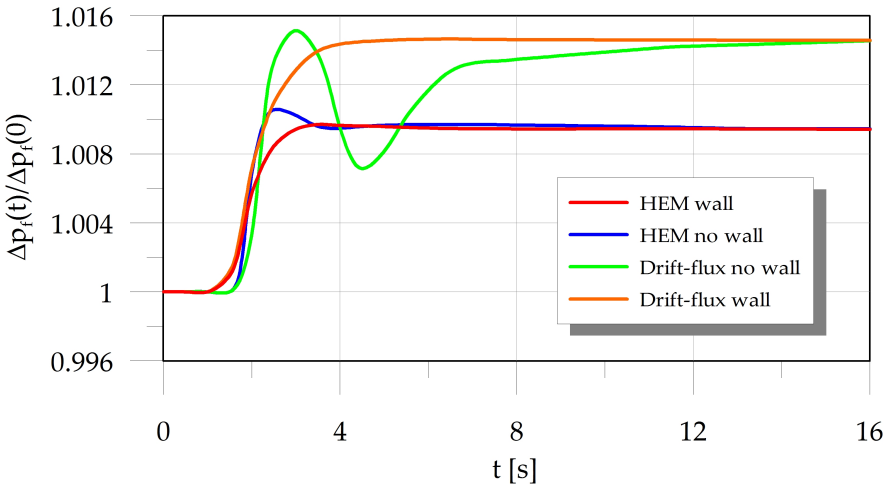

(a) Frictional contribution.

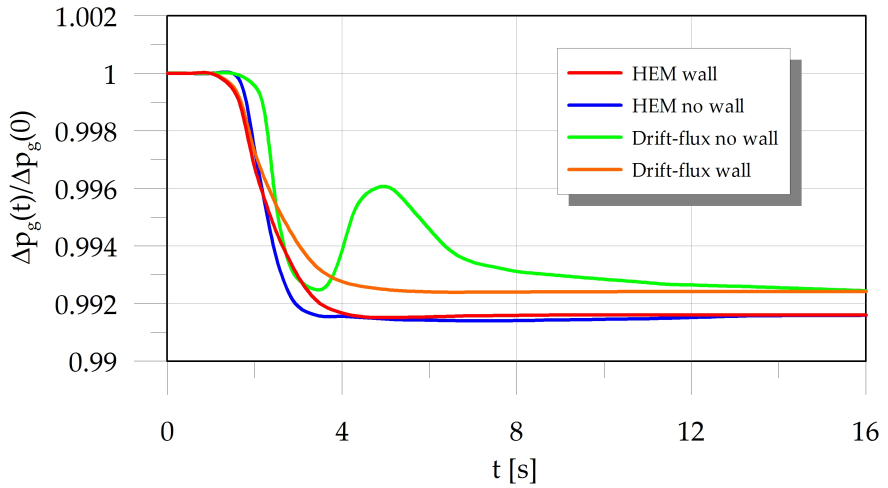

(b) Accelerative contribution.

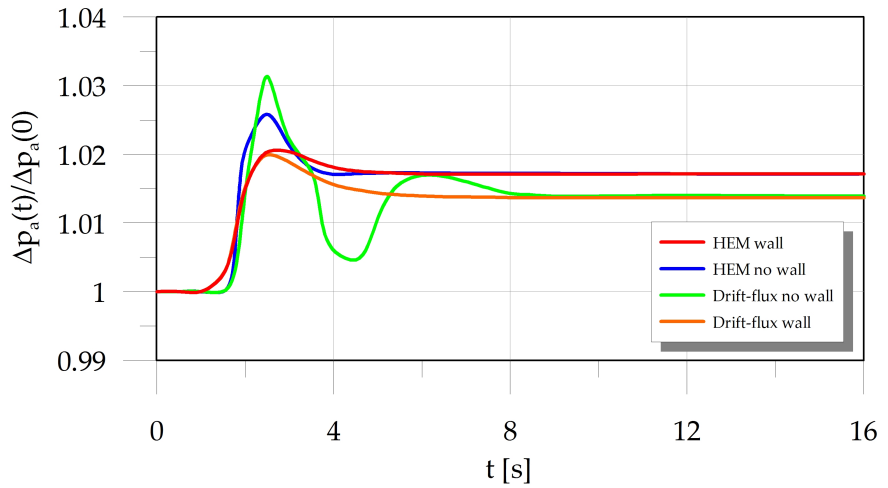

(c) Gravitational contribution.

Figure 3.21: Different contribution to the total pressure drop.

3.5.2 System dynamics in unstable conditions

In this section the dynamics of the system in unstable conditions has been simulated, by using the HEM, with and without the wall. The using of the drift flux model has not been possible from numerical point of view.

The parameters used to obtain the initial steady state condition are:

- $p_{in} = 7.0\,\mathrm{MPa}$;
- $h_{in} = 1165\,\mathrm{kJ\,kg^{-1}}$, i.e. $T_{in} = 266\,^{\circ}\mathrm{C}$;
- $K_{in} = 12$ and $K_{out} = 30$;
- $\Delta p = 80\,\mathrm{kPa}$, i.e. $p_{out} = 6.92\,\mathrm{MPa}$;
- $q = 92.6\,\mathrm{kW}$, i.e. $q'' = 650\,\mathrm{kW\,m^{-2}}$.

which correspond to the point of the $(N_{pch} - N_{sub})$ of coordinates:

$$\begin{cases} N_{pch} = 7.08 \\ N_{sub} = 1.31 \end{cases}$$

The simulations have been run by solving system (3.30).

In the case in which the wall is not present the thermal power input step has been eliminated:

$$\Delta q''_0 = 0$$

Indeed in this case the system oscillates without any external perturbation.

In the case of wall presence instead a thermal power input step has been given: in this case, indeed, there is not any oscillation without external perturbation. The amplitude of the thermal power input step is, also in this case, of about the 1 % ($6.5\,\mathrm{kW\,m^{-2}}$).

Later on the main results are reported and briefly discussed.

The outlet enthalpy is shown in Figure 3.22. It can be noticed that both with and without the wall the oscillations seem to have a period of about 2 s which is a time comparable to twice the transit time in the system, of the order of about 1 s.

For this reason the oscillations could be considered physical as they are probably density wave oscillations (cf. chapter 1). Anyway, the fact that in case of wall absence

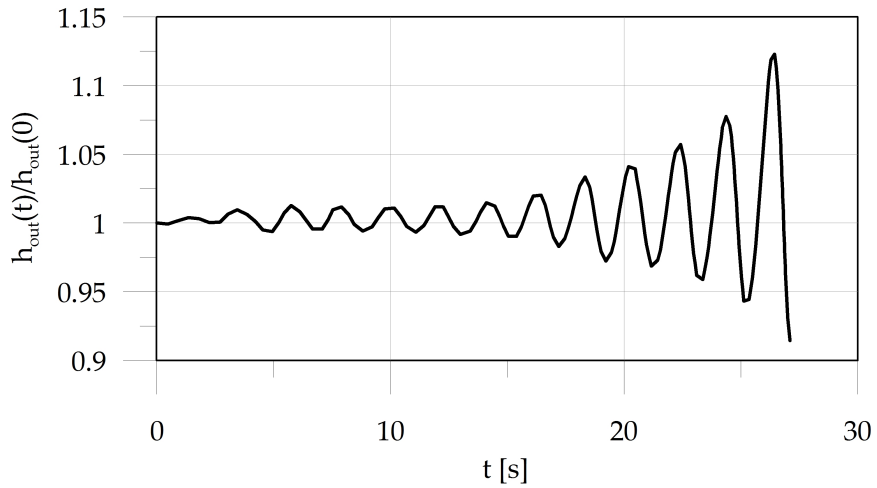

(a) Without wall.

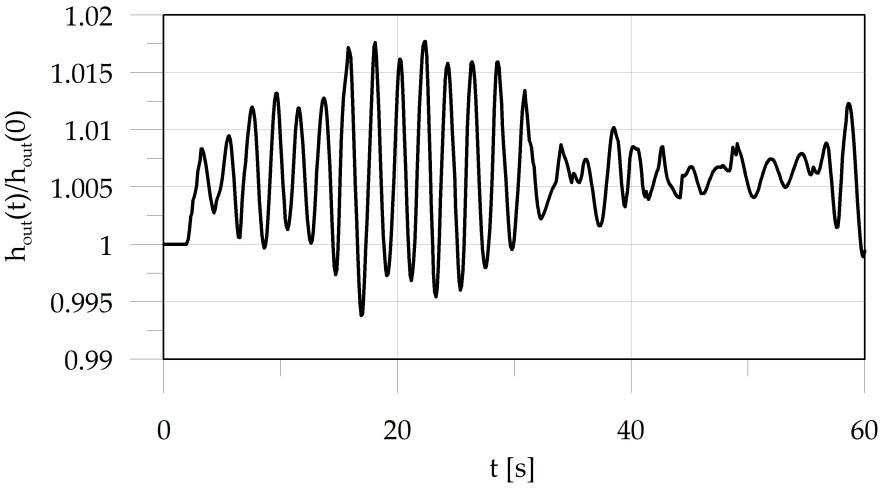

(b) With wall.

Figure 3.22: Outlet enthalpy.

no external perturbations are needed to induce the oscillations means that such oscillations are probably triggered by numerical fluctuations which behave like small external perturbations. Moreover, it can be observed that in the plot 3.22a the amplitude seems to diverge unlike the plot 3.22b.

With regards to the mass flow rates, Figure 3.23 shows the transient behavior of inlet and outlet mass flow rates in the two considered cases. It can be noticed that both in the plot 3.23a and in the plot 3.23b the oscillations seem to be exactly in counterphase: it suggests that the propagation of the information about the flow rate travels about at the fluid velocity along the channel as a kinematic wave.

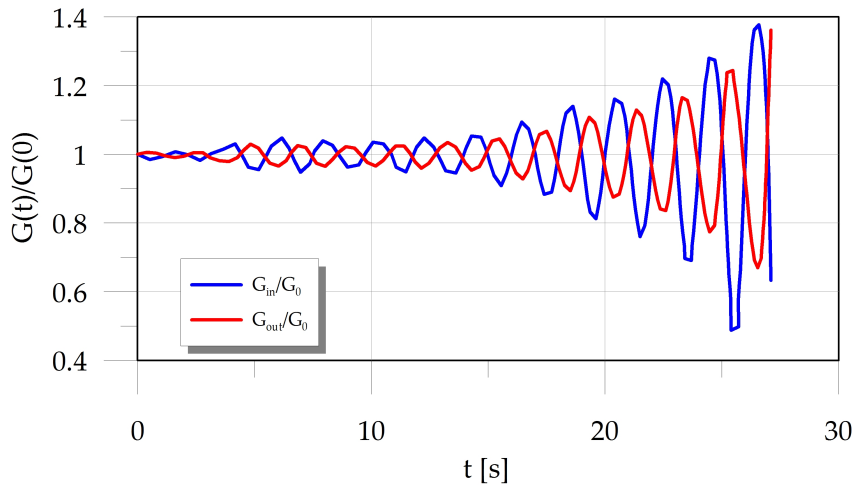

(a) Without wall.

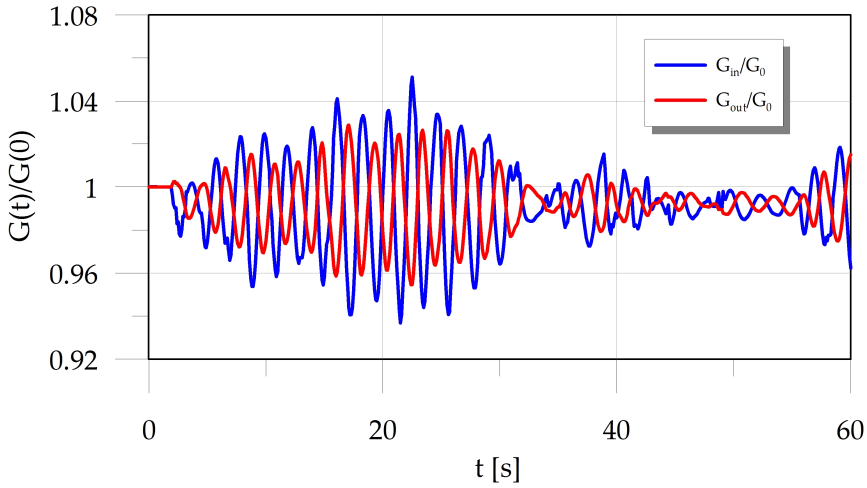

(b) With wall.

Figure 3.23: Mass fluxes at channel inlet and outlet.

In the case of wall presence the general trend of the mass flow rate is to decrease as response to the input thermal power step while in the other case (plot 3.23a) it remains around unity.

More complex is the dynamics of the liquid and of the vapor mass flow rate at the outlet of the channel. Although they seem to have the same period they are not in phase opposition: they show a constant phase shift. This is due to the fact that they are related to the phase of boiling boundary oscillation which affects the exit quality, this one affects in turn the outlet liquid and the vapor flow rate.

As it happens for the inlet and outlet flow rate, the plot of Figure 3.24b evidences

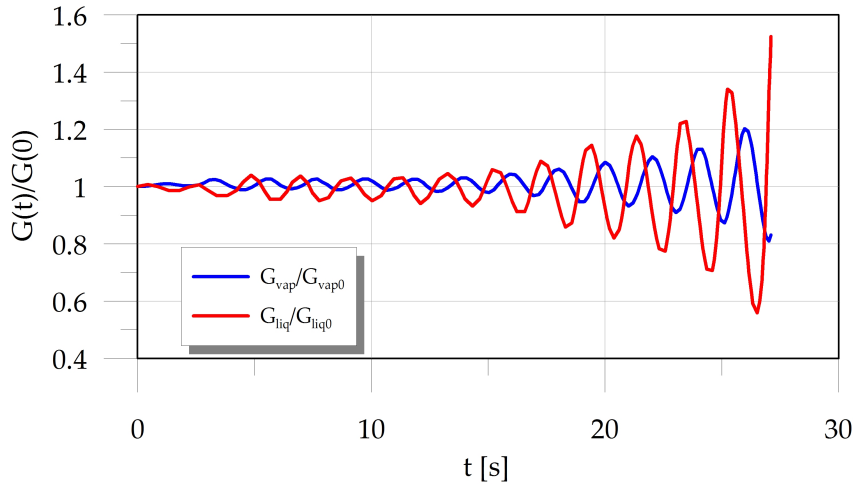

(a) Without wall.

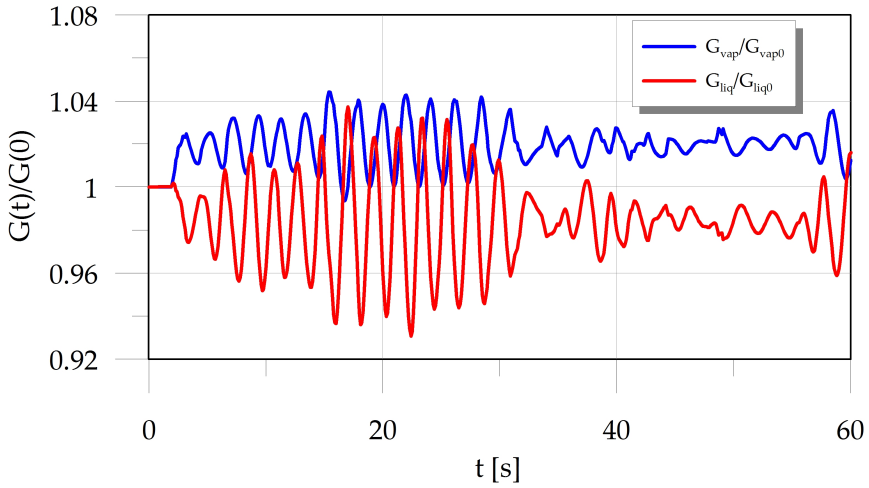

(b) With wall.

Figure 3.24: Liquid and vapor mass flow rates.

the increase of the vapor outlet flow rate and the decrease of the liquid flowrate.

The contributions to the total pressure drop across the channel are shown in Figure 3.25, 3.26 and 3.27.

In both the cases, some aspects can be observed.

- The frictional pressure drop single-phase and two-phase contributions are exactly in phase opposition and the relative variation of the single-phase one (blue lines of Figures 3.25a and 3.26a) is higher than the two-phase one because of the fact that the former are smaller in absolute values.

- The gravitational pressure drop contributions are characterized by a constant

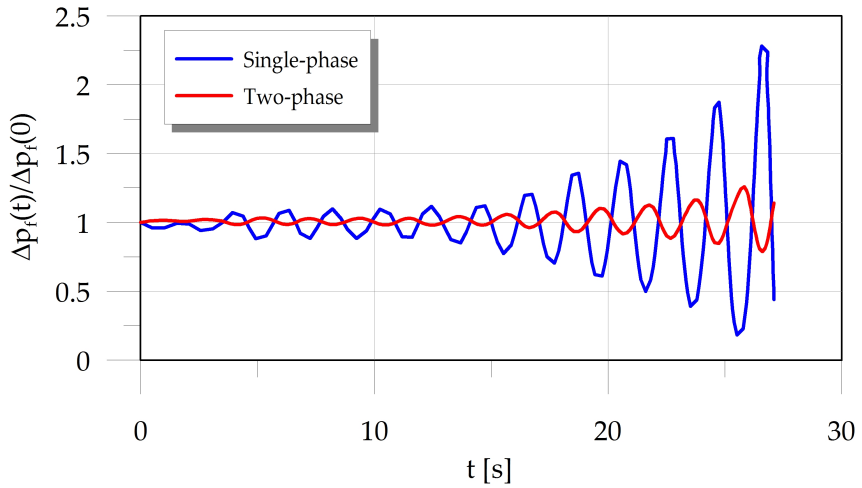

(a) Frictional contribution.

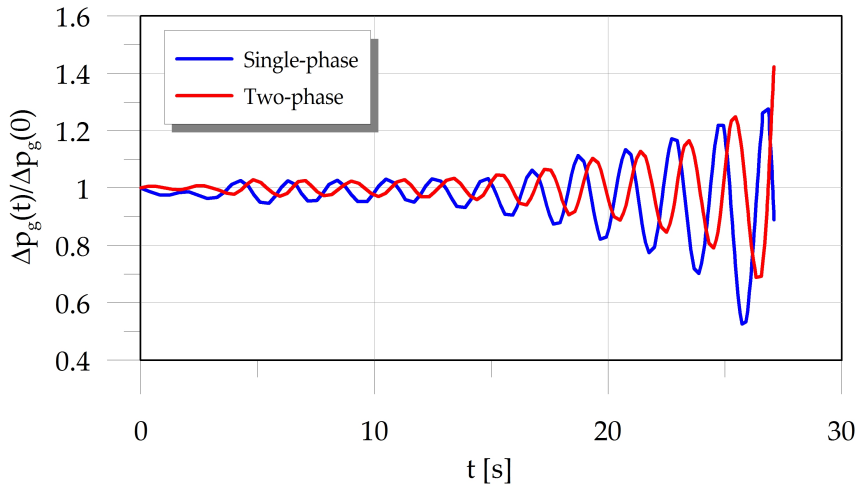

(b) Gravitational contribution.

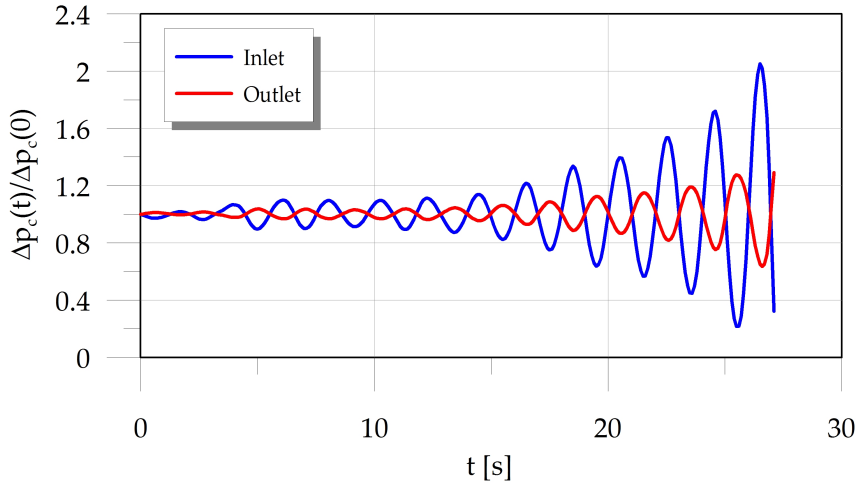

(c) Concentrate contribution.

Figure 3.25: Pressure drop contributions.

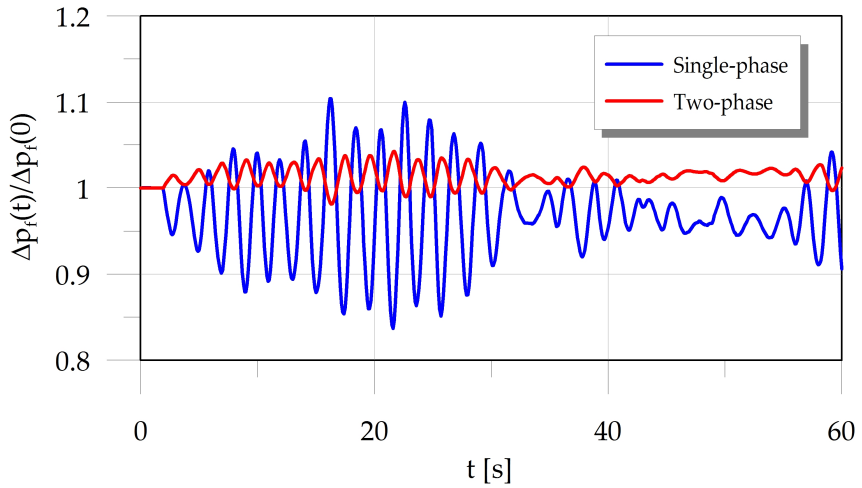

(a) Frictional contribution.

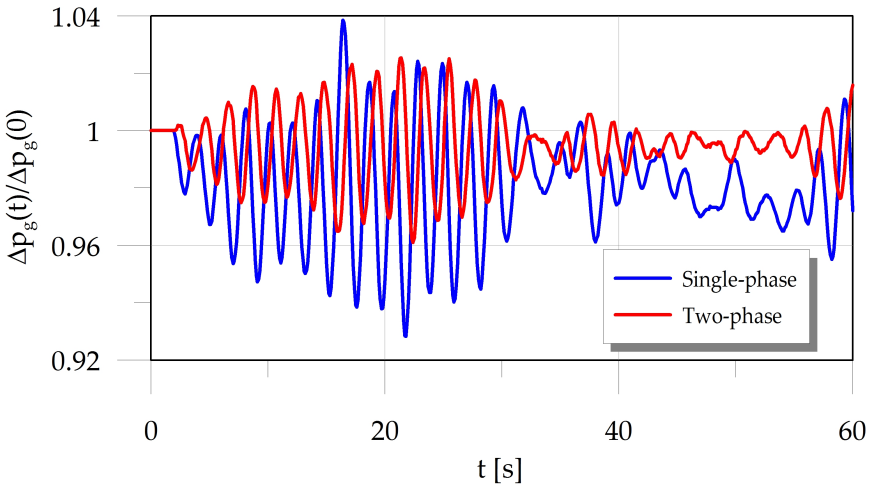

(b) Gravitational contribution.

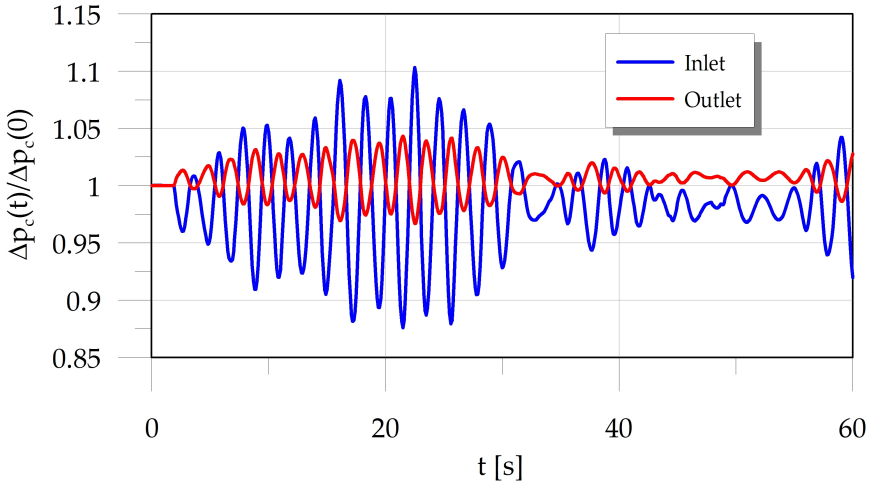

(c) Concentrate contribution.

Figure 3.26: Pressure drop contributions.

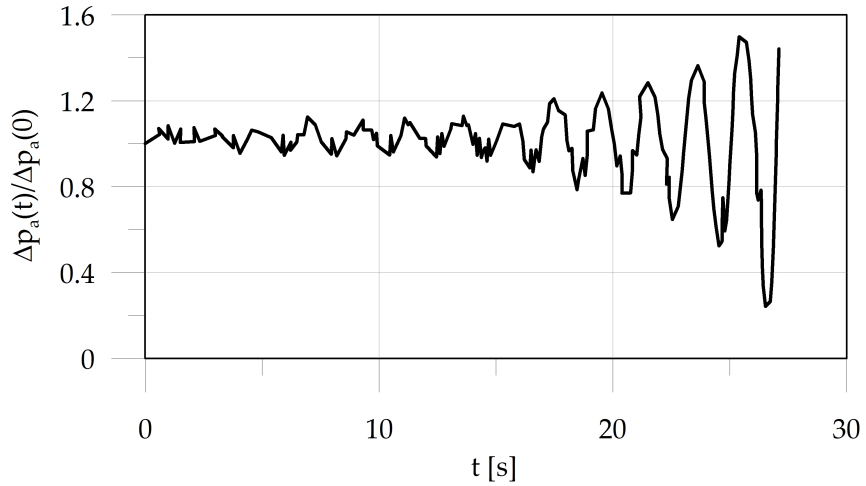

(a) Without wall.

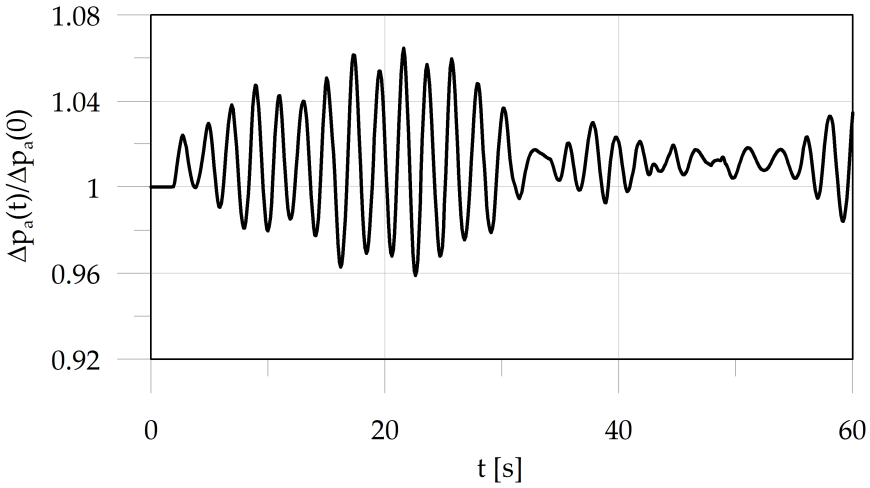

(b) With wall.

Figure 3.27: Accelerative pressure drops (total).

phase shift between single and two-phase contributions.

- The concentrate inlet and outlet pressure drop contributions are in phase opposition, it is mainly due to the fact that they are affected mostly by the inlet and outlet mass fluxes (Figure 3.23), therefore they follow their trend. It should be noticed that the inlet local pressure loss relative variation is greater than the outlet one: this is due to the fact that in these calculations $K_{in} < K_{out}$.

The accelerative contributions could not be represented as the others because the single-phase contribution is so small that its relative variation would be too huge to be represented and compared to the two-phase contribution. For this reason the total

contribution, that is practically the same of the total one, has been represented alone (Figure 3.27).

3.6 Conclusions

The results of the performed analyses have shown a good agreement both with some theoretical expectations and with some results available from open literature.

With regards to the steady analyses, the results of simulations run in the test case show the differences between the HEM and two different type of drift flux model. The models gave no remarkably different results in the calculations of enthalpy, quality and temperatures spatial distributions, and just small differences have been found in pressure spatial shapes. The main differences are in the slip ratio values and in the various contributions to the total pressure drops (local, frictional, gravitational, ...). In particular, the drift flux models gave values of the slip ratio very different from unity and this fact affects many other quantities, like velocities, void fractions and mixture densities. Anyway, the results seem to be very physically sensitive.

The characteristic curves of the system obtained are satisfactory. The analysis of these curves as function of the system parameters are, indeed, similar to the results reported by Kakac and Bon [3] and the system features in terms of static stability have been appreciated and confirmed. It has been observed, indeed, that the introduction of an inlet throttling tends to stabilize the system making the curve monotone, while an outlet throttling contributes to destabilize changing the curve shape into the *"S"* shape, with a negative slope.

The linear stability analysis performed led to the drawing of stability maps. These one have been compared with numerical results obtained by Ambrosini et al. [1], showing a quite good agreement. It has been observed that the increase of the outlet throttling shifts the stability boundary to the left, making the unstable zone larger, as expected and, in general, that the drift flux model seems to make the system less stable, being the obtained stability boundary more to the left than the one obtained with the HEM. Nevertheless, there is no great difference: the two boundaries are, indeed, quite enveloped.

The results of the transient analyses in the stable conditions evidenced mainly the effect of the wall. It has been observed that its presence tends to damp out the oscillations and to introduce delays in the system responses that make them softer than the ones obtained without the wall. This is true both by using the HEM and the drift flux model.

The results obtained in the unstable conditions have shown that, without the wall, the system begins to oscillate without any external perturbation and that the oscillation amplitude seems to diverge; with the wall, the oscillation must be triggered by an external perturbation and its amplitude does not diverge. Anyway, in both cases, an oscillation period comparable to the system transit time has been observed and this fact suggests that they reasonably considered as density wave oscillations.

Finally, considerations on the adoption of *COMSOL Multiphysics* in this analyses are required. About the stationary calculations, the stationary solver and the parametric one make their realization easy and reliable especially in those simulations in which the inlet flow rate has been imposed; nevertheless, these tools gave convergence problems as the boundary conditions are changed and outlet pressure is specified instead of inlet flow rate. Surely, the most big advantages emerged during the second part: indeed, the eigenvalue solver used to carry out the linear stability analysis resulted a valid instrument. Instead, several problems have been found during transient simulations: more precisely, all the correlations adopted gave so much numerical problems that the only results obtained are those ones corresponding to HEM adoption; to note however that, also in this case, this calculations were not easy to realize.

Bibliography

[1] Walter Ambrosini and Juan Carlos Ferreri. Analysis of basic phenomena in boiling channel instabilities with different flow models and numerical schemes. In *ICONE 14-89863*, 2006.

[2] Neil E. Todreas and Mujid S. Kazimi. *NUCLEAR SYSTEMS I - Thermal Hydraulic Fundamentals*. Taylor&Francis, 1989.

[3] S. Kakac and B. Bon. A review of two-phase flow dynamic instabilities in tube boiling systems. *International Journal of Heat and Mass transfer*, 2007.

[4] *COMSOL Multiphysics 3.5a Reference Guide*.

[5] *COMSOL Multiphysics 3.5a User's Guide*.

[6] Takashi Hibiki and Mamoru Ishii. One-dimensional drift-flux model and constitutive equations for relative motion between phases in various two-phase flow regimes. *International Journal of Heat and Mass transfer*, 2003.

[7] Paolo Bolzern, Riccardo Scattolini, and Nicola Schiavoni. *Fondamenti di controlli automatici*. McGraw-Hill, 2008.

[8] *COMSOL Multiphysics 3.5a Modeling Guide*.

[9] W. R. Schlichting, R. T. Lahey, M. Z. Podowsky, and T. A. Ortega Gómez. Stability analysis of a boiling loop in space. In *COMSOL Conference, Boston*, 2007.

[10] J.M. Delhaye et al. *Thermohydraulics of two-phase systems for industrial and nuclear engineering*. Hemisphere, 1981.

[11] W. Ambrosini, P. Di Marco, and J.C. Ferreri. Linear and nonlinear analysis of density wave instability phenomena. *International Journal of Heat and Technology*, 2007.

[12] Walter Ambrosini and Juan Carlos Ferreri. On the analysis of thermal-fluid-dynamic instabilities via numerical discretization of conservation equations. *Nuclear Engineering and Design*, 2002.

[13] Walter Ambrosini. Lesson learned from the adoption of numerical techniques in the analysis of nuclear reactor thermal-hydraulic phenomena. *Progress in Nuclear Energy*, 2008.

Chapter 4

Parallel channel preliminary study

Abstract

A suitable model for parallel channel systems has been developed. More precisely, this system is made by two different vertical channels connected by means of a lower and an upper plenum placed respectively at their bottom and top.

Such a model has been deduced starting from the one described and used in the previous chapters for a single channel system: indeed, it has been sufficient to duplicate it and to impose the opportune boundary conditions to achieve this task.

In this part of the work only a preliminary analysis has been performed by means of the model. In fact, the simulations have been done keeping the system in a single-phase operating condition and, among them, two steady states and one transient analysis have been examined. In particular, the latter one is a simulation of the flow rate regulation in one of the channels.

In order to assess on this system the methodology used to perform the linear stability analysis of the previous chapter, the eigenvalues of the linearized model have been computed and reported.

4.1 Introduction

The objective of this chapter is the description of the last part of the work: a preliminary study on single-phase parallel channels.

It has been articulated in two steps.

During a first one, an suitable model able to describe the behavior of such a physical system has been set up and implemented. Obviously, to do that the procedures used in the previous part of the work have been used: more precisely, the model for two-phase single channels previously created have been opportunely used to reproduce single-phase conditions and coupled by means of apposite boundary conditions. This step has been carried out using *COMSOL Multiphysics* code once again, in particular the *PDE General Form* module.

Instead, during the second one some simulations have been performed in order to verify the reliability of the model so created, and, on the other hand, to make a preliminary analysis.

Later on a description of each of these steps follows.

Finally, it has to be noted that this last part of the work has been developed with the main aim to constitute the basis for a more complex analysis of the behavior of two-phase parallel channel systems made by two or more connected channels.

4.2 The system and the model

The object of this section is the description of the physical system considered and of the way by means of which it has been modeled and implemented.

After a short description of its main characteristics, exactly as done in the previous chapter 3, the hypotheses assumed to build up the model, with the relative equations, and the procedures used to implement it are reported.

Also this time, this part has been realized by means of *COMSOL Multiphysics* code.

4.2.1 The physical system

During this last part of the work, the physical system illustrated on Figure 4.1 has been considered.

It is formed by two identical cylindrical channels characterized by:

- a diameter D, equal to 0.0124 m;

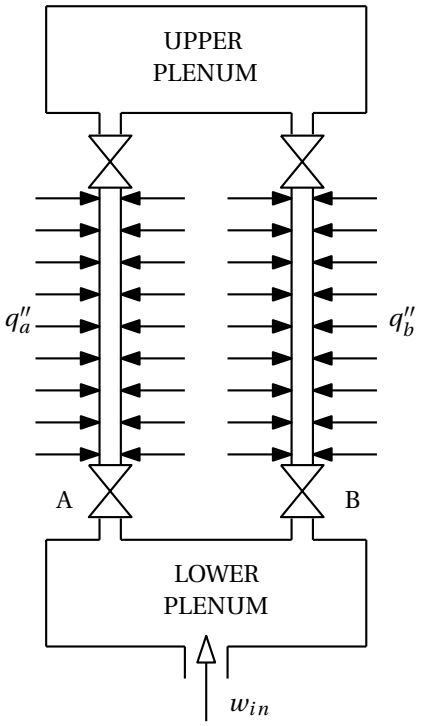

Figure 4.1: Sketch of the parallel channel model.

- a length L, equal to 3.6576 m (i.e. 12 ft);
- a slope angle θ, equal to 90°.

Both these channels are provided with an inlet and an outlet orifice: their function is to introduce, thanks to sharp variation of the channel cross sections, appropriate local pressure drops thus to regulate the mass flow rate flowing through them.

Lower plenum and an upper plenum allow to impose the same pressure drop across the two channels. In particular, for the first one a value of 7.0 MPa has been fixed for the inlet pressure p_{in} and a temperature T_{in} of about 250 °C (i.e. an inlet enthalpy h_{in} of 1100 kJ kg^{-1}).

Moreover, both the channels are subject to constant heat fluxes: more precisely, a certain quantity of thermal power is imposed on their wall and heats the water. The same characteristics taken into account for the wall in chapter 3 have been hereby chosen: a thickness t_w of 1 mm, a density ρ_w of 8000 kg m^{-3} and a specific heat c_w of 475 J kg^{-1} K^{-1}.

Note that the reason leading to the choice of all those values are the same one of chapter 3: they are close to the ones typical of a BWR environment.

4.2.2 The mathematical model

Both for the fluid dynamics and for the thermal behavior of the channel wall, the same models used in chapter 3 have been here adopted.

More precisely, for the first one, conservation equations (2.5), (3.4), (3.12) and constitutive and closure ones shown in sections 2.2.4 and 2.2.5 have been used.

Instead, for the second one equation (3.9) has been considered.

The only difference is represented by the boundary conditions: indeed, the parallel channel condition requires the imposition of coupled Dirichlet boundary conditions both at the inlet and at the outlet of the channel [1], that is at the two plena.

The conditions fixed at the lower plenum are represented by the inlet pressure and temperature (enthalpy), together with an ideal mass balance. Indeed, the mass flow rate in each channel is not known: only the total inlet mass flow rate w_{in} is specified. Therefore, assuming the lower plenum as a point region:

$$w_{in} = w_a + w_b \tag{4.1}$$

which means:

$$G_{in}\, A_{in} = G_a\, A_a + G_b\, A_b \tag{4.2}$$

The cross sectional areas A_{in}, A_a and A_b have been assumed to be equal for simplicity, so that condition (4.1) is the same of the following:

$$G_{in} = G_a + G_b \tag{4.3}$$

With regards to the upper plenum instead, the condition imposed is simply:

$$p_a(L) = p_b(L) \tag{4.4}$$

Although the condition is valid also at the lower plenum, that is $z = 0$, in the case of the upper plenum it is not fixed to a known value as it happens to the upper plenum.

4.2.3 Model implementation

As mentioned above, the implementation of the model created has been done by means of *COMSOL Multiphysics* code.

Three steps led to accomplish this aim:

- at first, two one dimensional geometries characterized by the described features, one for each channel, have been created;
- secondly, all the equations mentioned have been implemented using the *PDE General Form* module as explained in chapter 2 and 3;
- finally, appropriate initial and boundary conditions have been imposed.

In particular, some explanations on the procedure used to implement the Dirichlet boundary conditions required are reported.

The conditions fixed at the inlet of the two channels are:

$$\begin{cases} \text{Channel A (}\textit{Dirichlet}\text{):} \\ R_1 = p_{in} - u_1 \\ R_2 = (G_{in} - G_b) - u_2 \\ R_3 = h_{in} - u_3 \end{cases} \qquad \begin{cases} \text{Channel B (}\textit{Dirichlet}\text{):} \\ R_1 = p_{in} - u_1 \\ R_2 = (G_{in} - G_a) - u_2 \\ R_3 = h_{in} - u_3 \end{cases} \tag{4.5}$$

The boundary conditions at the channel exits have been fixed instead in a slight different way. A mathematical condition able to connect the channels in terms of outlet pressure can be implemented in COMSOL as follow[1]:

$$\begin{cases} \text{Channel A (}\textit{Neumann}\text{):} \\ G_1 = -\Gamma_1(L) \\ G_2 = -\Gamma_2(L) \\ G_3 = -\Gamma_3(L) \end{cases} \qquad \begin{cases} \text{Channel B (}\textit{Dirichlet}\text{):} \\ R_1 = p_a - u_1 \\ R_2 = 0 \\ R_3 = 0 \end{cases} \tag{4.6}$$

Fixing the outlet pressure of channel B (Figure 4.1) to be the same computed at the outlet of channel A is enough to connect the two channels: this pressure is not, indeed, mathematically independent from the one of channel B.

The quantities G_a, G_b and p_a have been computed as *integrated coupling variables* and made available in the opportune points of the two geometries [2].

4.3 Performed simulations and results

In this section the calculations performed with this model are illustrated.

[1] cf. equation (2.54), chapter 2

This analysis, which has to be considered preliminary, consists in two steady calculations, calculation of the relative eigenvalues, and a transient calculation as well.

All the calculations have been performed by means of the same COMSOL settings (meshgrid points, element shapes, etc...) used in chapter 3.

4.3.1 Steady state calculations

The steady calculations have been done in two different situations. In the first one, channel A is subject to a thermal flux while channel B is kept adiabatic, all the others operating conditions being the same in both the two channels. In the second one all the operating conditions are the same, so the thermal power supplied to both the channels is identical.

The main parameters that determine the operating conditions of the system in the two cases are listed below:

- $p_{in} = 7.0\,\mathrm{MPa}$ and $h_{in} = 1100\,\mathrm{kJ\,kg^{-1}}$ (i.e. $T_{in} \cong 253\,^{\circ}\mathrm{C}$);
- $K^a_{in} = K^b_{in} = 20$ and $K^a_{out} = K^b_{out} = 5$;
- $\dot{m}_{in} = 0.604\,\mathrm{kg\,s^{-1}}$ i.e. $G_{in} = 5000\,\mathrm{kg\,m^{-2}\,s^{-1}}$;

The thermal power supply has been kept constant and uniform along the channel axis and in the first steady state calculated, steady state 1 from now on, only the channel A has been heated, whereas in the second one, steady state 2 from now on, both the channels have been heated by the same thermal power. In both the cases they are subjected to the same thermal flux of $200\,\mathrm{kW\,m^{-2}}$ that corresponds to a total power supply of about 28.5 kW per channel.

The main results of the steady simulation 1 are shown in Figure 4.2a, 4.2b and 4.2c, which show respectively pressure, temperature and velocity axial distributions.

The pressure variation along the channel are basically the same in the two channels, being the flow rates basically the same in the two channels and the velocities very similar because of the small density variation of the fluid in comparison to the two-phase cases of chapter 3.

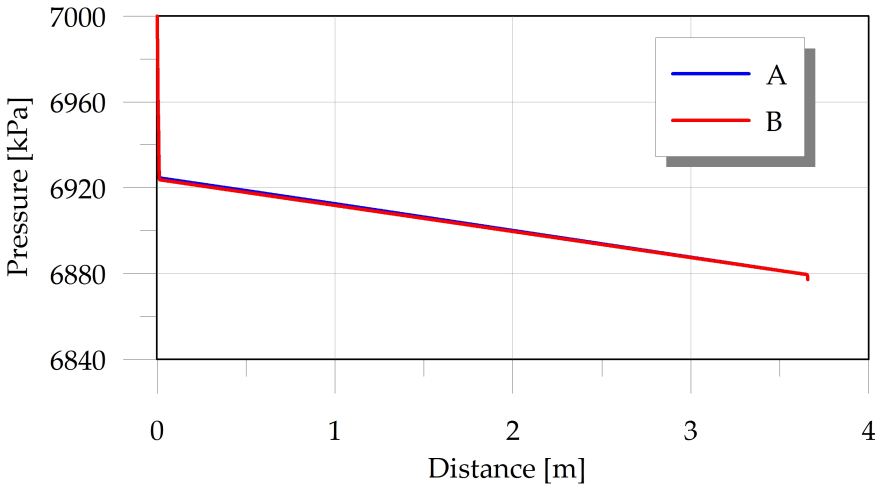

(a) Pressure.

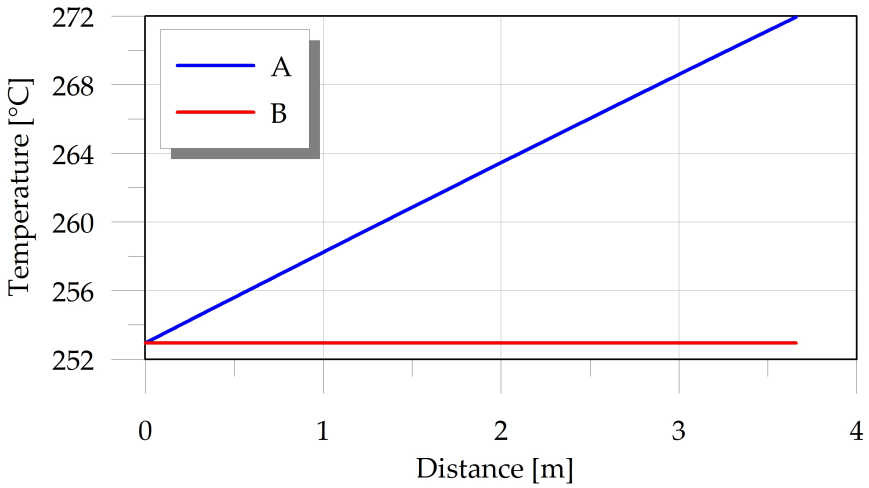

(b) Temperature.

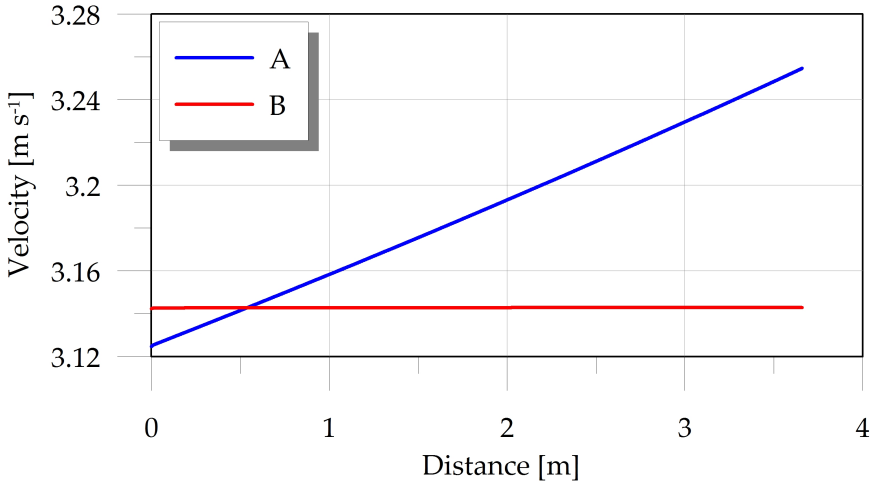

(c) Velocity.

Figure 4.2: Pressure, temperature and velocity distributions in the channels (Steady state 1).

Steady state 1	Steady state 2
3.618631	3.881947
4.433492	$4.428761 - 0.199202\,i$
$4.61708 - 0.293297\,i$	$4.428761 + 0.199202\,i$
$4.61708 + 0.293297\,i$	$4.592551 - 0.839974\,i$
4.702175	$4.592551 + 0.839974\,i$
$4.744256 - 0.828115\,i$	$4.712886 - 0.373348\,i$
$4.744256 + 0.828115\,i$	$4.712886 + 0.373348\,i$
$4.842309 - 0.348329\,i$	$4.901145 - 0.319712\,i$
$4.842309 + 0.348329\,i$	$4.901145 + 0.319712\,i$
$4.963431 - 0.271569\,i$	$4.977686 - 0.249632\,i$
$4.963431 + 0.271569\,i$	$4.977686 + 0.249632\,i$
4.978222	$4.981655 - 0.437316\,i$
$4.99681 - 0.413304\,i$	$4.981655 + 0.437316\,i$
$4.99681 + 0.413304\,i$	4.98721
$5.004777 - 0.210894\,i$	$5.011167 - 0.198549\,i$
$5.004777 + 0.210894\,i$	$5.011167 + 0.198549\,i$
$5.021233 - 0.173521\,i$	$5.026816 - 0.162468\,i$
$5.021233 + 0.173521\,i$	$5.026816 + 0.162468\,i$
$5.031602 - 0.150133\,i$	$5.028234 - 0.11679\,i$
$5.031602 + 0.150133\,i$	$5.028234 + 0.11679\,i$

Table 4.1: First twenty eigenvalues with the smaller real part.

The flow rates at the channel inlets are:

$$\begin{cases} \dot{m}_a \cong 0.301\,\mathrm{kg\,s^{-1}} & \text{i.e.} \quad G_a = 2493\,\mathrm{kg\,m^{-2}\,s^{-1}} \\ \dot{m}_b \cong 0.303\,\mathrm{kg\,s^{-1}} & \text{i.e.} \quad G_b = 2507\,\mathrm{kg\,m^{-2}\,s^{-1}} \end{cases}$$

which means that the total flow rate is divided into two practically equal fractions. The total pressure drop between the two plena is of 122.8 kPa.

The results of steady simulations 2 are shown instead in Figure 4.3 in which pressure, temperature and velocity distribution in each channel is reported. As expected, in this case all the quantities are equal in both the channels and the total pressure drop is of 123.3 kPa, i.e. basically the same of steady state 1.

Finally, the eigenvalues of the system linearized around these two equilibrium steady states have been computed in order to test the same methodology used for

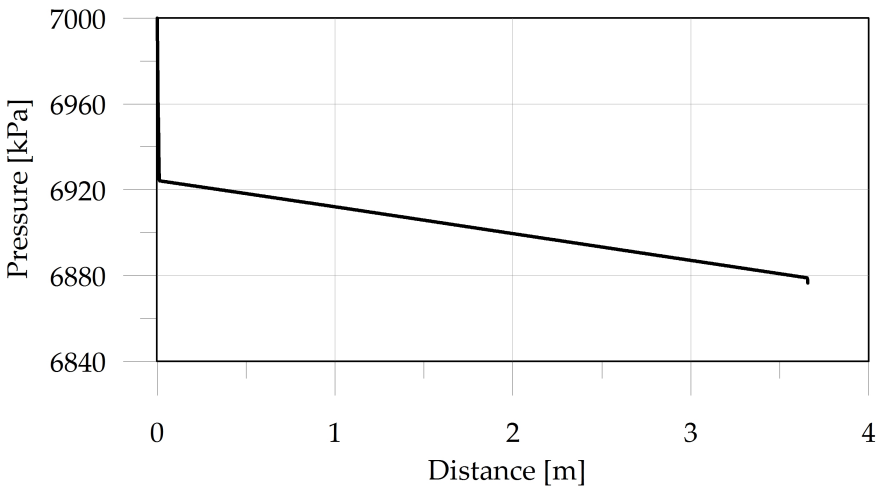

(a) Pressure.

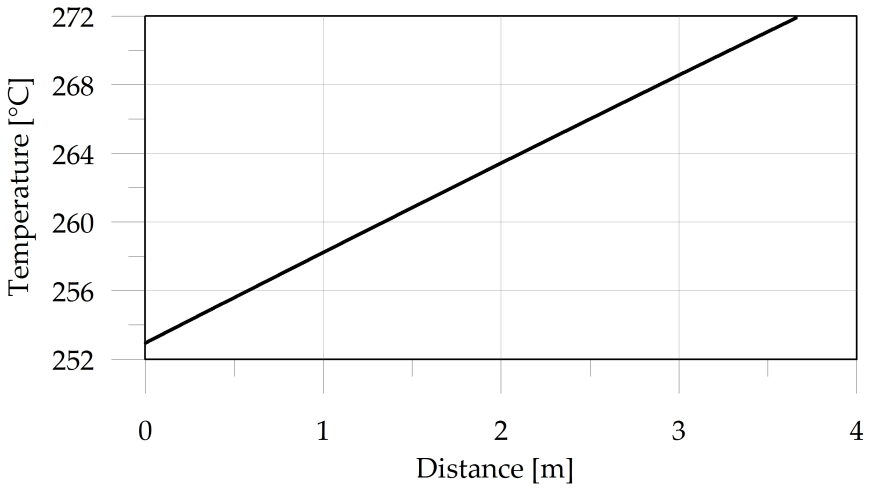

(b) Temperature.

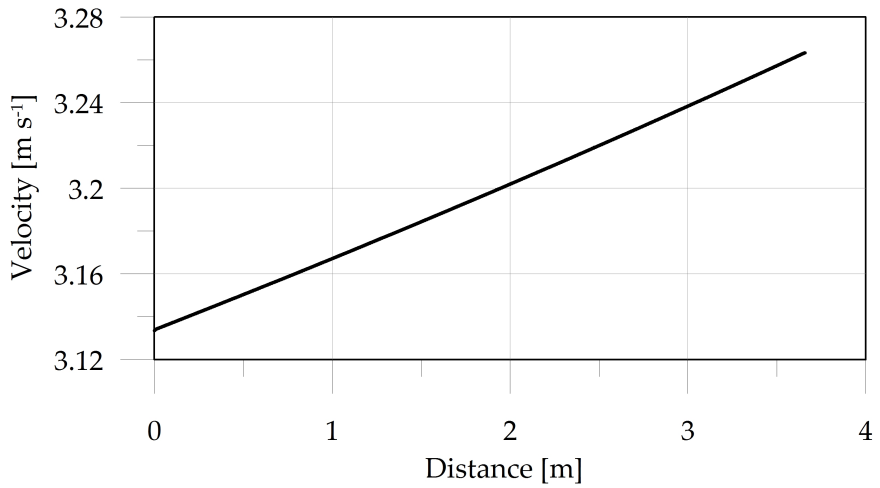

(c) Velocity.

Figure 4.3: Pressure, temperature and velocity distributions in the channels (Steady state 2).

the single boiling channel stability analysis of chapter 3. The first twenty smallest eigenvalues are reported in Table 4.1.

Obviously, according to the stability criterion illustrated in section 3.4, the system results linearly stable being a single-phase system: these ones, indeed, are not subject to the instability mechanisms illustrated in chapter 1.

4.3.2 Transient calculations

The transient calculations performed consisted in a time-dependent simulation of flow rate reduction in channel B, that is an increase of K_{in}^{b}.

This simulation is representative of an inlet throttling obtained by means of a valve partial closure operation. Practically, this closure has been simulated by increasing the parameter K_{in}^{b} from 20 to 40 in a lapse of time of 1 s.

Figure 4.4 shows the effect of the operation on the system pressure.

In particular, Figures 4.4a and 4.4b show the pressure distributions along the two channels at three different significant time steps: it can be noticed that the entire profiles translate toward smallest values very rapidly.

Figure 4.4c shows instead the total system pressure drop response to the operation. It can be noticed here that the system results are deeply affected by the valve throttling: the total pressure drop increases of almost the 25 %, that is, in this case, from 123.3 kPa to 152.7 kPa. Also in this plot, the rapid pressure dynamics can be observed.

Figure 4.5 shows instead the transient responses in terms of mass fluxes and of outlet temperatures in the channels. It can be noticed that the mass flux variation is the one desired as the mass flux in channel B decreases and the one in channel A increases (Figure 4.5a). As a consequence of the flow rate, and of the system overall, unbalance of outlet temperatures changes in order to respect the energy balance. This means that the outlet temperature in channel B increases in response to the mass flow rate reduction and, on the contrary, the outlet temperature in channel A decreases (Figure 4.5b). As a final consideration, the effect of the wall and of the slower dynamics of these quantities can be noticed in Figure 4.5b which shows a softer dynamics compared to the pressure one.

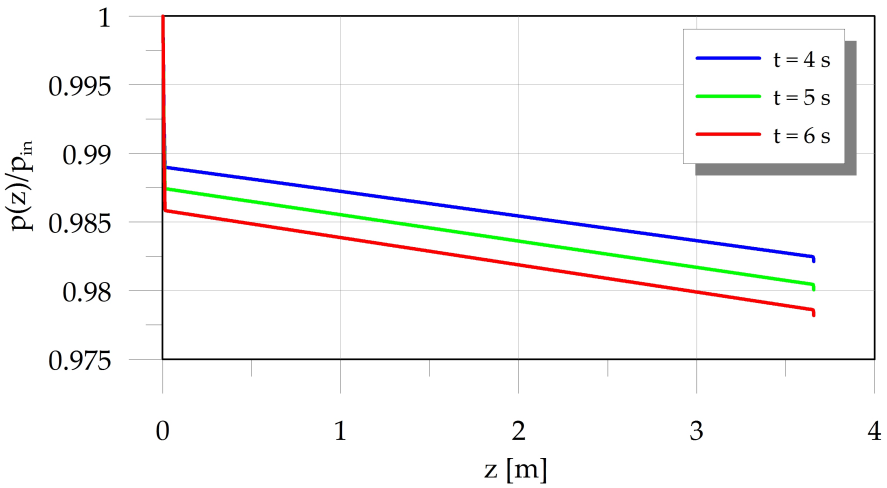

(a) Channel A.

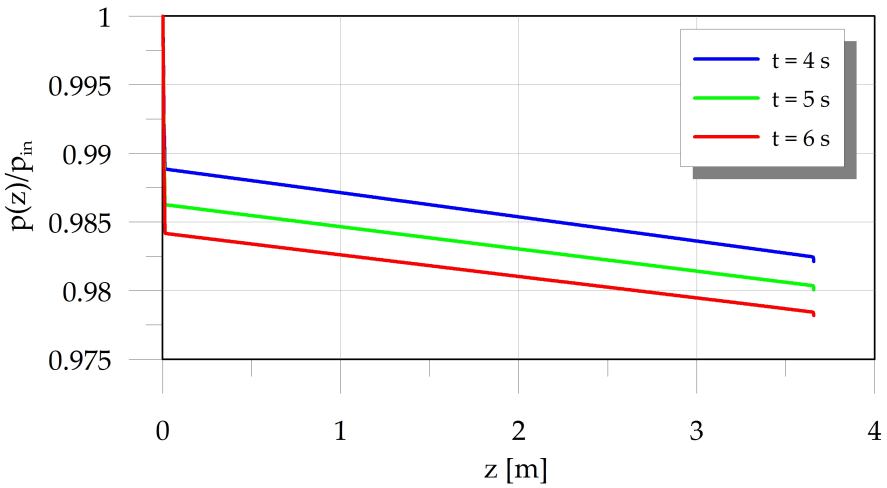

(b) Channel B.

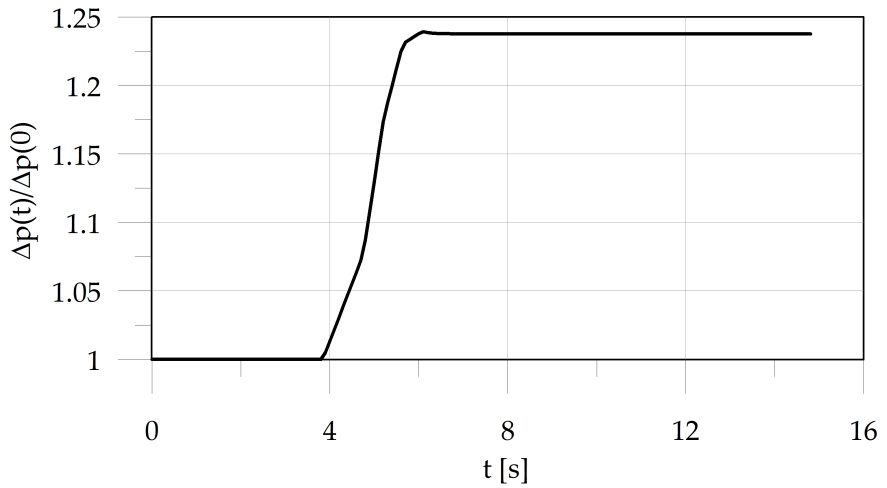

(c) Total system pressure drop.

Figure 4.4: Pressure variations.

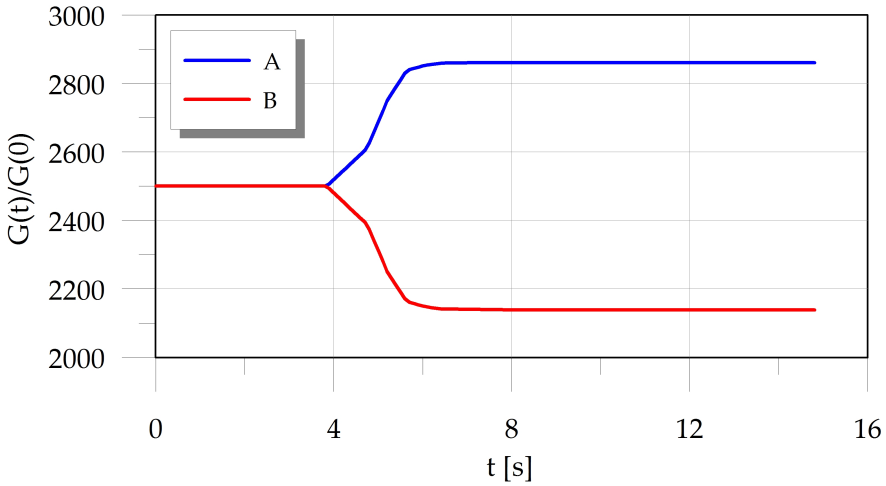

(a) Mass fluxes.

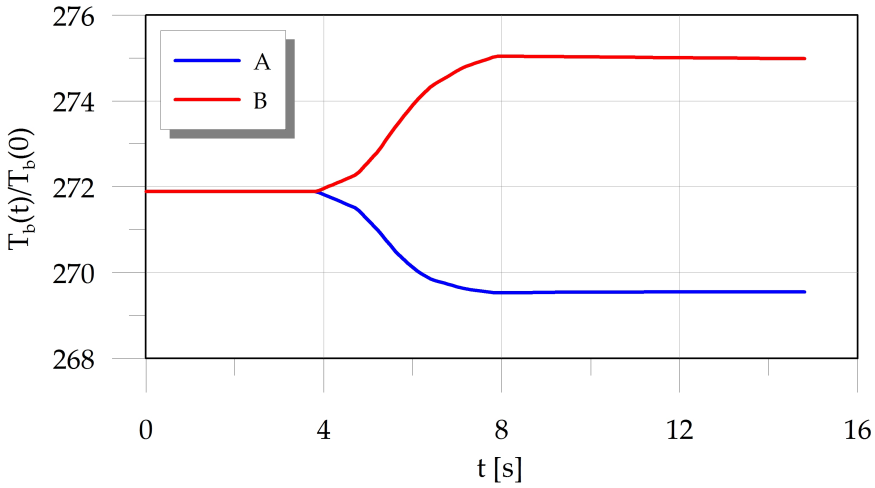

(b) Outlet temperatures.

Figure 4.5: Mass flux and temperature variations.

4.4 Conclusions

Although the obtained results are just preliminary, it seems that the created model could be used to the aim for which it has been ideated.

The results of the two steady state calculations and the computation of the eigenvalues of the linearized model have shown that the same approach of chapter 3 to the stability analysis could be applied to parallel channel systems too. Obviously, in the single-phase conditions examined, the system results linearly stable and this fact has been confirmed by the obtained eigenvalues: in a future development of this work a two-phase twin and multiple parallel channel system could be analyzed systemati-

cally by means of this technique.

Finally, a transient simulation has shown the effect of a flow rate reduction in one of the channels by means of throttling valve partial closure. This operation created an unbalance in the system which increases its total pressure drop. Flow rates and thermal outlet temperatures are redistributed in a controlled way, as it is desirable in PWR systems. Once more, this transient evidences again the model reliability.

Bibliography

[1] J.L. Muñoz-Cobo, M.Z. Podowski, and S. Chiva. Parallel channel instabilities in boiling water reactor systems: boundary conditions for out of phase oscillations. *Annals of Nuclear Energy*, 2002.

[2] *COMSOL Multiphysics 3.5a User's Guide*.

Conclusions

The model built for the description and the simulation of the thermal fluid dynamics of water and of mixtures of steam and water revealed a good reliability: the validation procedure, mainly based on steady state calculations, showed an accordance with the experimental data characterized by a maximum error of 10%. This fact suggested that the hypotheses made and the use of the *Thermal Equilibrium Drift Flux Model* to describe the two-phase flow dynamics can be considered satisfying for the purposes of the work.

The single channel analysis has been made by using such a model, opportunely generalized by the introduction of a wall model and local pressure losses at the inlet and the outlet of the channel. The results are listed below.

- The steady state analysis allowed the comparison between HEM and drift flux model, and a static stability analysis based on the system characteristic curves; these ones have been computed for different values of the operating parameters. The obtained results are in good agreement with theoretical expectations and with the literature.

- The linear stability analysis, performed with a particular eigenvalue technique based on COMSOL eigenvalue solver, allowed the drawing of stability maps of the system by using different two-phase flow mixture models (i.e. HEM and drift flux model) and with different values of inlet and outlet throttling. The results have shown a good agreement with both the results obtained by Ambrosini et al. and with the theoretical expectations.

- The transient calculations evidence the effect of the wall on the system response to thermal power supply step both in case of stability and of instability. In the

first case the damping effect of the wall on the system responses has been observed, in the second one density wave oscillations appeared and, in the case of wall absence, diverging oscillations have been found, probably numerically triggered. Anyway, the system behavior with the wall seems to be much more physically sensitive than the one shown without the wall.

In the last part of the work, the model for the single channel has been used to build a parallel channel system, made by two channels, thanks to opportune specification of the boundary conditions. The preliminary analysis performed showed mainly the possibility of an analysis similar to the single channel one.

In a future development of this work the systematic linear stability analysis in boiling conditions could be done. Beside it, being now the model for a single channel available, more channels could be easily added and then also multi-channel systems could be analyzed.

Furthermore, after the linear stability analysis, the non-linear one could be done: transient calculations could be performed to find the so-called limit cycle and so the stability boundary.

Finally, with regards to a possible model improvement, the heat transfer between wall and fluid could be better specified by means of more accurate relations for the heat transfer coefficient definitions.

Appendix A

Mathematical model used in chapter 2

A.1 Conservation equations

$$\frac{\partial \rho_m}{\partial t} + \frac{\partial G}{\partial z} = 0 \tag{A.1}$$

$$\frac{\partial G}{\partial t} + \frac{\partial}{\partial z}\left(\frac{G^2}{\rho_m^+}\right) = -\frac{dp}{dz} - \rho_m g \sin\theta - \left(\frac{\partial p}{\partial z}\right)_{\text{fric}} \tag{A.2}$$

$$\frac{\partial}{\partial t}\left(\rho_m h_m - p\right) + \frac{\partial}{\partial z}\left(G h_m^+\right) = q'' \frac{P}{A} + \frac{G}{\rho_m}\left[\left(\frac{\partial p}{\partial z}\right)_{\text{fric}} + \frac{\partial p}{\partial z}\right] \tag{A.3}$$

A.2 Constitutive equations

$$\rho_L = \begin{cases} \rho_L(p,h) & \text{if} \quad vc \le 0 \\ \rho_L(p) & \text{if} \quad 0 \le vc \le 1 \end{cases} \tag{A.4}$$

$$\rho_V = \begin{cases} \rho_V(p) & \text{if} \quad 0 \le vc \le 1 \\ \rho_V(p,h) & \text{if} \quad vc \ge 1 \end{cases} \tag{A.5}$$

$$h_L = h_L(p) \quad \text{if} \quad 0 \le vc \le 1 \tag{A.6}$$

$$h_V = h_V(p) \quad \text{if} \quad 0 \le vc \le 1 \tag{A.7}$$

$$\mu_L = \begin{cases} \mu_L(p,h) & \text{if} \quad vc \le 0 \\ \mu_L(p) & \text{if} \quad 0 \le vc \le 1 \end{cases} \tag{A.8}$$

$$\mu_V = \begin{cases} \mu_V(p) & \text{if} \quad 0 \le vc \le 1 \\ \mu_V(p,h) & \text{if} \quad vc \ge 1 \end{cases} \tag{A.9}$$

$$\sigma = \sigma(p) \quad \text{if} \quad 0 \le vc \le 1 \tag{A.10}$$

A.3 Closure equations

$$\rho_m = \begin{cases} \rho_m^+ = \rho_L & \text{if} \quad vc \le 0 \\ \alpha\,\rho_L + (1-\alpha)\,\rho_V & \text{if} \quad 0 \le vc \le 1 \\ \rho_m^+ = \rho_V & \text{if} \quad vc \ge 1 \end{cases} \tag{A.11}$$

$$\rho_m^+ = \begin{cases} \rho_m = \rho_L & \text{if} \quad vc \le 0 \\ \left[\dfrac{x^2}{\alpha\,\rho_V} + \dfrac{(1-x)^2}{(1-\alpha)\,\rho_L}\right]^{-1} & \text{if} \quad 0 \le vc \le 1 \\ \rho_m = \rho_V & \text{if} \quad vc \ge 1 \end{cases} \tag{A.12}$$

$$h_m = \begin{cases} h_m^+ = h_L & \text{if} \quad vc \le 0 \\ \dfrac{\alpha\,\rho_V\,h_L + (1-\alpha)\,\rho_L\,h_L}{\rho_m} & \text{if} \quad 0 \le vc \le 1 \\ h_m^+ = h_V & \text{if} \quad vc \ge 1 \end{cases} \tag{A.13}$$

$$\left(\frac{\partial p}{\partial z}\right)_{\text{fric}} = \begin{cases} f_M \dfrac{G^2}{2\,\rho_L\,D} & \text{if} \quad vc \le 0 \\ \phi_{lo}^2\,f_{lo}\dfrac{G^2}{2\,\rho_L\,D} & \text{if} \quad 0 \le vc \le 1 \\ f_M \dfrac{G^2}{2\,\rho_V\,D} & \text{if} \quad vc \ge 1 \end{cases} \tag{A.14}$$

$$f_M = \begin{cases} 0.316 \cdot \text{Re}^{-0.25} & \text{if} \quad \text{Re} < 30\,000 \\ 0.184 \cdot \text{Re}^{-0.2} & \text{if} \quad 30\,000 < \text{Re} < 1\,000\,000 \end{cases} \tag{A.15}$$

$$f_{lo} = \begin{cases} 0.316 \cdot \text{Re}_{lo}^{-0.25} & \text{if} \quad \text{Re} < 30\,000 \\ 0.184 \cdot \text{Re}_{lo}^{-0.2} & \text{if} \quad 30\,000 < \text{Re} < 1\,000\,000 \end{cases} \tag{A.16}$$

$$\text{Re} = \text{Re}_{lo} = \frac{G\,D}{A\,\mu} \tag{A.17}$$

$$\alpha = \begin{cases} 0 & \text{if} \quad vc \le 0 \\ \left[1 + \dfrac{1-x}{x}\dfrac{\rho_V}{\rho_L}S\right]^{-1} & \text{if} \quad 0 \le vc \le 1 \\ 1 & \text{if} \quad vc \ge 1 \end{cases} \tag{A.18}$$

$$\beta = \begin{cases} 0 & \text{if} \quad vc \le 0 \\ \left[1 + \dfrac{1-x}{x}\dfrac{\rho_V}{\rho_L}\right]^{-1} & \text{if} \quad 0 \le vc \le 1 \\ 1 & \text{if} \quad vc \ge 1 \end{cases} \tag{A.19}$$

$$x = \begin{cases} 0 & \text{if} \quad vc \le 0 \\ \dfrac{h_m^+ - h_L}{h_V - h_L} & \text{if} \quad 0 \le vc \le 1 \\ 1 & \text{if} \quad vc \ge 1 \end{cases} \tag{A.20}$$

$$S = C_0 + \frac{(C_0 - 1)\, x\, \rho_L}{(1-x)\, \rho_V} + \frac{V_{vj}\, \rho_L}{(1-x)\, G} \tag{A.21}$$

$$C_0 = \beta \left[1 + \left(\frac{1}{\beta} - 1\right)^b\right] \tag{A.22}$$

$$b = \left(\frac{\rho_V}{\rho_L}\right)^{0.1} \tag{A.23}$$

$$V_{vj} = 0 \tag{A.24}$$

$$\phi_{lo}^2 = 0.2185\, E + \frac{0.2365\, F\, H}{\mathrm{Fr}^{-0.0165}\, \mathrm{We}^{-0.1318}} \tag{A.25}$$

$$E = (1-x)^2 + x^2 \frac{\rho_L f_{vo}}{\rho_V f_{lo}}$$

$$F = x^{0.78} (1-x)^{0.224}$$

$$H = \left(\frac{\rho_L}{\rho_V}\right)^{0.91} \left(\frac{\mu_V}{\mu_L}\right)^{0.19} \left(1 - \frac{\mu_V}{\mu_L}\right)^{0.7}$$

$$\mathrm{Fr} = \frac{G^2}{g\, D\, (\rho_m^+)^2}$$

$$\mathrm{We} = \frac{G^2\, D}{\sigma\, \rho_m^+}$$

A.4 Initial conditions

$$p(z,0) = p_{in} \tag{A.26}$$

$$G(z,0) = G_{in} \tag{A.27}$$

$$h_m^+(z,0) = h_{in} \tag{A.28}$$

A.5 Boundary conditions

$$p(0,t) = p_{in} \tag{A.29}$$

$$G(0,t) = G_{in} \tag{A.30}$$

$$h_m^+(0,t) = h_{in} \tag{A.31}$$

Appendix B

Mathematical models used in chapter 3

B.1 Mixture equations

$$\frac{\partial \rho_m}{\partial t} + \frac{\partial G}{\partial z} = 0 \tag{B.1}$$

$$\frac{\partial G}{\partial t} + \frac{\partial}{\partial z}\left(\frac{G^2}{\rho_m^+}\right) = -\frac{\partial p}{\partial z} - \rho_m g \sin\theta - \left(\frac{\partial p}{\partial z}\right)_{\text{fric}} - \sum_{j=in}^{out}\left(\frac{\partial p}{\partial z}\right)_{\text{conc},j} \tag{B.2}$$

$$\frac{\partial}{\partial t}\left(\rho_m h_m - p\right) + \frac{\partial}{\partial z}\left(G h_m^+\right) = \frac{U_{ex} P \left(T_w - T_b\right)}{A} + \frac{G}{\rho_m}\left[\left(\frac{\partial p}{\partial z}\right)_{\text{fric}} + \sum_{j=in}^{out}\left(\frac{\partial p}{\partial z}\right)_{\text{conc},j} + \frac{\partial p}{\partial z}\right] \tag{B.3}$$

B.2 Wall equation

$$M_w c_w \frac{\partial T_w}{\partial t} = q'' P L - U_{ex} P L \left(T_w - T_b\right) \tag{B.4}$$

B.3 Constitutive equations

$$\rho_L = \begin{cases} \rho_L(p,h) & \text{if} \quad vc \le 0 \\ \rho_L(p) & \text{if} \quad 0 \le vc \le 1 \end{cases} \tag{B.5}$$

$$\rho_V = \begin{cases} \rho_V(p) & \text{if} \quad 0 \le vc \le 1 \\ \rho_V(p,h) & \text{if} \quad vc \ge 1 \end{cases} \tag{B.6}$$

$$h_L = h_L(p) \quad \text{if} \quad 0 \le vc \le 1 \tag{B.7}$$

$$h_V = h_V(p) \quad \text{if} \quad 0 \le vc \le 1 \tag{B.8}$$

$$\mu_L = \begin{cases} \mu_L(p,h) & \text{if} \quad vc \le 0 \\ \mu_L(p) & \text{if} \quad 0 \le vc \le 1 \end{cases} \tag{B.9}$$

$$\mu_V = \begin{cases} \mu_V(p) & \text{if} \quad 0 \le vc \le 1 \\ \mu_V(p,h) & \text{if} \quad vc \ge 1 \end{cases} \tag{B.10}$$

$$\sigma = \sigma(p) \quad \text{if} \quad 0 \le vc \le 1 \tag{B.11}$$

B.4 Closure equations

B.4.1 Homogeneous model (HEM)

$$\rho_m = \begin{cases} \rho_m^+ = \rho_L & \text{if} \quad vc \le 0 \\ \alpha\,\rho_L + (1-\alpha)\,\rho_V & \text{if} \quad 0 \le vc \le 1 \\ \rho_m^+ = \rho_V & \text{if} \quad vc \ge 1 \end{cases} \tag{B.12}$$

$$\rho_m^+ = \begin{cases} \rho_m = \rho_L & \text{if} \quad vc \le 0 \\ \left[\dfrac{x^2}{\alpha\,\rho_V} + \dfrac{(1-x)^2}{(1-\alpha)\,\rho_L}\right]^{-1} & \text{if} \quad 0 \le vc \le 1 \\ \rho_m = \rho_V & \text{if} \quad vc \ge 1 \end{cases} \tag{B.13}$$

$$h_m = \begin{cases} h_m^+ = h_L & \text{if} \quad vc \le 0 \\ \dfrac{\alpha\,\rho_V\,h_L + (1-\alpha)\,\rho_L\,h_L}{\rho_m} & \text{if} \quad 0 \le vc \le 1 \\ h_m^+ = h_V & \text{if} \quad vc \ge 1 \end{cases} \tag{B.14}$$

$$\left(\frac{\partial p}{\partial z}\right)_{\text{fric}} = \begin{cases} f_M \dfrac{G^2}{2\,\rho_L\,D} & \text{if} \quad vc \le 0 \\ \phi_{lo}^2\,f_{lo}\dfrac{G^2}{2\,\rho_L\,D} & \text{if} \quad 0 \le vc \le 1 \\ f_M \dfrac{G^2}{2\,\rho_V\,D} & \text{if} \quad vc \ge 1 \end{cases} \tag{B.15}$$

$$\left(\frac{\partial p}{\partial z}\right)_{\text{conc},j} = \begin{cases} K_j \dfrac{G^2}{2\,\rho_L}\,\delta\left(z - z_j\right) & \text{if} \quad vc \le 0 \\ K_j\,\phi_{lo}^2 \dfrac{G^2}{2\,\rho_L}\,\delta\left(z - z_j\right) & \text{if} \quad 0 \le vc \le 1 \\ K_j \dfrac{G^2}{2\,\rho_V}\,\delta\left(z - z_j\right) & \text{if} \quad vc \ge 1 \end{cases} \tag{B.16}$$

$$f_M = \begin{cases} 0.316 \cdot \mathrm{Re}^{-0.25} & \text{if} \quad \mathrm{Re} < 30\,000 \\ 0.184 \cdot \mathrm{Re}^{-0.2} & \text{if} \quad 30\,000 < \mathrm{Re} < 1\,000\,000 \end{cases} \tag{B.17}$$

$$f_{lo} = \begin{cases} 0.316 \cdot \mathrm{Re}_{lo}^{-0.25} & \text{if} \quad \mathrm{Re} < 30\,000 \\ 0.184 \cdot \mathrm{Re}_{lo}^{-0.2} & \text{if} \quad 30\,000 < \mathrm{Re} < 1\,000\,000 \end{cases} \tag{B.18}$$

$$\mathrm{Re} = \mathrm{Re}_{lo} = \frac{G D}{A \mu} \tag{B.19}$$

$$\alpha = \begin{cases} 0 & \text{if} \quad vc \le 0 \\ \left[1 + \dfrac{1-x}{x} \dfrac{\rho_V}{\rho_L} S\right]^{-1} & \text{if} \quad 0 \le vc \le 1 \\ 1 & \text{if} \quad vc \ge 1 \end{cases} \tag{B.20}$$

$$\beta = \begin{cases} 0 & \text{if} \quad vc \le 0 \\ \left[1 + \dfrac{1-x}{x} \dfrac{\rho_V}{\rho_L}\right]^{-1} & \text{if} \quad 0 \le vc \le 1 \\ 1 & \text{if} \quad vc \ge 1 \end{cases} \tag{B.21}$$

$$x = \begin{cases} 0 & \text{if} \quad vc \le 0 \\ \dfrac{h_m^+ - h_L}{h_V - h_L} & \text{if} \quad 0 \le vc \le 1 \\ 1 & \text{if} \quad vc \ge 1 \end{cases} \tag{B.22}$$

$$S = C_0 + \frac{(C_0 - 1)\, x\, \rho_L}{(1-x)\, \rho_V} + \frac{V_{vj}\, \rho_L}{(1-x)\, G} \tag{B.23}$$

$$C_0 = 1.0 \tag{B.24}$$

$$V_{vj} = 0 \tag{B.25}$$

$$\phi_{lo}^2 = 1 + x \left(\frac{\rho_L}{\rho_V} - 1\right) \tag{B.26}$$

B.4.2 Drift flux model A

$$\rho_m = \begin{cases} \rho_m^+ = \rho_L & \text{if} \quad vc \le 0 \\ \alpha\, \rho_L + (1-\alpha)\, \rho_V & \text{if} \quad 0 \le vc \le 1 \\ \rho_m^+ = \rho_V & \text{if} \quad vc \ge 1 \end{cases} \tag{B.27}$$

$$\rho_m^+ = \begin{cases} \rho_m = \rho_L & \text{if} \quad vc \le 0 \\ \left[\dfrac{x^2}{\alpha\, \rho_V} + \dfrac{(1-x)^2}{(1-\alpha)\, \rho_L}\right]^{-1} & \text{if} \quad 0 \le vc \le 1 \\ \rho_m = \rho_V & \text{if} \quad vc \ge 1 \end{cases} \tag{B.28}$$

$$h_m = \begin{cases} h_m^+ = h_L & \text{if} \quad vc \le 0 \\ \dfrac{\alpha\,\rho_V\,h_L + (1-\alpha)\,\rho_L\,h_L}{\rho_m} & \text{if} \quad 0 \le vc \le 1 \\ h_m^+ = h_V & \text{if} \quad vc \ge 1 \end{cases} \tag{B.29}$$

$$\left(\frac{\partial p}{\partial z}\right)_{\text{fric}} = \begin{cases} f_M \dfrac{G^2}{2\,\rho_L\,D} & \text{if} \quad vc \le 0 \\ \phi_{lo}^2\, f_{lo} \dfrac{G^2}{2\,\rho_L\,D} & \text{if} \quad 0 \le vc \le 1 \\ f_M \dfrac{G^2}{2\,\rho_V\,D} & \text{if} \quad vc \ge 1 \end{cases} \tag{B.30}$$

$$\left(\frac{\partial p}{\partial z}\right)_{\text{conc},j} = \begin{cases} K_j \dfrac{G^2}{2\,\rho_L}\,\delta\left(z - z_j\right) & \text{if} \quad vc \le 0 \\ K_j\,\phi_{lo}^2 \dfrac{G^2}{2\,\rho_L}\,\delta\left(z - z_j\right) & \text{if} \quad 0 \le vc \le 1 \\ K_j \dfrac{G^2}{2\,\rho_V}\,\delta\left(z - z_j\right) & \text{if} \quad vc \ge 1 \end{cases} \tag{B.31}$$

$$f_M = \begin{cases} 0.316 \cdot \text{Re}^{-0.25} & \text{if} \quad \text{Re} < 30\,000 \\ 0.184 \cdot \text{Re}^{-0.2} & \text{if} \quad 30\,000 < \text{Re} < 1\,000\,000 \end{cases} \tag{B.32}$$

$$f_{lo} = \begin{cases} 0.316 \cdot \text{Re}_{lo}^{-0.25} & \text{if} \quad \text{Re} < 30\,000 \\ 0.184 \cdot \text{Re}_{lo}^{-0.2} & \text{if} \quad 30\,000 < \text{Re} < 1\,000\,000 \end{cases} \tag{B.33}$$

$$\text{Re} = \text{Re}_{lo} = \frac{G\,D}{A\,\mu} \tag{B.34}$$

$$\alpha = \begin{cases} 0 & \text{if} \quad vc \le 0 \\ \left[1 + \dfrac{1-x}{x}\,\dfrac{\rho_V}{\rho_L}\,S\right]^{-1} & \text{if} \quad 0 \le vc \le 1 \\ 1 & \text{if} \quad vc \ge 1 \end{cases} \tag{B.35}$$

$$\beta = \begin{cases} 0 & \text{if} \quad vc \le 0 \\ \left[1 + \dfrac{1-x}{x}\,\dfrac{\rho_V}{\rho_L}\right]^{-1} & \text{if} \quad 0 \le vc \le 1 \\ 1 & \text{if} \quad vc \ge 1 \end{cases} \tag{B.36}$$

$$x = \begin{cases} 0 & \text{if} \quad vc \le 0 \\ \dfrac{h_m^+ - h_L}{h_V - h_L} & \text{if} \quad 0 \le vc \le 1 \\ 1 & \text{if} \quad vc \ge 1 \end{cases} \tag{B.37}$$

$$S = C_0 + \frac{(C_0 - 1)\,x\,\rho_L}{(1-x)\,\rho_V} + \frac{V_{vj}\,\rho_L}{(1-x)\,G} \tag{B.38}$$

$$C_0 = \beta \left[1 + \left(\frac{1}{\beta} - 1 \right)^b \right] \tag{B.39}$$

$$b = \left(\frac{\rho_V}{\rho_L} \right)^{0.1} \tag{B.40}$$

$$V_{vj} = 2.9 \left[\frac{\sigma\, g\, (\rho_L - \rho_V)}{\rho_L^2} \right]^{0.25} \tag{B.41}$$

(= 0 for steady curves and transient calculations)

$$\phi_{lo}^2 = \Omega(p, G) \left[1.2 \left(\frac{\rho_L}{\rho_V} - 1 \right) x^{0.824} \right] + 1.0 \tag{B.42}$$

B.4.3 Drift flux model B

$$\rho_m = \begin{cases} \rho_m^+ = \rho_L & \text{if} \quad vc \le 0 \\ \alpha\, \rho_L + (1-\alpha)\, \rho_V & \text{if} \quad 0 \le vc \le 1 \\ \rho_m^+ = \rho_V & \text{if} \quad vc \ge 1 \end{cases} \tag{B.43}$$

$$\rho_m^+ = \begin{cases} \rho_m = \rho_L & \text{if} \quad vc \le 0 \\ \left[\dfrac{x^2}{\alpha\, \rho_V} + \dfrac{(1-x)^2}{(1-\alpha)\, \rho_L} \right]^{-1} & \text{if} \quad 0 \le vc \le 1 \\ \rho_m = \rho_V & \text{if} \quad vc \ge 1 \end{cases} \tag{B.44}$$

$$h_m = \begin{cases} h_m^+ = h_L & \text{if} \quad vc \le 0 \\ \dfrac{\alpha\, \rho_V\, h_L + (1-\alpha)\, \rho_L\, h_L}{\rho_m} & \text{if} \quad 0 \le vc \le 1 \\ h_m^+ = h_V & \text{if} \quad vc \ge 1 \end{cases} \tag{B.45}$$

$$\left(\frac{\partial p}{\partial z} \right)_{\text{fric}} = \begin{cases} f_M \dfrac{G^2}{2\, \rho_L\, D} & \text{if} \quad vc \le 0 \\ \phi_{lo}^2\, f_{lo} \dfrac{G^2}{2\, \rho_L\, D} & \text{if} \quad 0 \le vc \le 1 \\ f_M \dfrac{G^2}{2\, \rho_V\, D} & \text{if} \quad vc \ge 1 \end{cases} \tag{B.46}$$

$$\left(\frac{\partial p}{\partial z} \right)_{\text{conc},j} = \begin{cases} K_j \dfrac{G^2}{2\, \rho_L}\, \delta\left(z - z_j\right) & \text{if} \quad vc \le 0 \\ K_j\, \phi_{lo}^2 \dfrac{G^2}{2\, \rho_L}\, \delta\left(z - z_j\right) & \text{if} \quad 0 \le vc \le 1 \\ K_j \dfrac{G^2}{2\, \rho_V}\, \delta\left(z - z_j\right) & \text{if} \quad vc \ge 1 \end{cases} \tag{B.47}$$

$$f_M = \begin{cases} 0.316 \cdot \mathrm{Re}^{-0.25} & \text{if} \quad \mathrm{Re} < 30\,000 \\ 0.184 \cdot \mathrm{Re}^{-0.2} & \text{if} \quad 30\,000 < \mathrm{Re} < 1\,000\,000 \end{cases} \tag{B.48}$$

$$f_{lo} = \begin{cases} 0.316 \cdot \mathrm{Re}_{lo}^{-0.25} & \text{if} \quad \mathrm{Re} < 30\,000 \\ 0.184 \cdot \mathrm{Re}_{lo}^{-0.2} & \text{if} \quad 30\,000 < \mathrm{Re} < 1\,000\,000 \end{cases} \tag{B.49}$$

$$\mathrm{Re} = \mathrm{Re}_{lo} = \frac{G D}{A \mu} \tag{B.50}$$

$$\alpha = \begin{cases} 0 & \text{if} \quad vc \le 0 \\ \left[1 + \dfrac{1-x}{x} \dfrac{\rho_V}{\rho_L} S\right]^{-1} & \text{if} \quad 0 \le vc \le 1 \\ 1 & \text{if} \quad vc \ge 1 \end{cases} \tag{B.51}$$

$$\beta = \begin{cases} 0 & \text{if} \quad vc \le 0 \\ \left[1 + \dfrac{1-x}{x} \dfrac{\rho_V}{\rho_L}\right]^{-1} & \text{if} \quad 0 \le vc \le 1 \\ 1 & \text{if} \quad vc \ge 1 \end{cases} \tag{B.52}$$

$$x = \begin{cases} 0 & \text{if} \quad vc \le 0 \\ \dfrac{h_m^+ - h_L}{h_V - h_L} & \text{if} \quad 0 \le vc \le 1 \\ 1 & \text{if} \quad vc \ge 1 \end{cases} \tag{B.53}$$

$$S = C_0 + \frac{(C_0 - 1)\, x\, \rho_L}{(1-x)\, \rho_V} + \frac{V_{vj}\, \rho_L}{(1-x)\, G} \tag{B.54}$$

$$C_0 = 1.13 \tag{B.55}$$

$$V_{vj} = 2.9 \left[\frac{\sigma\, g\, (\rho_L - \rho_V)}{\rho_L^2}\right]^{0.25} \tag{B.56}$$

(= 0 for steady curves and transient calculations)

$$\phi_{lo}^2 = \Omega(p, G) \left[1.2 \left(\frac{\rho_L}{\rho_V} - 1\right) x^{0.824}\right] + 1.0 \tag{B.57}$$

B.5 Initial conditions

$$p(z, 0) = p_{in} \tag{B.58}$$

$$G(z, 0) = G_{in} \tag{B.59}$$

$$h_m^+(z, 0) = h_{in} \tag{B.60}$$

$$T_w(z, 0) = T_{w0} \tag{B.61}$$

B.6 Boundary conditions

B.6.1 Imposed inlet flow rate

$$p(0,t) = p_{in} \tag{B.62}$$

$$G(0,t) = G_{in} \tag{B.63}$$

$$h_m^+(0,t) = h_{in} \tag{B.64}$$

B.6.2 Imposed pressure drop across

$$p(0,t) = p_{in} \tag{B.65}$$

$$h_m^+(0,t) = h_{in} \tag{B.66}$$

$$p(L,t) = p_{out} \tag{B.67}$$

Appendix C

Mathematical models used in chapter 4

All the equations listed below are valid both for channel A and B. Boundary conditions are instead different for the channels.

C.1 Mixture equations (valid both for channel A and B)

$$\frac{\partial \rho_m}{\partial t} + \frac{\partial G}{\partial z} = 0 \tag{C.1}$$

$$\frac{\partial G}{\partial t} + \frac{\partial}{\partial z}\left(\frac{G^2}{\rho_m^+}\right) = -\frac{\partial p}{\partial z} - \rho_m g \sin\theta - \left(\frac{\partial p}{\partial z}\right)_{\text{fric}} - \sum_{j=in}^{out}\left(\frac{\partial p}{\partial z}\right)_{\text{conc},j} \tag{C.2}$$

$$\frac{\partial}{\partial t}\left(\rho_m h_m - p\right) + \frac{\partial}{\partial z}\left(G h_m^+\right) = \frac{U_{ex} P \left(T_w - T_b\right)}{A} + \frac{G}{\rho_m}\left[\left(\frac{\partial p}{\partial z}\right)_{\text{fric}} + \sum_{j=in}^{out}\left(\frac{\partial p}{\partial z}\right)_{\text{conc},j} + \frac{\partial p}{\partial z}\right] \tag{C.3}$$

C.2 Wall equation

$$M_w c_w \frac{\partial T_w}{\partial t} = q'' P L - U_{ex} P L \left(T_w - T_b\right) \tag{C.4}$$

C.3 Constitutive equations (valid both for channel A and B)

$$\rho_L = \begin{cases} \rho_L(p,h) & \text{if} \quad vc \le 0 \\ \rho_L(p) & \text{if} \quad 0 \le vc \le 1 \end{cases} \tag{C.5}$$

$$\rho_V = \begin{cases} \rho_V(p) & \text{if} \quad 0 \le vc \le 1 \\ \rho_V(p,h) & \text{if} \quad vc \ge 1 \end{cases} \tag{C.6}$$

$$h_L = h_L(p) \quad \text{if} \quad 0 \le vc \le 1 \tag{C.7}$$

$$h_V = h_V(p) \quad \text{if} \quad 0 \le vc \le 1 \tag{C.8}$$

$$\mu_L = \begin{cases} \mu_L(p,h) & \text{if} \quad vc \le 0 \\ \mu_L(p) & \text{if} \quad 0 \le vc \le 1 \end{cases} \tag{C.9}$$

$$\mu_V = \begin{cases} \mu_V(p) & \text{if} \quad 0 \le vc \le 1 \\ \mu_V(p,h) & \text{if} \quad vc \ge 1 \end{cases} \tag{C.10}$$

$$\sigma = \sigma(p) \quad \text{if} \quad 0 \le vc \le 1 \tag{C.11}$$

C.4 Closure equations (valid both for channel A and B)

$$\rho_m = \begin{cases} \rho_m^+ = \rho_L & \text{if} \quad vc \le 0 \\ \alpha\,\rho_L + (1-\alpha)\,\rho_V & \text{if} \quad 0 \le vc \le 1 \\ \rho_m^+ = \rho_V & \text{if} \quad vc \ge 1 \end{cases} \tag{C.12}$$

$$\rho_m^+ = \begin{cases} \rho_m = \rho_L & \text{if} \quad vc \le 0 \\ \left[\dfrac{x^2}{\alpha\,\rho_V} + \dfrac{(1-x)^2}{(1-\alpha)\,\rho_L}\right]^{-1} & \text{if} \quad 0 \le vc \le 1 \\ \rho_m = \rho_V & \text{if} \quad vc \ge 1 \end{cases} \tag{C.13}$$

$$h_m = \begin{cases} h_m^+ = h_L & \text{if} \quad vc \le 0 \\ \dfrac{\alpha\,\rho_V\,h_L + (1-\alpha)\,\rho_L\,h_L}{\rho_m} & \text{if} \quad 0 \le vc \le 1 \\ h_m^+ = h_V & \text{if} \quad vc \ge 1 \end{cases} \tag{C.14}$$

$$\left(\frac{\partial p}{\partial z}\right)_{\text{fric}} = \begin{cases} f_M \dfrac{G^2}{2\rho_L D} & \text{if} \quad vc \le 0 \\ \phi_{lo}^2 f_{lo} \dfrac{G^2}{2\rho_L D} & \text{if} \quad 0 \le vc \le 1 \\ f_M \dfrac{G^2}{2\rho_V D} & \text{if} \quad vc \ge 1 \end{cases} \tag{C.15}$$

$$\left(\frac{\partial p}{\partial z}\right)_{\text{conc},j} = \begin{cases} K_j \dfrac{G^2}{2\rho_L} \delta\left(z - z_j\right) & \text{if} \quad vc \le 0 \\ K_j \phi_{lo}^2 \dfrac{G^2}{2\rho_L} \delta\left(z - z_j\right) & \text{if} \quad 0 \le vc \le 1 \\ K_j \dfrac{G^2}{2\rho_V} \delta\left(z - z_j\right) & \text{if} \quad vc \ge 1 \end{cases} \tag{C.16}$$

$$f_M = \begin{cases} 0.316 \cdot \text{Re}^{-0.25} & \text{if} \quad \text{Re} < 30\,000 \\ 0.184 \cdot \text{Re}^{-0.2} & \text{if} \quad 30\,000 < \text{Re} < 1\,000\,000 \end{cases} \tag{C.17}$$

$$f_{lo} = \begin{cases} 0.316 \cdot \text{Re}_{lo}^{-0.25} & \text{if} \quad \text{Re} < 30\,000 \\ 0.184 \cdot \text{Re}_{lo}^{-0.2} & \text{if} \quad 30\,000 < \text{Re} < 1\,000\,000 \end{cases} \tag{C.18}$$

$$\text{Re} = \text{Re}_{lo} = \frac{G D}{A \mu} \tag{C.19}$$

$$\alpha = \begin{cases} 0 & \text{if} \quad vc \le 0 \\ \left[1 + \dfrac{1-x}{x} \dfrac{\rho_V}{\rho_L} S\right]^{-1} & \text{if} \quad 0 \le vc \le 1 \\ 1 & \text{if} \quad vc \ge 1 \end{cases} \tag{C.20}$$

$$\beta = \begin{cases} 0 & \text{if} \quad vc \le 0 \\ \left[1 + \dfrac{1-x}{x} \dfrac{\rho_V}{\rho_L}\right]^{-1} & \text{if} \quad 0 \le vc \le 1 \\ 1 & \text{if} \quad vc \ge 1 \end{cases} \tag{C.21}$$

$$x = \begin{cases} 0 & \text{if} \quad vc \le 0 \\ \dfrac{h_m^+ - h_L}{h_V - h_L} & \text{if} \quad 0 \le vc \le 1 \\ 1 & \text{if} \quad vc \ge 1 \end{cases} \tag{C.22}$$

$$S = C_0 + \frac{(C_0 - 1)\, x\, \rho_L}{(1-x)\, \rho_V} + \frac{V_{vj}\, \rho_L}{(1-x)\, G} \tag{C.23}$$

$$C_0 = \beta \left[1 + \left(\frac{1}{\beta} - 1\right)^b\right] \tag{C.24}$$

$$b = \left(\frac{\rho_V}{\rho_L}\right)^{0.1} \tag{C.25}$$

$$V_{vj} = 2.9 \left[\frac{\sigma\, g\, (\rho_L - \rho_V)}{\rho_L^2} \right]^{0.25} \tag{C.26}$$

$$\phi_{lo}^2 = \Omega(p, G) \left[1.2 \left(\frac{\rho_L}{\rho_V} - 1 \right) x^{0.824} \right] + 1.0 \tag{C.27}$$

C.5 Initial conditions (valid both for channel A and B)

$$p(z, 0) = p_{in} \tag{C.28}$$

$$G(z, 0) = G_{in} \tag{C.29}$$

$$h_m^+(z, 0) = h_{in} \tag{C.30}$$

$$T_w(z, 0) = T_{w0} \tag{C.31}$$

C.6 Boundary conditions

C.6.1 Channel A

$$p(0, t) = p_{in} \tag{C.32}$$

$$G(0, t) = G_{in} - G_b(0, t) \tag{C.33}$$

$$h_m^+(0, t) = h_{in} \tag{C.34}$$

$$p(L, t) = p_b(L, t) \tag{C.35}$$

C.6.2 Channel A

$$p(0, t) = p_{in} \tag{C.36}$$

$$G(0, t) = G_{in} - G_a(0, t) \tag{C.37}$$

$$h_m^+(0, t) = h_{in} \tag{C.38}$$

$$p(L, t) = p_a(L, t) \tag{C.39}$$

Nomenclature

A	cross sectional area
c	specific heat capacity
C_0	concentration parameter
D	diameter
f	friction factor
Fr	Froude number
g	gravity constant
G	mass flux
h	specific enthalpy
K	concentrate local loss constant
L	length
M	mass
N_{pch}	phase change number
N_{sub}	subcooling number
p	pressure
P	perimeter
q	total heat input
q'	linear thermal power density
q''	thermal flux
q'''	volumetric thermal power density
Re	Reynolds number
S	slip ratio
t	time
t_w	wall thickness

T	temperature
U_{ex}	heat transfer coefficient
V	velocity
V_{vj}	effective drift velocity
w	mass flow rate
We	Weber number
x	thermodynamic quality
z	spatial coordinate (axial)

Greek symbols

α	void fraction
β	volumetric ratio
δ	perturbation or Dirac-delta function
θ	slope angle
μ	viscosity
ρ	density
σ	surface tension
τ_w	wall time constant
ϕ	friction multiplier

Subscripts

acc	accelerative
bb	boiling boundary
conc	concentrated
fric	frictional
grav	gravitational
in	inlet
l	only-liquid
L	liquid phase
lo	liquid-only
m	mixture
M	Moody (Darcy)
out	outlet
sat	saturation

v vapor only

V vapor

w wall

Superscripts

+ dynamic

Math symbols

Δ finite difference

Bibliography

COMSOL Multiphysics 3.5a Modeling Guide.

COMSOL Multiphysics 3.5a Reference Guide.

COMSOL Multiphysics 3.5a User's Guide.

Private communication.

W. Ambrosini. Lesson learned from the adoption of numerical techniques in the analysis of nuclear reactor thermal-hydraulic phenomena. *Progress in Nuclear Energy*, 2008.

W. Ambrosini, P. Di Marco, and J. Ferreri. Linear and nonlinear analysis of density wave instability phenomena. *International Journal of Heat and Technology*, 2007.

W. Ambrosini and J. Ferreri. Analysis of basic phenomena in boiling channel instabilities with different flow models and numerical schemes. In *ICONE 14-89863*, 2006.

W. Ambrosini and J. C. Ferreri. On the analysis of thermal-fluid-dynamic instabilities via numerical discretization of conservation equations. *Nuclear Engineering and Design*, 2002.

P. Bolzern, R. Scattolini, and N. Schiavoni. *Fondamenti di controlli automatici.* McGraw-Hill, 2008.

G. Caruso. *Esercitazioni di Impianti Nucleari.* Aracne, 2003.

J. Delhaye et al. *Thermohydraulics of two-phase systems for industrial and nuclear engineering.* Hemisphere, 1981.

T. Hibiki and M. Ishii. One-dimensional drift-flux model and constitutive equations for relative motion between phases in various two-phase flow regimes. *International Journal of Heat and Mass transfer*, 2003.

S. Kakac and B. Bon. A review of two-phase flow dynamic instabilities in tube boiling systems. *International Journal of Heat and Mass transfer*, 2007.

J.Muñoz-Cobo, M. Podowski, and S. Chiva. Parallel channel instabilities in boiling water reactor systems: boundary conditions for out of phase oscillations. *Annals of Nuclear Energy*, 2002.

L. Santini, A. Cioncolini, C. Lombardi, and M. Ricotti. Two-phase pressure drops in a helically coiled steam generator. *International Journal of Heat and Mass transfer*, 2008.

W. R. Schlichting, R. T. Lahey, M. Z. Podowsky, and T. A. Ortega Gòmez. Stability analysis of a boiling loop in space. In *COMSOL Conference, Boston*, 2007.

N. E. Todreas and M. S. Kazimi. *NUCLEAR SYSTEMS I - Thermal Hydraulic Fundamentals*. Taylor&Francis, 1989.